A Torsional Oscillator Study

of

Solid Helium

George Edgar Marcus Nichols

Royal Holloway College

University of London

A dissertation submitted to the University of London

for the degree of Doctor of Philosophy

September 2013

Declaration of Authorship

I, George Nichols, hereby declare that this thesis and the work presented in it is entirely my own. Where I have consulted the work of others, this is always clearly stated.

Signed: _____

Date: _____

Abstract

A compound two-mode torsional oscillator is used to investigate the 'supersolid' signature in polycrystaline ^{4}He. We observe a change in the resonant period of both torsion modes below 200 mK, accompanied by dissipation peaks, consistent with the original observation of Kim and Chan [52]. By careful analysis of the sensitivity of the two modes of the torsional oscillator we are able to account for contributions from changes in the shear modulus of the ^{4}He sample proposed by Beamish *et al* [14] and Maris [61], and the viscoelastic behaviour discussed by Yoo and Dorsey [94]. We find that a zero-frequency period shift remains unaccounted for, corresponding to a velocity-dependant decoupling of 0.14% of the sample with a critical velocity of $\sim 100\,\mu\mathrm{m\,s^{-1}}$. We examine the results of Aoki *et al* and apply the same corrections to their work, finding a decoupling of 0.017% Extensive repair work performed on the cryostat during the experiment is also described.

Acknowledgements

Sincere thanks must go to my supervisor Professor Brian Cowan, whose continued guidance, optimism and patience made this work possible. The experimental cell used in this work was originally designed by Dr Malcolm Poole, who supported my first steps in cryogenics. I am indebted to Professor John Saunders for his comments and robust dialogue. Without the machining skill of Dave Bosworth and precision work of Alan Betts the problems encountered during this experiment would have been insurmountable. Thanks also go to Dr Jan Nyèki, Dr Ben Yager, Dr Lev Levitin and Frank Arnold for their endless support and assistance in the lab, and Jon and Andy Nichols and Alexandra Zuckermann for theirs out of it.

Contents

List of Figures

List of Tables

Chapter 1

Motivation

> "As a rule," said Holmes, "the more bizarre a thing is the less mysterious it proves to be ... It is quite a three pipe problem, and I beg that you won't speak to me for fifty minutes."
>
> *Arthur Conan Doyle*
>
> The Red-headed League

1.1 Helium and Superfluidity

The second most abundant element in the universe is surely the most remarkable. Discovered by spectroscopy on, and named for, the sun in 1868 by French astronomer Jules Janssen [55], helium is the lightest of the noble gasses and makes up around 24% of observable matter in the universe [28]. There are two stable isotopes of

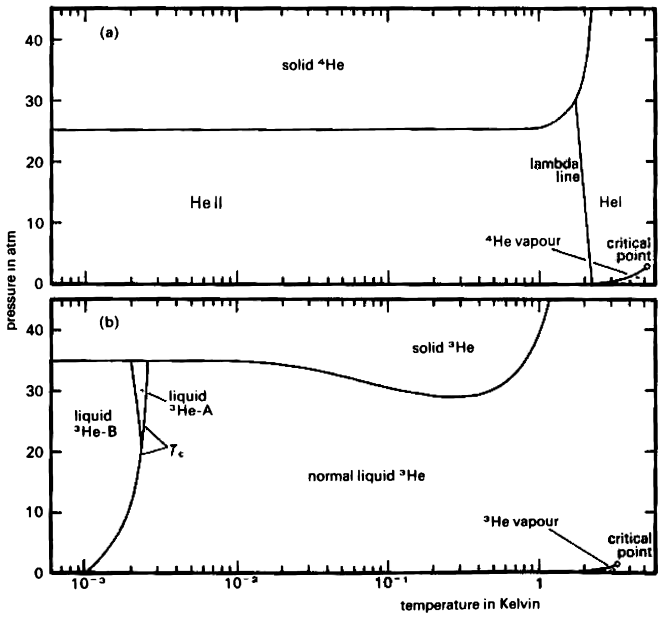

Figure 1.1: $P - T$ phase diagrams of ^{4}He (a) and ^{3}He (b).

helium, by far the most abundant being ^{4}He. ^{4}He on earth is formed by the alpha decay of heavier elements – an alpha particle is a fully ionised ^{4}He nucleus. The other stable isotope is ^{3}He. This occurs at around 1 part per million in ^{4}He collected on earth, but this ratio varies due to the different nuclear processes responsible for their production. Both ^{4}He and ^{3}He are produced in the proton-proton chain reaction in stars, leading to a higher abundance of ^{3}He elsewhere in the solar system [95, 93]. ^{5}He, ^{6}He and ^{7}He and ^{8}He have also been produced, but all have half-lives of less than one second.

Helium was first liquefied by Kamerlingh Onnes in Leiden in 1908 by means of a cascade of cryogens, achieving the few degrees above absolute zero required to condense his valuable sample of helium. For this achievement he received the

1913 Nobel Prize in Physics [67]. The availability of liquid helium in the laboratory allowed experiments at temperatures as low as 1 K producing a number of exciting results, most notably the observation of persistent electrical current in certain metals, but helium held surprises of its own.

Helium was cooled to 1 K by evaporation, but no solid phase was observed at this remarkably low temperature. It was not until 1926 when Keesom subjected a sample to a pressure of 26 atm at low temperature that a solid was formed [48]. Helium's twin properties of low mass and weak van der Waals interaction give rise to a unique property - the lack of a triple point. It is now known that helium is the only material that can remain liquid down to absolute zero [92].

The spherical symmetry of the fully occupied 1s electron orbital means that the helium atom has very low polarisability, and thus its weak interactions and exceptionally low boiling point – 4.2 K for ^{4}He and 3.2 K for ^{3}He at 1 atm. We can see the reason behind the reluctance of helium to solidify by considering its zero point motion. To solidify a material its atoms must be confined to lattice sites. By modelling each atom as an independent quantum harmonic oscillator we may estimate the zero point energy of a helium atom at around $E_0 \approx 7$ meV which would correspond to thermal motion at 70 K. This means that helium atoms are so light that even cooled to absolute zero their quantum mechanical motion overcomes the weak van der Waals attraction between them, and they must be tightly confined by

significant pressures before they will form an ordered solid.

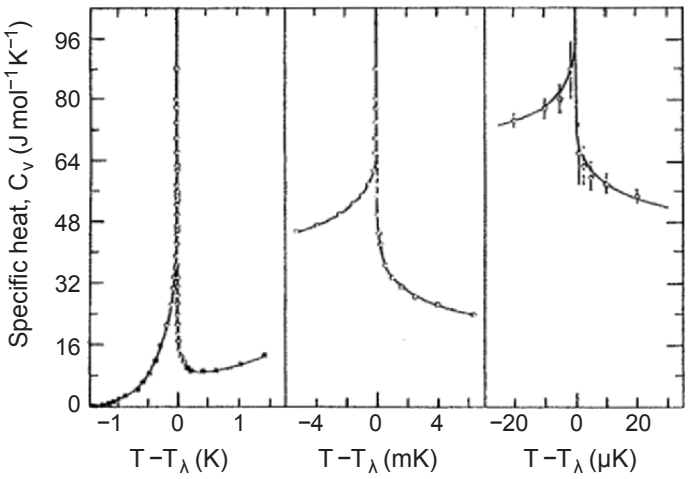

Figure 1.2: The lambda anomaly in the specific heat of liquid ^{4}He. Taken from [20].

In 1924 Boks and Onnes discovered a maximum in the density of liquid helium at 2.3 K [40], and in the same year Dana and Onnes observed a sharp spike in the specific heat of helium around 2.2 K, shown in Fig. 1.2 [20]. The shape of this anomaly – a greek lambda – gives its name to the phase transition to which these phenomena hinted.

Considering the thermal de Broglie wavelength of an atom of helium gives us some insight into its odd behaviour. The de Broglie wavelength, $\lambda_{\mathrm{dB}} = h/p$, encapsulates a central postulate of quantum mechanics – that of wave-particle duality. By calculating the de Broglie wavelength of a particle we can determine whether quantum mechanics will be relevant to its behaviour (if λ_{dB} is comparable to length scales in the experiment) or if it can be described classically (if λ_{dB} is much smaller than any experimental feature). From the Maxwell-Boltzmann distribution we can

approximate the momentum of a particle as

$$p = (2mk_{\mathrm{B}}T)^{1/2}, \tag{1.1}$$

from which we can obtain the thermal de Broglie wavelength

$$\lambda_{\mathrm{dB}} = \left(\frac{2\pi\hbar^2}{mk_{\mathrm{B}}T}\right)^{1/2}. \tag{1.2}$$

For an atom of ^{4}He in the liquid phase ($T < 4.2\,\mathrm{K}$) $\lambda_{\mathrm{dB}} \approx 0.4\,\mathrm{nm}$, and is larger still in ^{3}He. This is greater than the typical interatomic spacing of ^{4}He, $d \approx 0.27\,\mathrm{nm}$, meaning that liquid helium must be considered a *quantum fluid* [7].

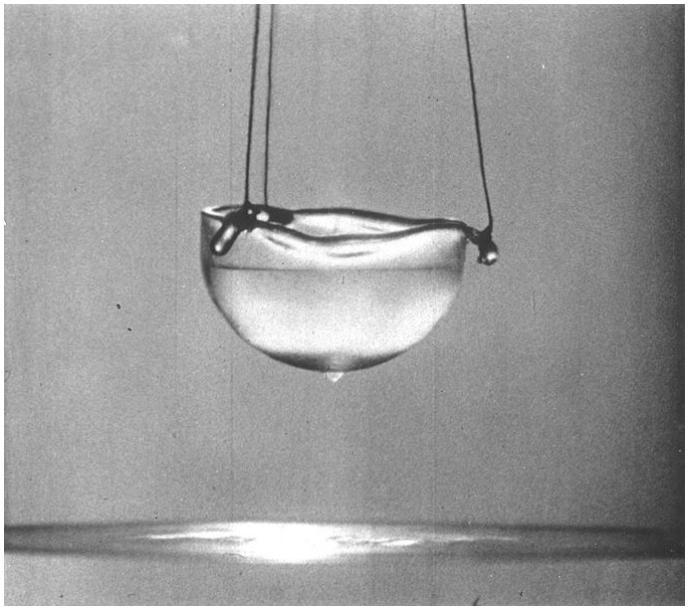

Figure 1.3: A superfluid helium film flowing up the edges of a container, down the outside and dripping into the bath below. A still from an educational video by Alfred Leitner [57]

Below the lambda transition the behaviour of liquid ^{4}He is truly astonishing. Kapitza [47], and Allen and Misener [2], working independently and essentially simultaneously [10] in 1937 discovered that the flow velocity of liquid helium below the lambda transition, dubbed helium II, is almost independent of the pressure driving it. Kapitza concluded that the viscosity of the liquid helium II must be at least 10^6 times smaller than that of the normal liquid, helium I. This lack of viscosity allows helium II to flow through channels too narrow to permit the flow of a normal fluid, causing Kapitza to dub helium II a 'superfluid'. Driving the flow above a certain critical velocity caused the viscosity to return. The meniscus of helium II in a container extends into a film that will run up the walls of the container to find its level. In this way a beaker of helium II will gradually empty itself, shown dramatically in Fig 1.3. Helium II is an astonishingly good conductor of heat, which may be observed by pumping on a vessel of liquid helium to cool it. At high temperatures the liquid will boil vigorously, but on cooling through T_λ the liquid becomes calm as a mill pond [62]. Liquid is still evaporating, but the temperature differences required to nucleate bubbles of gas are equalised by the extraordinary thermal conductivity. A mass flow can be driven by a temperature difference in the liquid helium II, known as the thermomechanical or fountain effect [1]. The liquid level of a volume of helium II separated from a reservoir by a narrow channel will rise when it is heated as liquid flows into the heated region. In the right arrangement this can produce a

dramatic fountain of liquid, driven only by a difference in temperature.

Later in 1937 London proposed that the lambda transition in liquid helium may be analogous to Bose-Einstein Condensation (BEC) [58]. Bose and Einstein had collaborated on the statistics of integer-spin particles, now known as bosons. Unlike half-integer-spin fermions, multiple bosons may occupy a single energy state. Einstein demonstrated that a dilute gas of bosons will condense into the lowest available energy state when cooled to very low temperatures and form a new phase of matter, governed by quantum physics. As helium is a boson (its even number of fundamental particles give it no overall intrinsic angular momentum) any number of helium atoms may occupy a single quantum state. London argued that the lambda-shaped discontinuity in the specific heat of helium was similar to that of an ideal Bose-Einstein gas on condensing into its ground state, and that the unusual behaviour observed in helium II should be considered in the context of Bose and Einstein's condensate phase.

Having seen London's paper, Tisza suggested that the bizarre transport properties observed in helium II could be explained through a 'two-fluid model', where a superfluid condensate state coexisted with a normal liquid [86, 87]. The superfluid flows with no viscosity in response to changes in chemical potential, and the normal fluid flows viscously in response to changes in pressure. As the temperature drops more helium condenses and the superfluid density rises. The condensate state is

not quite a BEC as the interactions between helium atoms are small but significant whereas Einstein's ideal Bose gas is non-interacting, but it shares the key property of a macroscopic wave function. Landau advanced these theories by considering the motion of the superfluid component as a number of quasiparticle excitations. He proposed an excitation spectrum for helium with a linear slope at low energies corresponding to phonon excitations and a minimum corresponding to a particular excitation named the 'roton' at higher energies. The strong coupling between an atom in the condensate and its neighbours involves them in its motion. The low-energy excitations drag many particles together, causing phonon-like collective motion. At high energies the moving atom forces its neighbours to move in backflow around it – a motion likened by Feynman to a smoke ring. From the behaviours of these quasiparticles Landau was able to describe key properties of the superfluid such as the T^3 behaviour of the specific heat, the absence of viscosity and the critical flow velocity. Landau's proposed excitation spectrum was later confirmed by neutron scattering experiments [42], as shown in Fig. 1.4. For these and other achievements he was awarded the 1962 Nobel Prize in Physics [67].

The strength of the two-fluid model was demonstrated experimentally in 1946 by Andronikashvili [6] by measuring the mass of helium viscously dragged between moving plates by its effect on the natural frequency of a torsional oscillator immersed in liquid (see section 2.1). Landau's work on superfluids was later refined by Feyn-

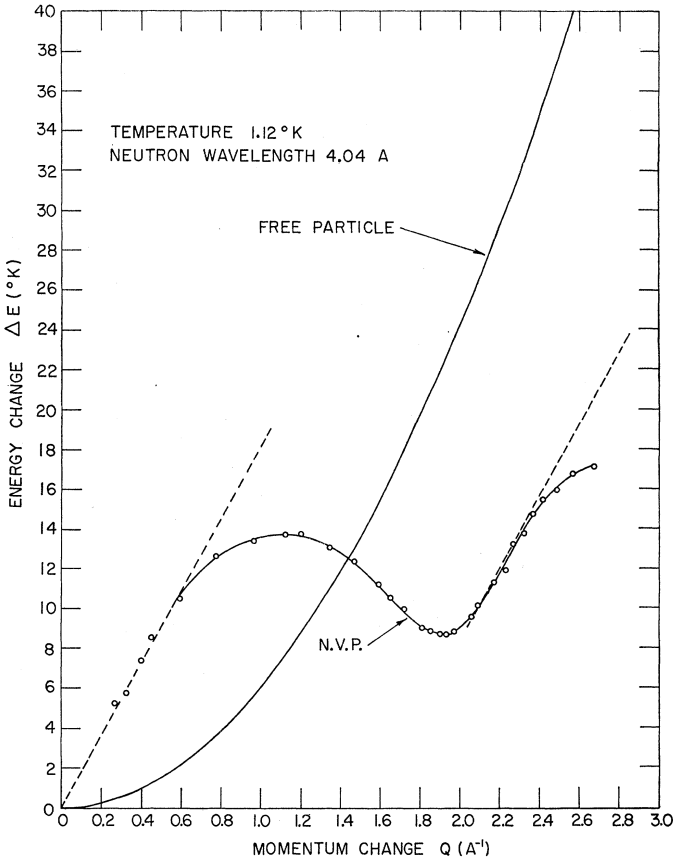

Figure 1.4: The excitation spectrum of liquid ^{4}He, measured by neutron scattering, confirming the roton minimum proposed by Landau. [42].

man to bring his results into better quantitative agreement with experiment [31] and develop the concept of the roton as a vortex ring [32]

The other stable isotope, ^{3}He, has two superfluid phases at temperatures some two orders of magnitude lower than in ^{4}He, as seen in Fig. 1.1. These phases were discovered by Lee, Osheroff and Richardson [69, 70], for which they received the 1996 Nobel Prize in Physics. As a fermion, superfluidity in ^{3}He originates from a pairing mechanism not unlike that in certain superconductors. The low temperatures

required to observe these phases are beyond the reach of the apparatus used in this experiment, and so shall not be discussed further.

1.2 The 'Supersolid' Phase

A 'supersolid' quantum crystal analogous to the superfluid has been conjectured since the late '60s [5, 56, 22]. Such a phase must be rigid and long-range ordered while supporting a flow of mass without dissipation, breaking both translational and gauge symmetries. The popular conception of such a state is that of a gas of lattice vacancies that undergo BEC at low temperature. The high zero-point energy of helium makes its atoms (and therefore any vacancies between them) highly mobile. If such mobile vacancies can exist at low temperatures [33, 71, 4] helium is a likely candidate for such a phase. Legget proposed a study of the DC rotation of an annulus of solid sample while cooling through the proposed transition temperature, and slowing the rotation below a presumed critical velocity. In both cases the superfluid-like flow would reduce the moment of inertia of the sample and speed its rotation as a persistent mass current is established [56].

Such DC rotation is extremely challenging at millikelvin temperatures and high pressures – how does one fill the sample cell, for example – so other methods have been employed in the search for supersolid behaviour. Greywall [36] attempted to measure a mass flow between two reservoirs driven by a difference in pressure but

saw no 'superflow'. Bishop *et al* [16] looked for a change in the natural frequency of a torsional oscillator but saw no effect. These and other early searches are extensively reviewed by Meisel [63].

In 1997 Goodkind *et al* [43] observed an anomaly in the acoustic attenuation and velocity in solid ^{4}He at 200 mK and suggested this was consistent with a phase transition, specifically a BEC of vacancies in the solid.

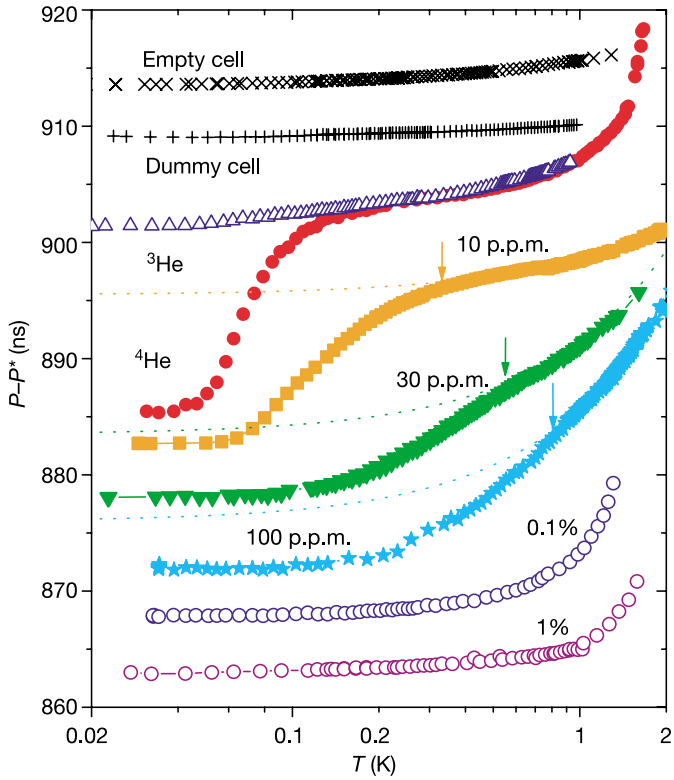

Figure 1.5: Kim and Chan's observation of an anomalous period shift in solid ^{4}He in vycor glass [53].

In 2004 Kim and Chan [53] loaded a torsional oscillator with solid ^{4}He in a porous matrix of vycor glass and tracked its natural frequency. On cooling the oscillator

below 200 mK they observed an abrupt drop in its resonant period, shown in Fig.1.5, which they interpreted as a drop in the moment of inertia of the sample. The change in period was suppressed by high drive speeds and increasing concentration of ^{3}He. No change in period was observed in a pure ^{3}He sample. Kim and Chan went on to repeat the experiment using a bulk ^{4}He sample loaded into an annular cell and saw a similar drop in resonant period [52]. In this experiment a control was made by blocking the annulus to prevent rotational flow. This strongly suppressed the period shift, consistent with a fluid-like flow of mass around the annulus. The torsional oscillator results have been reproduced by several other groups [8, 39, 82, 45, 96, 72] with broadly similar results.

If solid ^{4}He does have a genuinely superfluid component it should be observable in DC mass flow experiments. Several attempts have been made to force mass flow between two reservoirs joined by a constriction by applying pressure to one resevoir and measuring the pressure at the other [36, 18, 27, 83] but none have observed a measurable mass flux. It is possible that these experiments failed as they exert force on the rigid lattice of solid helium, rather than driving the superfluid component within it. Ray and Hallock [76, 75] took a more subtle approach and grew their solid sample in a cell connected to two remote chambers by porous vycor rods. The confinement of the vycor raises the melting point of the helium, so that solid in the bulk and superfluid in the rods may coexist in thermal equilibrium. The chambers

at other ends of the rods can then be filled with bulk superfluid helium at a higher temperature. By analogue to the fountain effect one would expect temperature differences between the two liquid resevoirs two drive a mass flux through the 'supersolid' chamber. A mass flux is observed, but at temperatures far higher than the torsional oscillator anomaly–up to 600 mK. Balibar and Caupin [12] suggest that this mass flux may originate from liquid channels between grain boundaries and the chamber walls rather than a superfluid-like flow. Ray and Hallock [77] argue that the observed hysteresis of the flow cannot be explained by liquid channels, and represents superfluid-like mass flux along grain boundaries or dislocations.

Tsepelin *et al* followed the melting curve of ^{4}He with a high precision pressure cell [88]. The crystal followed the expected T^4 behaviour with no sign of a supersolid transition.

In 2007 Day and Beamish loaded helium into a cell containing two piezo transducers supported on rigid posts and separated by a narrow gap [25]. One transducer is driven sinusoidally to oscillate back and forth. This motion shears the helium between the two transducers which in turn exerts a force on the other transducer, generating a voltage across it. Thus the shear modulus of the helium sample may be measured directly at a wide range of frequencies. Day and Beamish showed that the shear modulus rises on cooling the sample below 200 mK. This rise has a remarkably similar shape to the torsional oscillator period shift, is independent of

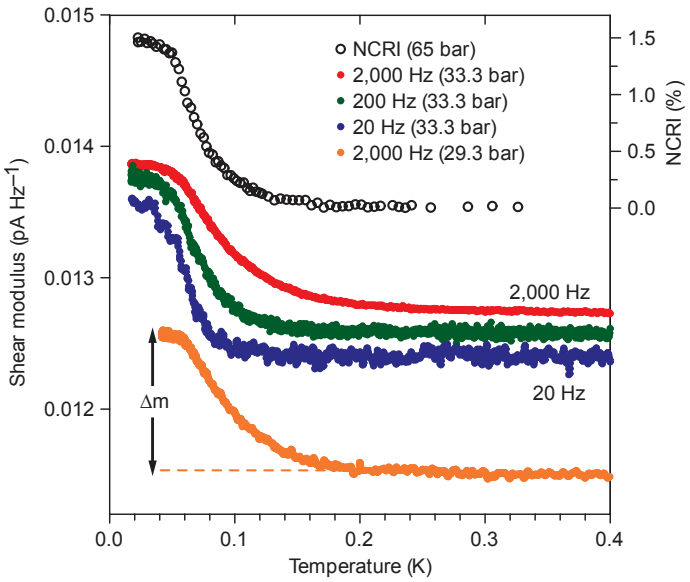

Figure 1.6: Similarity between the torsional oscillator and shear modulus measurements in ^{4}He [25].

frequency and is similarly suppressed by high strain and ^{3}He impurity concentration, as shown in Fig. 1.6.

It is now well understood that the change in shear modulus observed by Day and Beamish can affect the behaviour of torsional oscillators loaded with solid helium [79], but could it *effect* them? A number of subtle changes to the torsional oscillator period have been proposed as arising from changes in the shear modulus of the sample:

- The viscoelastic motion of the solid sample will change as the shear modulus varies [94, 61], causing a change in the apparent moment of inertia.

- The base of the torsional oscillator cell is in torsion along with the rod, and its torsion constant will be changed by the helium sample in contact with it [61].

- If the torsional oscillator sample chamber is shaped as an annulus with a solid cylinder forming the inner wall it may move independently of the oscillator, shearing the helium and changing the natural frequency [64].

- Torsional oscillators that are filled through their torsion rod will experience a stiffening of the rod as the shear modulus increases. This will cause the natural frequency of the oscillator to increase, just as would be seen from a reduction in the moment of inertia of the sample [14].

Any torsional oscillator study of helium at these temperatures must take these contributions in to account.

No study has yet conclusively proven the existence of a 'supersolid' phase, and some early proponents of the discovery are now distancing themselves from it [78, 11]. Chan *et al* have repeated some of the early torsional oscillator experiments made in their group using cells designed to be resistant to the shear modulus contributions discussed above, and has seen no period shift [50]. Balibar *et al* argue that the effect is down to 'giant plasticity' of ^{4}He crystals [41] which freezes out at low temperatures, and the torsional oscillator period shift is merely the crystals' shear modulus returning to 'normal'.

There are still unexplained results. Several explanations exist of the DC flow measurements of Ray and Hallock. The torsional oscillators of some groups designed to negate shear modulus contributions still show period shifts [65]. Sullivan *et al*

have measured the NMR signal of extremely dilute ^{3}He in solid ^{4}He samples and see features and hysteresis around 200 mK [54]. Kim *et al* have used a variety of sophisticated torsional oscillators and piezo transducers to measure the response of solid ^{4}He in rotating cryostats and see a range of unexpected features [23].

Recently a 'supersolid' phase has been theorised [49] and experimentally realised [13] in optical lattice traps. This involves the self-organisation of a BEC of cold atoms into a 'checkerboard' lattice, with atoms occupying alternate states at neighbouring sites. This phase spontaneously breaks spatial and gauge symmetries, meeting our criteria for a 'supersolid'.

It remains unclear whether a 'supersolid' phase can be realised in solid helium.

Chapter 2

The Torsional Oscillator

> Nothing happens until something moves.
>
> *Albert Einstein*

2.1 Background

The Torsional Oscillator (TO) is a commonly used instrument for measuring dynamic mechanical properties of a liquid or solid sample. The first TO was designed by Andronikashvili in 1946 after a suggestion by Landau as a way to measure the superfluid density of liquid helium [6]. His oscillator comprised a bob made up of stacked aluminium discs 10 µm thick, spaced 200 µm apart, suspended on a phosphor-bronze wire. In his experiment the bob was immersed in a sample of liquid helium and a torque applied to the wire to start it oscillating in torsion.

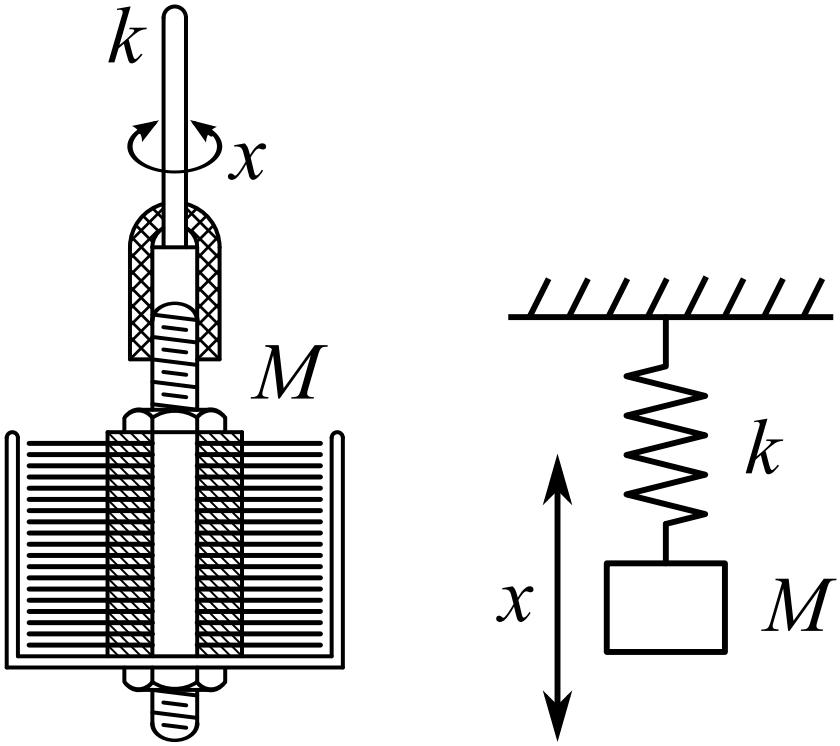

Figure 2.1: A schematic of Andronikashvili's torsion bob oscillator experiment (a) and the mass-spring model (b).

The bob will behave as a simple harmonic oscillator, modelled as a mass M on a spring of force constant k with position x. We balance the restoring force of the spring, given by Hooke's law $F = -kx$, and the acceleration of the mass, given by Newton's second law $F = m\ddot{x}$, to arrive at the equation of motion

$$M\ddot{x} + kx = 0. \tag{2.1}$$

As one would intuitively expect, this has the solution of sinusoidal motion

$$x(t) = A \sin \omega t \tag{2.2}$$

where A is the amplitude of oscillations and ω their frequency. Substituting this into the equation of motion provides us with the natural frequency of the oscillator

$$\omega_0 = \sqrt{\frac{k}{M}}. \tag{2.3}$$

It will be important later to note that the natural frequency depends on both the mass and the spring constant.

As the separation of the aluminium discs is less than the known viscous penetration depth of normal liquid helium the liquid between the discs is dragged along with the bob, increasing its moment of inertia. By effectively increasing the mass of the bob M, the natural frequency ω_0 of its oscillations is necessarily reduced.

The liquid helium sample is then cooled below T_λ. As the liquid becomes superfluid its viscosity drops to zero and so is no longer dragged with the bob. As such, the bob effectively loses moment of inertia, and so its natural frequency increases. By measuring the oscillation frequency of the torsion bob at various temperatures Andronikashvili was able to quantify the superfluid density below the λ transition and so provide strong evidence for Landau's two-fluid model of superfluid helium.

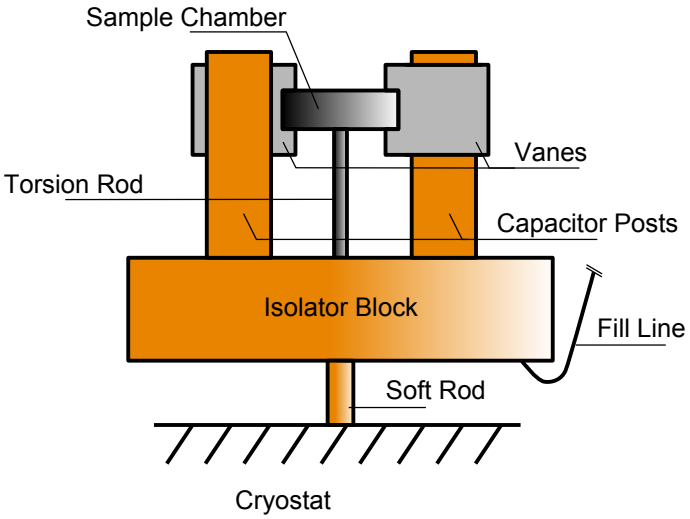

Figure 2.2: A schematic diagram of a modern torsional oscillator.

Modern torsional oscillator experiments encapsulate the sample in a closed cell rather than being immersed into them [15] allowing pressurised samples and solids to be studied. Such an oscillator might consist of a sample chamber, commonly metal or epoxy but other materials such as sapphire have been used [30], mounted to a springy torsion rod. The torsion rod is then anchored to an isolator block which is connected by a soft rod to the cryostat. The isolator block is designed to have a lower natural frequency than the experimental cell and act as a low-pass filter to vibrations. Attached to the sample chamber are two vanes which are used to drive the oscillator and detect its motion. A capillary fill line through which to load the sample may enter the cell directly, or the torsion rod may be drilled out to act as a fill line.

Two capacitor posts with electrically isolated surfaces are mounted on to the

isolator block. These surfaces are held close enough to capacitatively couple to the oscillator vanes. An AC signal is superimposed on to a DC bias voltage and applied to one post to continuously drive the oscillator while the other is used to measure the oscillator's movement. In some designs [45] the vanes contain magnets and the movement of the oscillator induces a current in a pickup coil in the posts, allowing for very precise measurement via a SQUID.

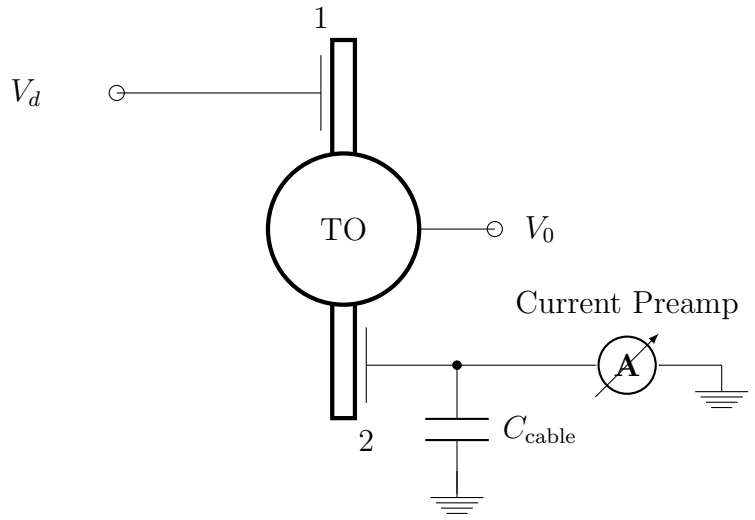

Figure 2.3: Top-down schematic of the electrical contacts of torsional oscillator, showing the capacitatively coupled electrodes.

The oscillator used in this experiment is of capacitatively coupled design with detection via a current preamplifier, as shown schematically in Fig. 2.3. The vanes of the oscillator are rigidly mounted to the cell and electrically isolated from it. In use they are raised to a high voltage V_0 (typically a few hundred volts) to provide the E-field across the gaps between the posts and the vanes. Alternatively, the vanes may be grounded and the plates raised to high voltage with appropriate isolation

from the readout instruments, as shown in Fig. 2.10 in section 2.4. The electrodes on the posts are of equal area A and separated from the vanes by distance $d_{1,2}$. The capacitance of the gaps 1 and 2 is then

$$C_{1,2} = \frac{\epsilon_0 A}{d_{1,2}}. \tag{2.4}$$

The driving electrode 1 stores the field energy

$$U_1 = \frac{C_1 V_1^2}{2} \tag{2.5}$$

which we differentiate to find the force acting on vane 1 of the oscillator:

$$F = -\frac{\partial U}{\partial d_1} \tag{2.6}$$

$$= \frac{\epsilon_0 A}{2d^2} V_1^2 = \frac{C_1}{2d_1} V_1^2 = \frac{C_1^2}{2\epsilon_0 A} V_1^2. \tag{2.7}$$

It is often desirable to write these expressions in terms of the area and the capacitance rather than the separation d, as the gap is difficult to measure. The voltage on the drive electrode V_1 is the sum of the AC drive and the DC bias

$$V_1 = V_0 + V_d \tag{2.8}$$

so we may rewrite the force as

$$F = \frac{C_1}{2d_1}(V_0 + V_d)^2 \tag{2.9}$$

$$= \frac{C-1}{2d_1}(V_0^2 + 2V_0V_d + V_d^2). \tag{2.10}$$

As $V_d \ll V_0$ we may neglect the V_d^2 term, leaving

$$F = \frac{C_1}{2d_1}V_0^2 + \frac{C_1}{d_1}V_0V_d \tag{2.11}$$

$$= F_0 + \Delta F \tag{2.12}$$

where F_0 is a static force

$$F_0 = \frac{C_1}{2d_1}V_0^2 \tag{2.13}$$

and ΔF is a much smaller oscillating force

$$\Delta F = \frac{C_1}{d_1}V_0V_d. \tag{2.14}$$

By assuming linearity we may apply Hooke's law and introduce a torsion constant

k as in our simple harmonic oscillator model above to give a static displacement d_0

$$d_0 = k\frac{C_1}{2d_1}V_0^2 \tag{2.15}$$

$$= k\frac{C_1^2}{2\epsilon_0 A_1}V_0^2 \tag{2.16}$$

and an oscillating displacement Δd

$$\Delta d = k\frac{C_1}{d_1}V_0 V_d \tag{2.17}$$

$$= k\frac{C_1^2}{\epsilon_0 A_1}V_0 V_d. \tag{2.18}$$

We may now obtain the velocity of the vane from the time derivative of this displacement. Since the variation is $e^{i\omega t}$ the velocity is $|\dot{d}| = |\omega \Delta d|$, giving

$$|\dot{d}| = k\omega\frac{C_1}{d_1}V_0 V_d \tag{2.19}$$

$$= k\omega\frac{C_1^2}{\epsilon_0 A_1}V_0 V_d. \tag{2.20}$$

We have assumed a constant C_1, so we require that the displacement of the vane be much less than the electrode spacing, *i.e.* $\Delta d \ll d_1$. Because the torsional oscillator is a resonant system this displacement will be multiplied many times when the oscillator is driven at its resonant frequency. We shall derive the resonant response of the oscillator in section 2.2, and this frequency-dependant behaviour will multiply

the displacement calculated above.

The situation is slightly different on the detection side due to the behaviour of the current preamplifier. Here we consider the cable capacitance C_{cable} so that

$$C = C_2 + C_{\text{cable}} \tag{2.21}$$

and we know that V_2 is constant and $V_2 = V_0$ as the electrode post is grounded through the preamp. Here the capacitance between the electrode and the vane is

$$C_2 = \frac{\epsilon_0 A}{d_2} \tag{2.22}$$

$$= \frac{\epsilon_0 A}{d + \Delta d e^{i\omega t}}. \tag{2.23}$$

As we are measuring the current, we differentiate the charge $Q_2 = CV_2$

$$I = \frac{dQ_2}{dt} \tag{2.24}$$

$$= V_0 \frac{dC}{dt} \tag{2.25}$$

which, because C_{cable} is constant, is equal to

$$I = V_0 \frac{dC_2}{dt} \tag{2.26}$$

$$= -i\omega V_0 C_2 \frac{\Delta d}{d} e^{i\omega t}. \tag{2.27}$$

Note then that by using a current preamplifier we have eliminated any contributions arising from the cable capacitance, and introduced a 90° phase shift. The current preamplifier has gain G_A, typically $1\,\mathrm{M}\Omega$, such that $V_{out} = G_A I$. The signal we observe is thus

$$V_{out} = -i\omega G_A V_0 C_2 \frac{\Delta d}{d} e^{i\omega t}. \tag{2.28}$$

We rearrange to find the amplitude of the displacement $|\Delta d|$ from the the signal amplitude $|V_{out}|$

$$|\Delta d| = \frac{|V_{out}| d_2}{\omega G_A V_0 C_2} \tag{2.29}$$

from which we eliminate d_2 via eqn 2.22

$$|\Delta d| = \frac{|V_{out}| A \epsilon_0}{\omega G_A V_0 C_2^2}. \tag{2.30}$$

and as above in Eq. 2.20 we obtain the velocity of vane 2 in terms of readily measureable quantities:

$$|\dot{d}| = \frac{|V_{out}| A \epsilon_0}{G_A V_0 C_2^2}. \tag{2.31}$$

Using either analogue or digital electronics at room temperature the torsional oscillator can be held on resonance as the temperature is varied. In this way the resonant frequency, and so any changes in the moment of inertia of the sample, can be tracked as a function of temperature. The amplitude of the drive may also be

varied to study critical velocity phenomena.

2.2 The Damped, Forced Oscillator

The movement of the oscillator and the sample under study will not be perfectly elastic, meaning that its motion will be damped; in the linear regime we approximate this as an additional force proportional to its speed. We introduce the damping constant γ to give the damped harmonic oscillator equation of motion

$$M\ddot{x} + \gamma\dot{x} + kx = 0 \tag{2.32}$$

and may follow Boas [17], or any undergraduate mechanics textbook, for our solution. For convenience we substitute $2b = \frac{\gamma}{M}$ and our earlier result for the undamped resonant frequency $\omega_0^2 = \frac{k}{M}$ from Eq. 2.3. We may then solve the auxilliary equation

$$D^2 + 2bD + \omega_0^2 = 0 \tag{2.33}$$

which has roots

$$D = \frac{-2b \pm \sqrt{4b^2 - 4\omega_0^2}}{2} = -b \pm \sqrt{b^2 - \omega_0^2}. \tag{2.34}$$

As the torsional oscillator is designed to be as lightly damped as posssible, we solve this in the underdamped case where $b^2 < \omega_0^2$, meaning that $\sqrt{b^2 - \omega_0^2}$ is imaginary. We let

$$\beta = \sqrt{\omega_0^2 - b^2} \tag{2.35}$$

so that

$$\sqrt{b^2 - \omega_0^2} = i\beta. \tag{2.36}$$

The roots of the auxiliary equation are then

$$-b \pm i\beta. \tag{2.37}$$

The general solution for complex roots may then be expressed as

$$x = e^{-bt}(A \sin \beta t + B \cos \beta t) \tag{2.38}$$

which, as we might expect, describes an exponentially decaying sinusoid. Note though that the frequency of the oscillation

$$\beta = \sqrt{\omega_0^2 - \frac{\gamma^2}{4M^2}} \tag{2.39}$$

is reduced from the undamped resonant frequency ω_0 and approaches it in the limit of low damping, *i.e.* when $\gamma \to 0, \beta \to \omega_0$.

In most modern torsional oscillator experiments a continuous sinusoidal drive is applied to the oscillator. Adding a driving torque $\Gamma = \Gamma_0 \sin \omega_d t$ of amplitude Γ_0 and frequency ω_d we arrive at the equation of motion

$$M\ddot{x} + \gamma\dot{x} + kx = \Gamma_0 \sin \omega_d t. \tag{2.40}$$

The solution to this is of the form *transient solution + steady-state solution*, but because we know the transient solution, given by the complementary function, will tend to zero after some finite time (as shown above) we may concern ourselves only with the steady state solution, given by the particular integral. Using the method of complex exponentials to solve the particular integral we first solve the equation

$$\ddot{y} + 2b\dot{y} + \omega_0^2 y = \Gamma_0 e^{i\omega_d t} \tag{2.41}$$

by substituting

$$y_p = Ce^{i\omega_d t}. \tag{2.42}$$

We thus find

$$-\omega_d^2 y + 2ib\omega_d y + \omega_0^2 y = \Gamma_0 e^{i\omega_d t} \tag{2.43}$$

$$(-\omega_d^2 + 2ib\omega_d + \omega_0^2)Ce^{i\omega_d t} = \Gamma_0 e^{i\omega_d t} \tag{2.44}$$

which we solve for C:

$$C = \frac{\Gamma_0}{-\omega_d^2 + 2ib\omega_d + \omega_0^2} \tag{2.45}$$

$$= \frac{\Gamma_0}{(\omega_0^2 - \omega_d^2) + 2ib\omega_d} \tag{2.46}$$

$$= \frac{(\omega_0^2 - \omega_d^2) - 2ib\omega_d)\Gamma_0}{(\omega^2 - \omega_d^2)^2 + 4b^2\omega_d^2} \tag{2.47}$$

or in the form $Re^{i\theta}$

$$|C| = \frac{\Gamma_0}{\sqrt{(\omega_0^2 - \omega_d^2)^2 + 4b^2\omega_d^2}} \tag{2.48}$$

$$\therefore C = \frac{\Gamma_0}{(\omega_0^2 - \omega_d^2)^2 + 4b^2\omega_d^2} e^{-i\varphi}. \tag{2.49}$$

So our substitution 2.42 becomes

$$y_p = \frac{\Gamma_0}{\sqrt{(\omega_0^2 - \omega_d^2)^2 + 4b^2\omega_d^2}} e^{i(\omega_d t - \varphi)} \tag{2.50}$$

Giving us our steady state solution

$$x(\omega_d) = \Im(y_p) = \frac{\Gamma_0}{\sqrt{(\omega_0^2 - \omega_d^2)^2 + \gamma^2\omega_d^2/M^2}} \sin(\omega_d t - \varphi). \tag{2.51}$$

Once again this gives our expected result of sinusoidal oscillations, phase shifted from the drive by φ, whose amplitude is suppressed by damping γ and increases on

resonance, *i.e.* as $\omega_d \to \omega_0$, as shown in Fig. 2.4.

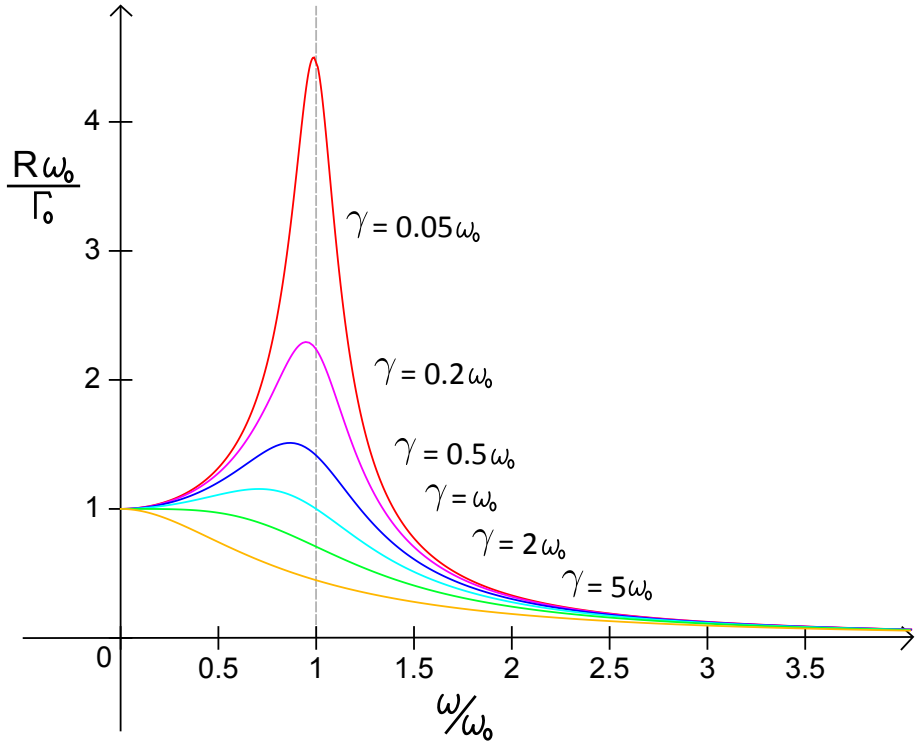

Figure 2.4: The steady-state response of a forced harmonic oscillator with different amounts of damping. As the damping is decreased the resonance better approximates a Lorentzian peak and the peak position approaches ω_0.

Although the lineshape of the resonance in frequency space is not strictly symmetric about ω_0 it may be well approximated as such in the limit where $\gamma \ll \omega_0$. The resonance lineshape follows a Lorentzian curve with amplitude

$$R(\omega) = R_0 \frac{\delta^2}{(\omega - \omega_0)^2 + \delta^2} \tag{2.52}$$

where R_0 is the maximum amplitude of the peak, and δ is its width.

In torsional oscillator experiments it is more common to express the damping

of the oscillator as a dimensionless quality-factor, or Q-value. This may be defined in a number of ways, but may be most simply thought of as the energy stored in a resonant system divided by the energy dissipated per cycle, that is

$$Q = 2\pi \times \frac{\text{Energy Stored}}{\text{Loss per Cycle}} = \omega_0 \times \frac{\text{Energy Stored}}{\text{Power Loss}} \tag{2.53}$$

which in the case of low loss is equal to the resonant frequency divided by the linewidth

$$Q = \frac{\omega_0}{\Delta\omega} \tag{2.54}$$

and is related to the damped oscillator response discussed above by

$$Q = \frac{\sqrt{Mk}}{\gamma} \tag{2.55}$$

Equation 2.53 encapsulates the intuitive value of this parameter, as it gives the time it will take a resonator to lose practically all its energy ($1/e^{2\pi}$, or $\sim 1/535$ of its initial energy), expressed as a number of cycles of that resonator. Because Q is directly related to the linewidth it is a good measure of the resolution performance of a torsional oscillator - that is the smallest $\Delta\omega_0$ and therefore the smallest ΔM it can perceive. A typical torsional oscillator might have a Q of a few thousand at room temperature, rising to tens of thousands on cooling it to nitrogen temperature as the material stiffens and its torsion constant rises. On further cooling various

dissipation mechanisms begin to freeze out and the Q may rise to several hundred thousand at helium temperature, and by the limit of dilution cooling may exceed a million. This means that for a typical torsional oscillator experiment mounted on a dilution unit with $Q = 500\,000$ and $\omega_0 = 2\,\mathrm{kHz}$ the linewidth of the resonance would be $4\,\mu\mathrm{Hz}$.

2.3 The Two Mode Torsional Oscillator

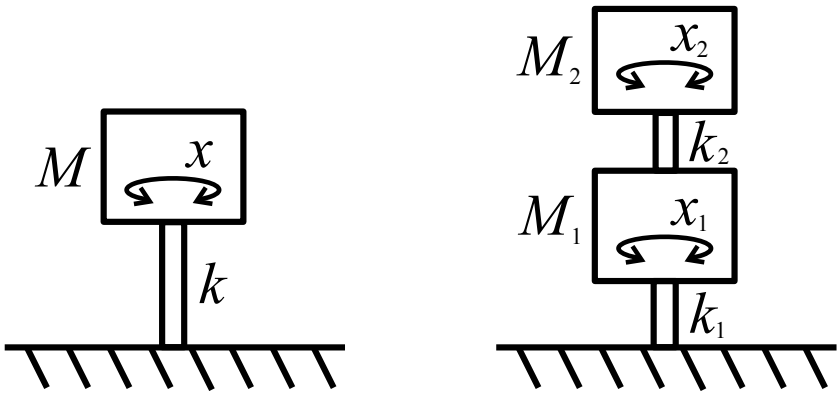

Figure 2.5: A single (a) and double (b) torsional oscillator.

The two-mode compound torsional oscillator uses a second 'dummy' mass joined by a second torsion rod to allow the study of one sample at two frequencies. As before we formulate an equation of motion from the forces acting on the two masses

that arise from Hooke's law, namely the torques Γ_1 and Γ_2:

$$\begin{aligned} \Gamma_1 &= -k_1 x_1 - k_2(x_1 - x_2) \\ \Gamma_2 &= -k_2(x_2 - x_1) \end{aligned} \tag{2.56}$$

which produce the angular accelerations

$$\begin{aligned} M_1 \ddot{x_1} &= \Gamma_1 \\ M_2 \ddot{x_2} &= \Gamma_2 \end{aligned} \tag{2.57}$$

and thus the equations of motion for the two masses are

$$\begin{aligned} k_1 x_1 + k_2(x_1 - x_2) &= -M_1 \ddot{x_1} \\ k_2(x_2 - x_1) &= -M_2 \ddot{x_2}. \end{aligned} \tag{2.58}$$

We are interested in the normal modes – solutions where both masses are oscillating with the same frequency, that is

$$\begin{aligned} x_1(t) &= X_1 e^{i\omega t} \\ x_2(t) &= X_2 e^{i\omega t}. \end{aligned} \tag{2.59}$$

Substituting these into the equations of motion we arrive at the following equations

$$\begin{aligned}(k_1 + k_2)x_1 - k_2 x_2 &= M_1\omega^2 x_1 \\ -k_2 x_1 + k_2 x_2 &= M_2\omega^2 x_2\end{aligned} \tag{2.60}$$

which may be conveniently represented in eigenvector/eigenvalue form $\mathbf{Ax} = \lambda\mathbf{x}$:

$$\begin{pmatrix} (k_1 + k_2)/M_1 & -k_2/M_1 \\ -k_2/M_2 & k_2/M_2 \end{pmatrix} \begin{pmatrix} x_1 \\ x_2 \end{pmatrix} = \omega^2 \begin{pmatrix} x_1 \\ x_2 \end{pmatrix}. \tag{2.61}$$

The homogeneous, characteristic equations are thus

$$\begin{aligned}(k_1 + k_2 - M_1\omega^2)x_1 - k_2 x_2 &= 0 \\ -k_2 x_1 + (k_2 - M_2\omega^2)x_2 &= 0.\end{aligned} \tag{2.62}$$

We find the eigenfrequencies of this system by the requirement that the determinant of the matrix of characteristic equations be zero, *i.e.* the eigenvalues of matrix $\mathbf{A}$ are the real numbers λ that satisfy the equation $\det(\mathbf{A} - \lambda\mathbf{I}) = 0$ where $\mathbf{I}$ is the identity matrix.

$$\begin{vmatrix} (k_1 + k_2) - M_1\omega^2 & -k_2 \\ -k_2 & k_2 - M_2\omega^2 \end{vmatrix} = 0 \tag{2.63}$$

Which gives us a quadratic equation for ω^2:

$$M_1 M_2 \omega^4 - (k_2 M_1 + k_1 M_2 + k_2 M_2)\omega^2 + k_1 k_2 = 0. \tag{2.64}$$

This provides us with two positive solutions for the natural frequencies of the oscillator. We shall see later that the lower frequency corresponds to a symmetric oscillation (x_1 and x_2 have the same sign) and the higher frequency to an antisymmetric oscillation (x_1 and x_2 have opposite signs), so they are designated ω_s and ω_a respectively:

$$\begin{aligned}
\omega_a^2 &= \frac{1}{2}\left(\frac{k_1}{M_1} + \frac{k_2}{M_1} + \frac{k_2}{M_2}\right) + \sqrt{\frac{1}{4}\left(\frac{k_1}{M_1} + \frac{k_2}{M_1} + \frac{k_2}{M_2}\right)^2 - \frac{k_1}{M_1}\frac{k_2}{M_2}} \\
\omega_s^2 &= \frac{1}{2}\left(\frac{k_1}{M_1} + \frac{k_2}{M_1} + \frac{k_2}{M_2}\right) - \sqrt{\frac{1}{4}\left(\frac{k_1}{M_1} + \frac{k_2}{M_1} + \frac{k_2}{M_2}\right)^2 - \frac{k_1}{M_1}\frac{k_2}{M_2}}
\end{aligned} \tag{2.65}$$

From the characteristic equations (2.62) we can derive two equivalent equations for the ratio of displacements

$$\begin{aligned}
\frac{X_2}{X_1} &= \frac{k_1 + k_2 - M_1\omega^2}{k_2} \\
\frac{X_2}{X_1} &= \frac{k_2}{k_2 - M_2\omega^2}
\end{aligned} \tag{2.66}$$

which we can solve at the two eigenfrequencies ω_a and ω_s to give

$$\begin{aligned}\left.\frac{X_2}{X_1}\right|_a &= \frac{1}{2}\left\{\left(1+\frac{k_1}{k_2}-\frac{M_1}{M_2}\right)-\sqrt{\left(1+\frac{k_1}{k_2}+\frac{M_1}{M_2}\right)^2-4\frac{k_1}{k_2}\frac{M_1}{M_2}}\right\}\\ \left.\frac{X_2}{X_1}\right|_s &= \frac{1}{2}\left\{\left(1+\frac{k_1}{k_2}-\frac{M_1}{M_2}\right)+\sqrt{\left(1+\frac{k_1}{k_2}+\frac{M_1}{M_2}\right)^2-4\frac{k_1}{k_2}\frac{M_1}{M_2}}\right\}.\end{aligned} \tag{2.67}$$

As the moments of inertia M_1 and M_2 and the torsion constants k_1 and k_2 are necessarily positive the square root term must always be greater than the first term. Thus $\left.\frac{x_2}{x_1}\right|_a$ must always be negative and $\left.\frac{x_2}{x_1}\right|_s$ must always be positive. This means that in the first case the displacements must have opposite sign at all times and in the second case they must have the same sign, hence their designations as antisymmetric and symmetric respectively. We may reduce these displacement ratios in terms of the characteristic frequency $\omega_2 = \sqrt{\frac{k_2}{M_2}}$ to a more convenient form

$$\left.\frac{X_2}{X_1}\right|_a = \frac{1}{1-\omega_a^2/\omega_2^2} \quad \text{and} \quad \left.\frac{X_2}{X_1}\right|_s = \frac{1}{1-\omega_s^2/\omega_2^2}. \tag{2.68}$$

2.4 Our Torsional Oscillator

Our torsional oscillator is a two mode design made from coin silver (90% Ag, 10% Cu) with magnesium vanes. The sample is contained in the hollow 'head'. The oscillator is designed after that of Morley *et al* [66]. Coin silver was chosen over the more conventional beryllium copper as it offers comparable low temperature

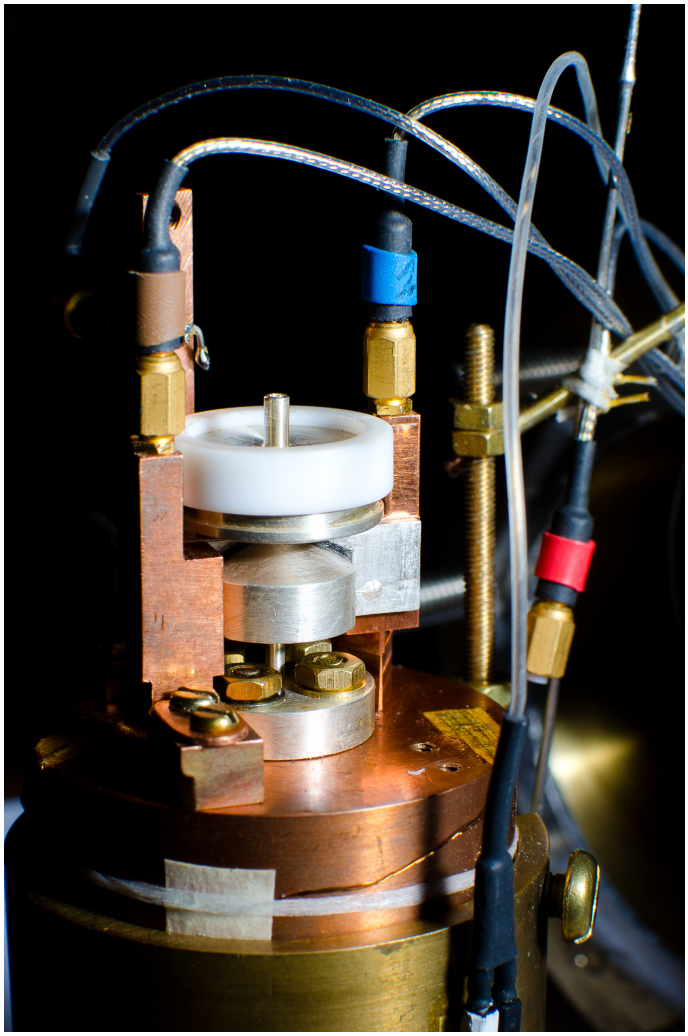

Figure 2.6: The torsional oscillator cell, mounted in a test probe.

performance in Q and thermal conductivity with less temperature dependence of the oscillation frequency and dissipation of the empty cell. In addition there are safety concerns when machining beryllium copper as it's dust can cause serious lung damage if inhaled [68].

After machining the oscillator is annealed in vacuum at 650 °C for 12 hours to improve its mechanical properties. This is an in-house 'recipe' that has been found

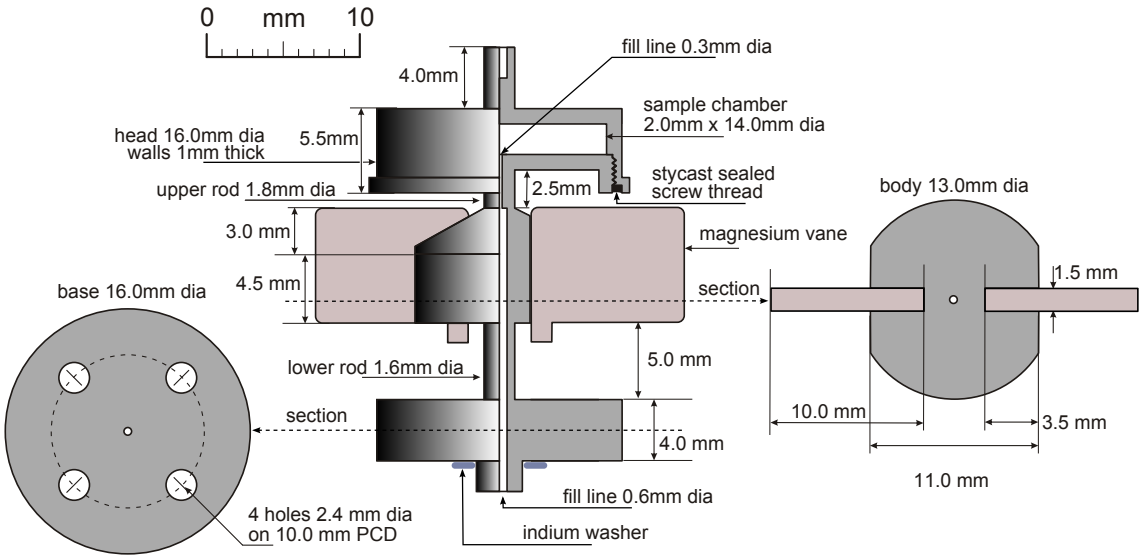

Figure 2.7: Technical drawing of the torsional oscillator cell. The pressure gauge assembly is shown separately in Fig. 2.9.

to give good performance ($Q > 100000$) at low temperatures. Magnesium is used for the vanes to save weight - the change in moment of inertia of the sample ΔM may be very small, so for good sensitivity the mass of the oscillator must be kept as small as the strength requirements will allow. As the vanes are far from the torsion axis and moment of inertia goes as the square of radius it is especially important that the vanes be both light and rigid.

Fine wires run to the vanes to raise them to high voltage. A number of wiring arrangements were tested in a dipping probe at 4 K, as shown in Fig. 2.8. Originally 38-gauge bare copper wires were soldered to the pin of the Microdot connector, routed around the oscillator head and secured to the wings with conductive silver DAG adhesive, as (a). The Q performance of this oscillator was between 200 000

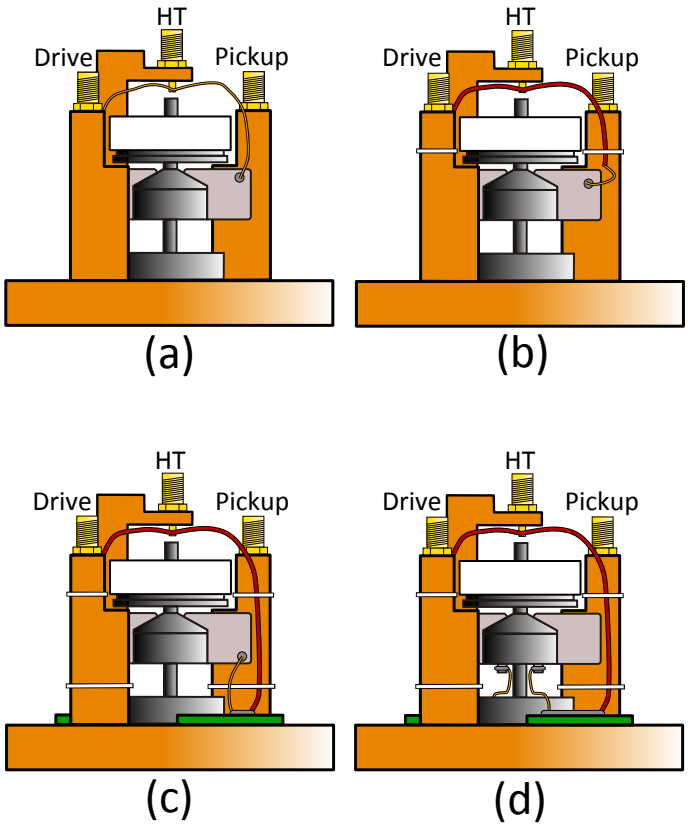

Figure 2.8: The wiring arrangements used to raise the torsional oscillator vanes to high voltage. Directly from the connector, (a), via a thicker wire secured to the posts, (b), via a PCB pad (green), (c), and to a tab on the vanes, (d).

and 250 000 at base temperature, significantly lower than that achieved by other groups. Thicker wires were tried in the same arrangement, up to 28-gauge, and the copper wire substituted for bronze and gold with no reproducible improvements.

It was believed that the length of the wires was allowing them to 'wobble' and contribute to the oscillator's dissipation. In order to shorten the length of the wires 1 mm diameter enamelled copper wire was soldered to the Microdot pin and secured to the drive and pickup posts with dental floss. The fine bare copper wire was then

soldered to this and secured to the vane, as shown in (b). This arrangement yielded poorer Q performance of $\sim$ 150 000. It was thought that the thick wire may be moving and causing loss, so a small piece of copper-clad board was fixed to the post with epoxy and the two wires soldered onto this pad. This led to no improvement in Q.

It was decided that moving the wire out to the posts reduced the oscillator's Q because it brought the wire further from the oscillator's torsion axis, necessitating greater movement and so more loss. New copper-clad boards were secured to the isolator block with brass screws. The fine bare copper wire was then run directly from the board to the vane, keeping the length of wire short, as in (c). This led to a modest improvement on the original Q to $\sim$ 350 000. When a leak developed on the torsional oscillator a new one was made with small tabs on the bottom edge of the vanes near the torsion rod, as shown in (d). The fine wire is then soldered to the pad, raised up to the vane tab near the torsion rod and wound around it, then secured with silver DAG. This arrangement allows the wire to be very close to the torsion axis, though the wire is longer than in (b) or (c). On the following cooldown the oscillator experienced stability problems, where the resonant frequency would abruptly change. There was a suspicion that this may be down to movement of the copper-clad boards on the isolator block, as the board will thermally contract more than the brass screws securing it and become lose. a small amount of vacuum

grease was applied beneath the pads to hold them fast at low temperature. On the following run the stability problems were much reduced. With the final arrangement the oscillator achieved Q in excess of 900 000, but an adsorbtion pump was fitted to the cryostat at the same time which may be partly responsible. It is possible that exchange gas left in the IVC was causing dissipation from the oscillator, but different exchange gasses used (^{3}He, ^{4}He and neon) showed no significant difference to torsional oscillator performance, and heating the oscillator plate to avoid the adsorbtion of exchange gas had no effect. In future runs the wires will be removed all together, as the oscillator is now operated with the vanes grounded, as in Fig 2.10.

The sample chamber is assembled from two pieces joined by a screw thread and sealed with Stycast 2850 epoxy. The magnesium vanes are secured into milled slots with cigarette paper coated in Stycast 1266 epoxy. The sample chamber is filled from a fill line drilled through the torsion rod 0.6 mm in diameter up to the top of the body and 0.3 mm in diameter in to the head. The oscillator is secured to a copper isolator block with a natural frequency of around 60 Hz via four brass M3 studs. These compress an indium seal joining the oscillator fill line to a hole bored in the isolator block. The CuNi fill line capillary is soldered into the bottom surface of the isolator block.

The top of the head forms an *in situ* capacitative pressure gauge. A narrow 70 µm kapton washer sits on top of the head and supports a polished silver plate.

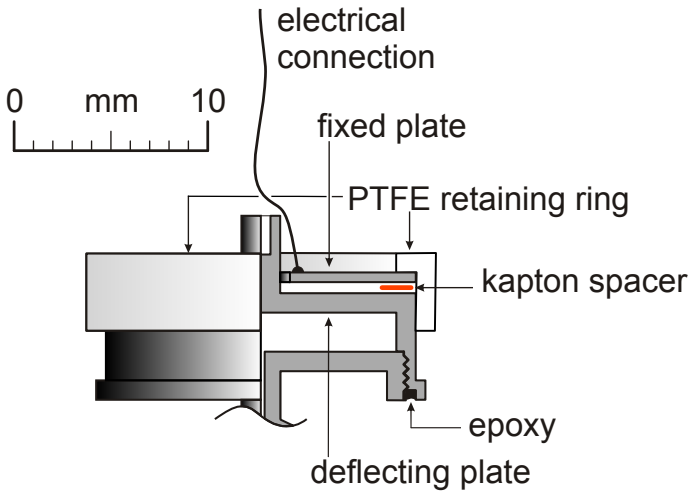

Figure 2.9: The pressure gauge assembly.

The washer is coated with a thin film of vacuum grease to stop any slippage as the cell oscillates. A fine copper wire is secured to this plate with silver DAG. It is critical that the wire be kept on the axis of the torsional oscillator, as shown in Fig. 2.9. The closer the wire is to the torsion axis the less it will move and reduce the Q of the oscillator. The assembly is held in place with a stepped PTFE ring. The thermal contraction of PTFE is much greater than that of metals, so the PTFE ring will tighten on cooling and hold the assembly rigid. The top wall of the sample chamber deflects outwards as the pressure inside the cell is raised, increasing the capacitance between the cell wall and the floating plate. This forms the capacitative arm of a back diode oscillator circuit mounted on the 1 K pot plate. The frequency of this oscillator circuit is then read out to provide a precise pressure measurement directly of the sample. Most experiments rely on remote gauges, but the ability to make a pressure measurement directly allows exact positioning on the $P-T$ phase

diagram and fine control during annealing.

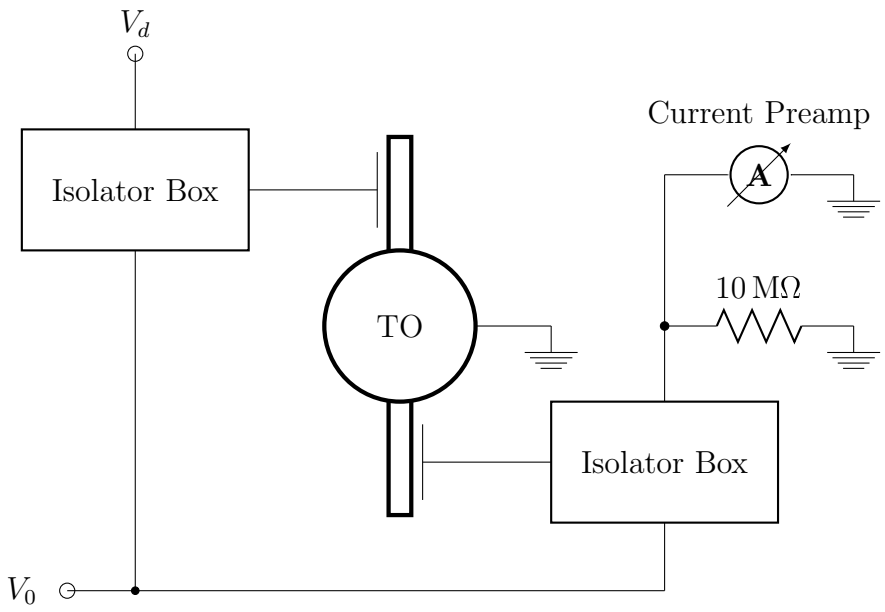

Figure 2.10: A schematic of the torsional oscillator connected in 'grounded' mode. The electrode posts are raised to high-tension V_0 and the oscillator vanes are grounded. The isolator boxes contain the circuit shown in Fig. 2.11 to add the AC signal on to the DC drive while keeping the instruments isolated from high voltages. A 10 MΩ shunt resistor is added to the input of the current preamp to dissipate any residual charge when it is switched off.

The torsional oscillator is driven by a Stanford Research Systems DS345 function generator using an Agilent 53132A frequency counter as an ultra-high stability clock. This is passed through a potential divider to bring the voltage down to achieve low enough drives. The torsional oscillator is operated in the 'grounded' configuration discussed above and shown in Fig. 2.10 in which the vanes are held at ground and the post electrodes are raised to high voltage. This has the advantage that no wires running to the oscillator vanes are needed, eliminating a source of damping from

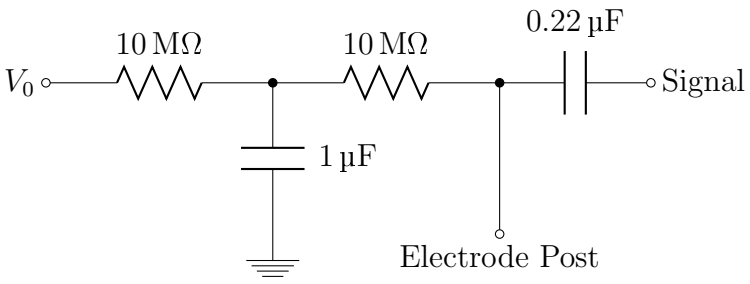

Figure 2.11: The isolator circuit used to superimpose the AC signal onto the high-tension DC at the electrode posts without damaging instrumentation.

the oscillator and improving its Q. It is however necessary to properly isolate the instruments from the high voltage, and so two isolator boxes containing the circuit shown in Fig. 2.11 are used to superimpose the AC drive on to the DC bias on the input, and to act as a high-pass filter to cut the DC bias on the output. The high voltage DC bias is provided by an Innotec LAB2K5 power supply.

The capacitor posts are cleaned and positioned by hand before each experimental run to achieve a capacitance of between 2 pF and 4 pF as this has been found to give adequate signal with little risk of the plates touching as the oscillator moves. The signal lines to and from the oscillator are superconducting coaxial cables with NbTi inners and stainless steel shields with Microdot connectors and all room temperature wiring is through coaxial cables with BNC connectors.

The oscillator response is measured using phase-sensitive detection following a Stanford Research Systems SR570 current preamplifier. We know from Eq. 2.51 that the oscillator's steady-state response to a sinusoidal drive will be a sinusoid at the same frequency as it is driven. As such we are only interested in signals

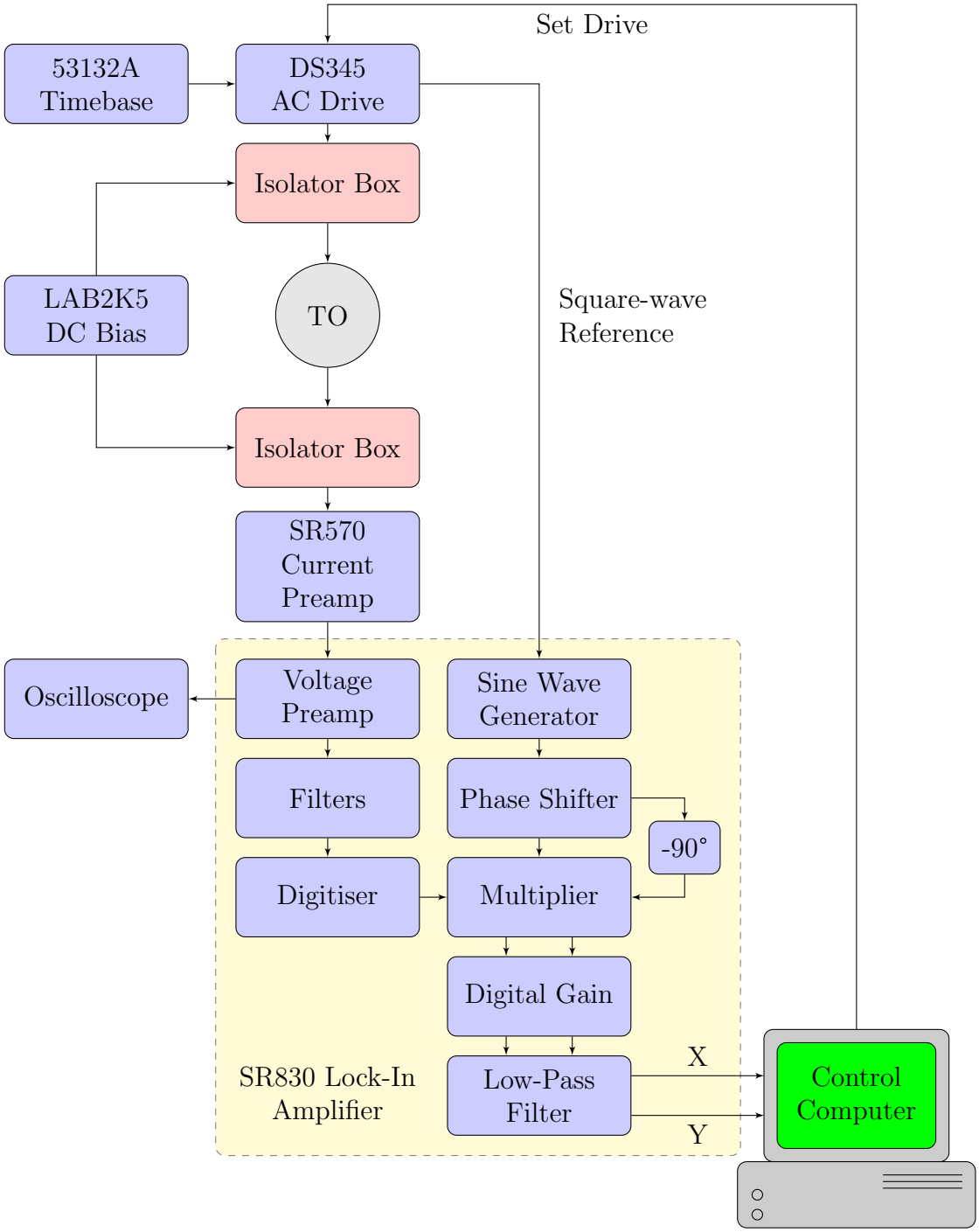

Figure 2.12: The main components of the tosional oscillator instrumentation used in this experiment.

returning from the oscillator at the drive frequency ω_d. Noise will occur at all frequencies, chiefly originating from mechanical vibrations in the laboratory as the cryostat lacks any vibration isolation. We may thus minimise the noise present in the final signal via the use of a band-pass filter centred on ω_r. This will attenuate signals at frequencies outside of the bandwidth of the filter $\omega_r \pm \delta$, so for maximum signal-to-noise we desire a very narrow bandwidth. Conventional filters may achieve narrow bandwidth but do not easily allow the centre frequency of the filter to be varied. As we are interested in following a changing resonant frequency this is a critical limitation. The solution is to use a lock-in amplifier, which can provide extremely narrow-band detection at across a wide range of frequencies [85]. Here a Stanford Research Systems SR830 two-channel digital lock-in amplifier is used.

A lock-in amplifier consists of four essential components - a sine-wave generator, a phase shifter, a multiplier and a low-pass filter [44]. The oscillator's response to sinusoidal drive will be a sinusoid at the drive frequency ω_d, phase-shifted from the drive by φ. This is equivalent to the sum of an in-phase and a quadrature signal with amplitudes R_i and R_q respectively:

$$V_{sig} = R\cos(\omega_d t + \varphi) \tag{2.69}$$

$$\equiv R_i \cos(\omega_d t) + R_q \sin(\omega_d t). \tag{2.70}$$

The lock-in amplifier generates a sine wave at frequency ω_r either from an internal

clock set by the user or an external reference. In our case the square-wave trigger output of the DS345 function generator is used. This signal can then be phase shifted by an adjustable φ_r. The input signal is then multiplied by the reference:

$$V_m = R\cos(\omega_d t + \varphi) A\cos(\omega_r t + \varphi_r) \tag{2.71}$$

$$\equiv A\cos(\omega_r t + \varphi_r)\{R_i \sin(\omega_d t) + R_q \cos(\omega_d t)\}. \tag{2.72}$$

which, given the trigonometric identities

$$\cos A \cos B = \frac{1}{2}\{\cos(A-B) + \cos(A+B)\} \tag{2.73}$$

$$\cos A \sin B = \frac{1}{2}\{\sin(A+B) - \sin(A-B)\} \tag{2.74}$$

is equivalent to

$$\begin{aligned} V_m =& \frac{AR_i}{2}\{\cos\left[(\omega_r - \omega_d)t + \varphi_r\right] + \cos\left[(\omega_r + \omega_d)t + \varphi_r\right]\} \\ &+ \frac{AR_q}{2}\{\sin\left[(\omega_r + \omega_d)t + \varphi_r\right] - \sin\left[(\omega_r - \omega_d)t - \varphi_r\right]\}. \end{aligned} \tag{2.75}$$

The multiplied signal is then passed to the low-pass filter. The low-pass filter will typically have a cutoff frequency much less than ω_r, so it will eliminate the sum frequencies, leaving the signal

$$V_{out} = \frac{AR_i}{2}\cos\left[(\omega_r - \omega_d)t + \varphi_r\right] - \frac{AR_q}{2}\sin\left[(\omega_r - \omega_d)t - \varphi_r\right]. \tag{2.76}$$

Since we are generating our reference sine wave from the trigger output of the DS345 we know that $\omega_r = \omega_d$. Thus $\omega_r - \omega_d = 0$ and our output reduces to a DC voltage

$$V_{out} = \frac{A}{2}\{R_i \cos\varphi_r - R_q \sin\varphi_r\}. \tag{2.77}$$

If we then set $\varphi_r = 0$ then

$$V_{out} = \frac{A}{2}R_i \tag{2.78}$$

and if we set $\varphi_r = -\pi/2$ then

$$V_{out} = \frac{A}{2}R_q. \tag{2.79}$$

The sine wave generator maintains the reference amplitude A such that

$$\frac{A}{2} = 1 \tag{2.80}$$

so that by choice of φ_r the output of the lock-in amplifier is either the in-phase or quadrature amplitude of the oscillator.

We now consider signals at frequencies other than ω_d, which we shall call noise of frequency ω_n. We let $d = \omega_r - \omega_n \neq 0$, remembering that $A/2 = 1$, then from Eq. 2.76 we are left with the signal

$$V_{out} = R_i \cos(dt + \varphi_r) - R_q \sin(dt - \varphi_r). \tag{2.81}$$

We recall that the low-pass filter has a cutoff frequency Δ, so it will pass all signals for which $|d| < \Delta$ and attenuate all signals for which $|d| > \Delta$. So we see that the lock-in amplifier acts as a band-pass filter with narrow bandwidth of $\omega_r \pm \Delta$ that can be easily centred on a supplied reference frequency.

The real-world implementation is inevitably more complicated, but the main features of the SR830 digital lock-in amplifier are shown inside the yellow box in Fig. 2.12. The signal from the current amplifier first enters an analogue low-noise voltage preamplifier. At this stage a monitor output is taken to an oscilloscope to observe the complete signal. A low-pass anti-aliasing filter set at the Nyquist frequency of the digitiser is required before the signal is digitised to prevent artefacts appearing from aliasing between signals at frequencies comparable to the digitiser sampling frequency. Notch filters are optionally applied at the power line frequency and double the power line frequency to remove noise picked up from the mains supply and its harmonics, but are not used in this experiment. The signal is then digitised and passed to the digital multiplier.

As the SR830 is a two-channel unit it simultaneously multiplies the signal by two reference sinusoids, one at phase φ_r and the other at $\varphi_r - \pi/2$. Because the signal is digitised and the reference sinusoids are generated digitally the SR830 uses digital multiplication, avoiding problems of noise and offset voltage that would affect analogue units. Following the multiplication digital gain is applied to the signal.

The application of gain after the multiplication allows the digital lock-in amplifier to operate with high dynamic reserve - this is its tolerance to off-frequency noise at the input. If there is a high amplitude of noise at the input the voltage preamplifier may saturate even though the signal amplitude is low. By using a low gain at the input and a high digital gain after the multiplier the signal is preserved, at the cost of greater noise introduced by the analogue-to-digital converter as it is operating on a smaller signal. The SR830 may be operated in high dynamic range mode in which the input gain is low and the digital gain is high, low noise mode in which the input gain is high and the digital gain is low, and normal mode in which they are even. Normal mode is used for this experiment as a much of the signal noise originates from mechanical 'knocks' to the oscillator, and as such is amplitude noise at the resonant frequency and larger than any electrical noise in the system. Thus there is no advantage to be had from the high dynamic range or low noise modes.

The cutoff frequency of the low-pass filter is set by specifying a time constant. We assumed in the calculation above that the signal we are interested in is a constant sinusoid, but this may not always be the case. If the amplitude of our signal changes then the signal is be described as a spread of frequencies around the signal frequency. These additional components of the signal will appear as extra terms in the multiplication, and larger changes will generate higher frequency terms. Any with frequency greater than than the cutoff frequency of the low-pass filter will be

attenuated, so only a fraction of a large change will be visible in the output signal. Since we compute an appropriate value for A based on V_{out}, the speed at which the lock-in amplifier can adapt to a changing input signal is limited by the bandwidth of the low-pass filter. Expressing the cutoff frequency Δ as a time constant $\tau_c = \frac{1}{2\pi\Delta}$ gives a more intuitively useful control, as it will take several times τ_c for V_{out} to reflect a change in the input signal. Reducing the time constant allows faster response, but as this increases the low-pass filter bandwidth it comes at the cost of more noise in the output. Low pass filters with the same cutoff frequency act on both the outputs of the multiplier.

The output of the low-pass filters are then the in-phase and quadrature outputs, denoted X and Y respectively. These may then be combined to give the absolute amplitude of the oscillator $R = \sqrt{X^2 + Y^2}$ and the phase shift of the returning signal $\varphi = \arctan\left(\frac{X}{Y}\right)$ either directly on the instrument or later in software.

We recall our solution to the amplitude of the forced harmonic oscillator in Eq. 2.47:

$$C = \frac{((\omega_0^2 - \omega_d^2) - 2ib\omega_d)\Gamma_0}{(\omega^2 - \omega_d^2)^2 + 4b^2\omega_d^2} \tag{2.82}$$

which we may rearrange to

$$\frac{C}{\Gamma_0} = \frac{\omega_0^2 - \omega_d^2}{(\omega^2 - \omega_d^2)^2 + 4b^2\omega_d^2} - i\frac{2b\omega_d}{(\omega^2 - \omega_d^2)^2 + 4b^2\omega_d^2}. \tag{2.83}$$

This shows the in-phase and quadrature response of the oscillator - we note that at $\omega_0^2 = \omega_d^2$ the first term goes to zero and the second reaches its maximum. Their lineshape is shown in Fig. 2.13.

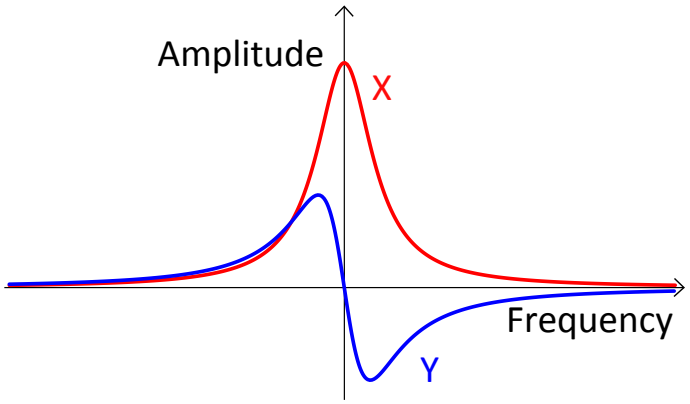

Figure 2.13: The in-phase X and quadrature Y response of the torsional oscillator as measured by two-channel lock-in detection.

2.5 The Oscillator Parameters

It is important to quantify the parameters of the torsional oscillator. We may measure the resonant frequencies of the torsional oscillator when it is empty and when it is loaded with ^{3}He and ^{4}He. From these frequencies the properties of the torsional oscillator may be deduced using Eqn. 2.65. The symmetric and antisymmetric mode frequencies are shown in table 2.1 for different samples loaded into the torsional oscillator at 250 V DC and 0.5 mV AC drive at 700 mK. It is important that figures are compared at a low AC drive where the empty oscillator behaviour does not change with drive amplitude. Using these loaded frequencies we may per-

Table 2.1: Frequencies of the oscillator loaded with different samples.

	$\omega_a/2\pi$	$\omega_s/2\pi$	Ratio ω_a/ω_s
Empty cell	1978.484 597 Hz	399.143 886 Hz	4.9568
^{3}He @ 41.5 bar	1977.787 764 Hz	398.696 627 Hz	4.9606
^{4}He @ 42.0 bar	1977.434 426 Hz	398.458 359 Hz	4.9627

form a self-consistency check. The samples contribute extra moment of inertia to the head of the oscillator, *i.e.* $M_2 \rightarrow M_2 + \Delta M$. The extra contribution is given in Table 2.2, masses are calculated from the molar volume of helium at the sample pressure extrapolated from [37].

Table 2.2: Masses and moment of inertia contributions of the samples.

	Mass m	Inertia ΔM
^{3}He @ 41.5 bar	3.941×10^{-5} kg	0.966×10^{-9} kgm^2
^{4}He @ 42.0 bar	6.127×10^{-5} kg	1.501×10^{-9} kgm^2

Substituting these additional moments of inertia and their experimentally known frequencies into equations 2.65 gives us a set of four equations in the four unknown values k_1, k_2, M_1 and M_2 for each sample loading. We can solve these to arrive at the torsional oscillator parameters in table 2.3. For comparison values for the moments of inertia are provided as calculated using a commercial CAD package.

A value for the torsion modulus G of annealed coin silver at low temperatures is not available in the literature. Angolet [60] suggests using the same value given for beryllium copper of $G = 5.3 \times 10^{10}\,\mathrm{N\,m^{-2}}$, which for a hollow rod of length l, outer

diameter d and hole diameter h has spring constant

$$k = \frac{\pi G}{32}\frac{(d^4 - h^4)}{l} \tag{2.84}$$

giving us the values of k_1 and k_2 in table 2.3. The values of the moments of inertia

Table 2.3: Calculated parameters of the torsional oscillator

	^{3}He loading	^{4}He loading	Mean	CAD	
M_1	1.4276	1.4335	1.4306	1.455	$\times 10^{-7}$kgm^2
M_2	3.2732	3.3282	3.3007	3.432	$\times 10^{-7}$kgm^2
M_2/M_1	2.2928	2.3217	2.3072	2.359	
k_1	3.3215	3.3706	3.3460	6.68	N m
k_2	13.674	13.758	13.716	21.8	N m
k_2/k_1	4.1168	4.0818	4.0992	3.26	

calculated from the sample loadings are all within 1% agreement and within 10% of the estimation of masses from CAD software. The values of k show a very poor agreement, suggesting that Angolet's assumption that $G_{\mathrm{AgCu}} \approx G_{\mathrm{BeCu}}$ is not valid. Rearranging Eqn. 2.84 and using our values of k derived from the torsional oscillator frequencies we find that at 700 mK $G_{\mathrm{Ag90Cu10}} = 3.3 \times 10^{10}\,\mathrm{N\,m^{-2}}$ after annealing.

2.6 Mass Sensitivity

Ultimately we are interested in the oscillator's mass sensitivity – that is the change in the natural frequency of a mode for a given change in a sample's moment of

inertia:

$$\frac{\partial \omega_a}{\partial M_2} \quad \text{and} \quad \frac{\partial \omega_s}{\partial M_2}. \tag{2.85}$$

It will be more convenient to discuss these sensitivities in terms of the logarithmic derivatives

$$\frac{M_2}{\omega_a}\frac{\partial \omega_a}{\partial M_2} = \frac{\partial \ln \omega_a}{\partial \ln M_2} \quad \text{and} \quad \frac{M_2}{\omega_s}\frac{\partial \omega_s}{\partial M_2} = \frac{\partial \ln \omega_s}{\partial \ln M_2}. \tag{2.86}$$

We recall the eigenfrequencies of the oscillator given in Eq. 2.65:

$$\begin{aligned} \omega_a^2 &= \frac{1}{2}\left(\frac{k_1}{M_1} + \frac{k_2}{M_1} + \frac{k_2}{M_2}\right) + \sqrt{\frac{1}{4}\left(\frac{k_1}{M_1} + \frac{k_2}{M_1} + \frac{k_2}{M_2}\right)^2 - \frac{k_1}{M_1}\frac{k_2}{M_2}} \\ \omega_s^2 &= \frac{1}{2}\left(\frac{k_1}{M_1} + \frac{k_2}{M_1} + \frac{k_2}{M_2}\right) - \sqrt{\frac{1}{4}\left(\frac{k_1}{M_1} + \frac{k_2}{M_1} + \frac{k_2}{M_2}\right)^2 - \frac{k_1}{M_1}\frac{k_2}{M_2}} \end{aligned} \tag{2.87}$$

which give the *square* of the frequencies. The derivatives of the frequencies with respect to M and k are then

$$\frac{\partial \omega}{\partial M} = \frac{1}{2\omega}\frac{\partial \omega^2}{\partial M} \quad \text{and} \quad \frac{\partial \omega}{\partial k} = \frac{1}{2\omega}\frac{\partial \omega^2}{\partial k} \tag{2.88}$$

and therefore the logarithmic derivatives are given by

$$\frac{\partial \ln \omega}{\partial \ln M} = \frac{M}{2\omega^2}\frac{\partial \omega^2}{\partial M} \quad \text{and} \quad \frac{\partial \ln \omega}{\partial \ln k} = \frac{k}{2\omega^2}\frac{\partial \omega^2}{\partial k}. \tag{2.89}$$

This leaves us with a set of eight logarithmic derivatives that describe the oscillator, but the symmetry of the frequency equations 2.65 means that

$$\frac{\partial \ln \omega_s}{\partial \ln M_{1/2}} = \frac{\partial \ln \omega_a}{\partial \ln M_{2/1}}, \quad \frac{\partial \ln \omega_a}{\partial \ln M_{1/2}} + \frac{\partial \ln \omega_s}{\partial \ln M_{1/2}} = -\frac{1}{2} \tag{2.90}$$

and

$$\frac{\partial \ln \omega_s}{\partial \ln k_{1/2}} = \frac{\partial \ln \omega_a}{\partial \ln k_{2/1}}, \quad \frac{\partial \ln \omega_a}{\partial \ln k_{1/2}} + \frac{\partial \ln \omega_s}{\partial \ln k_{1/2}} = +\frac{1}{2}. \tag{2.91}$$

As such we need only evaluate two independent logarithmic derivatives to describe the sensitivity of the oscillator to changes in mass and torsion constant, namely

$$\beta = -\frac{\partial \ln \omega_a}{\partial \ln M_2} = \frac{(\omega_2^2 - \omega_s^2)}{2(\omega_a^2 - \omega_s^2)} \tag{2.92}$$

and

$$\alpha = \frac{\partial \ln \omega_s}{\partial \ln k_1} = \frac{(\omega_a^2 - \omega_1^2)}{2(\omega_a^2 - \omega_s^2)} \tag{2.93}$$

respectively. The substitutions ω_2 and ω_1 are the characteristic frequencies

$$\omega_2 = \sqrt{\frac{k_2}{M_2}} \quad \text{and} \quad \omega_1 = \sqrt{\frac{k_1}{M_1}}. \tag{2.94}$$

In terms of these parameters the eight logarithmic derivatives are

$$\begin{aligned}
\frac{\partial \ln \omega_a}{\partial \ln M_2} &= \frac{\partial \ln \omega_s}{\partial \ln M_1} = -\beta \\
\frac{\partial \ln \omega_a}{\partial \ln M_1} &= \frac{\partial \ln \omega_s}{\partial \ln M_2} = \beta - \frac{1}{2} \\
\frac{\partial \ln \omega_a}{\partial \ln k_2} &= \frac{\partial \ln \omega_s}{\partial \ln k_1} = \alpha \\
\frac{\partial \ln \omega_a}{\partial \ln k_1} &= \frac{\partial \ln \omega_s}{\partial \ln k_2} = \frac{1}{2} - \alpha.
\end{aligned} \tag{2.95}$$

The characteristic frequencies are evaluated from the oscillator parameters in Table 2.3 and found to be

$$\begin{aligned}
\omega_1 = 4836.2 \quad &= 2\pi \times 769.71\,\mathrm{Hz} \\
\omega_2 = 6446.3 \quad &= 2\pi \times 1026.0\,\mathrm{Hz}.
\end{aligned} \tag{2.96}$$

From these and the empty cell frequencies in Table 2.1 we find α and β to be

$$\alpha = 0.442 \quad \text{and} \quad \beta = 0.119. \tag{2.97}$$

The α parameter expresses the sensitivity of the oscillator's frequency to changes in the spring constant of the torsion rods, and β its sensitivity to changes in moments of inertia. In designing torsional oscillators to detect mass flux in a sample it is thus important to minimize α while maximising β. We can explore how this may be achieved by relating α and β to the frequency ratio of the double oscillator.

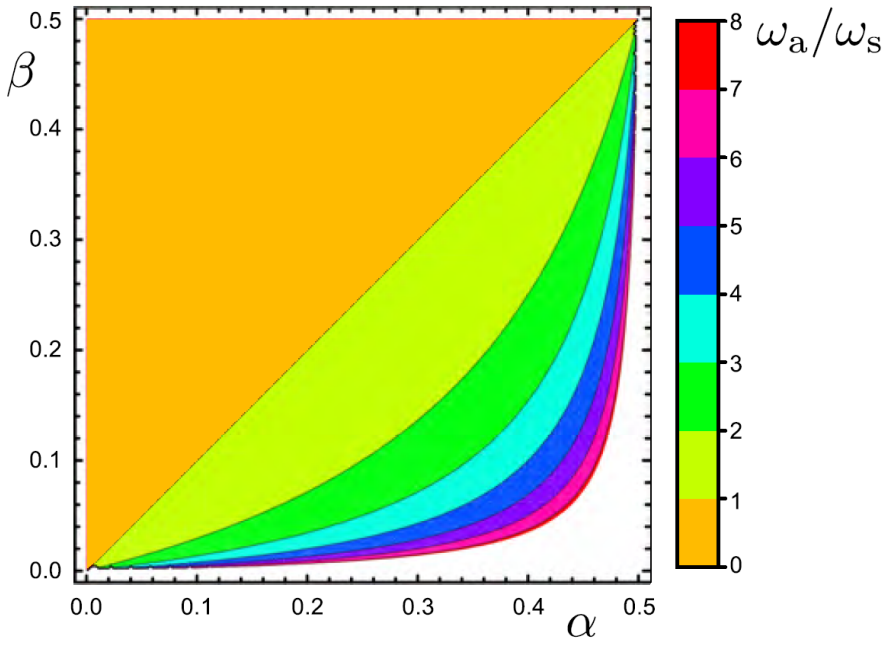

Figure 2.14: Countours of constant $\frac{\omega_a}{\omega_s}$ in the $\alpha - \beta$ plane.

We may rearrange Eqns. 2.93 and 2.92 to find the characteristic frequencies ω_1 and ω_2

$$\begin{aligned} \omega_1^2 &= \omega_a^2 + 2\alpha(\omega_a^2 - \omega_s^2) \\ \omega_2^2 &= \omega_s^2 - 2\beta(\omega_a^2 - \omega_s^2). \end{aligned} \tag{2.98}$$

From Eqn. 2.64 we know that

$$\omega_1\omega_2 = \omega_a\omega_s \tag{2.99}$$

so that

$$[\omega_a^2 + 2\alpha(\omega_a^2 - \omega_s^2)][\omega_s^2 - 2\beta(\omega_a^2 - \omega_s^2)] = \omega_a^2\omega_s^2 \tag{2.100}$$

which we can rearrange in terms of the frequency ratio

$$\left(\frac{\omega_a}{\omega_s}\right)^2 = \frac{\alpha(1-2\beta)}{\beta(1-2\alpha)}. \tag{2.101}$$

We plot contours of constant $\frac{\omega_a}{\omega_s}$ in the $\alpha - \beta$ plane in Fig. 2.14. In order to maximise β and minimise α we can see that the ratio of $\frac{\omega_a}{\omega_s}$ must be as low as possible. Solutions with $\frac{\omega_a}{\omega_s} < 1$ are unphysical, as the symmetric mode must occur at a lower frequency than the antisymmetric mode. This plot shows that there is a fundamental compromise in the design of two-mode torsional oscillators; that for the best sensitivity performance the frequencies must be as close as possible, but the chief motivation for using a two mode oscillator is to measure frequency dependence, for which a wide spread of frequencies is desirable.

Chapter 3

The Cryostat

> Other people can talk about how to expand the destiny of mankind. I just want to talk about how to fix a motorcycle. I think that what I have to say has more lasting value.
>
> *Robert M. Pirsig*
>
> Zen and the Art of Motorcycle Maintenance

3.1 The Dilution Refrigerator

The cryostat used for this experiment is a dilution refrigerator with a base temperature of around 15 mK. Originally a ^{4}He pot fridge, an Oxford Instruments 100 µW dilution stage was retrofitted in order to reach lower temperatures. The cryostat has a super-insulated nitrogen jacket which contains the helium bath.

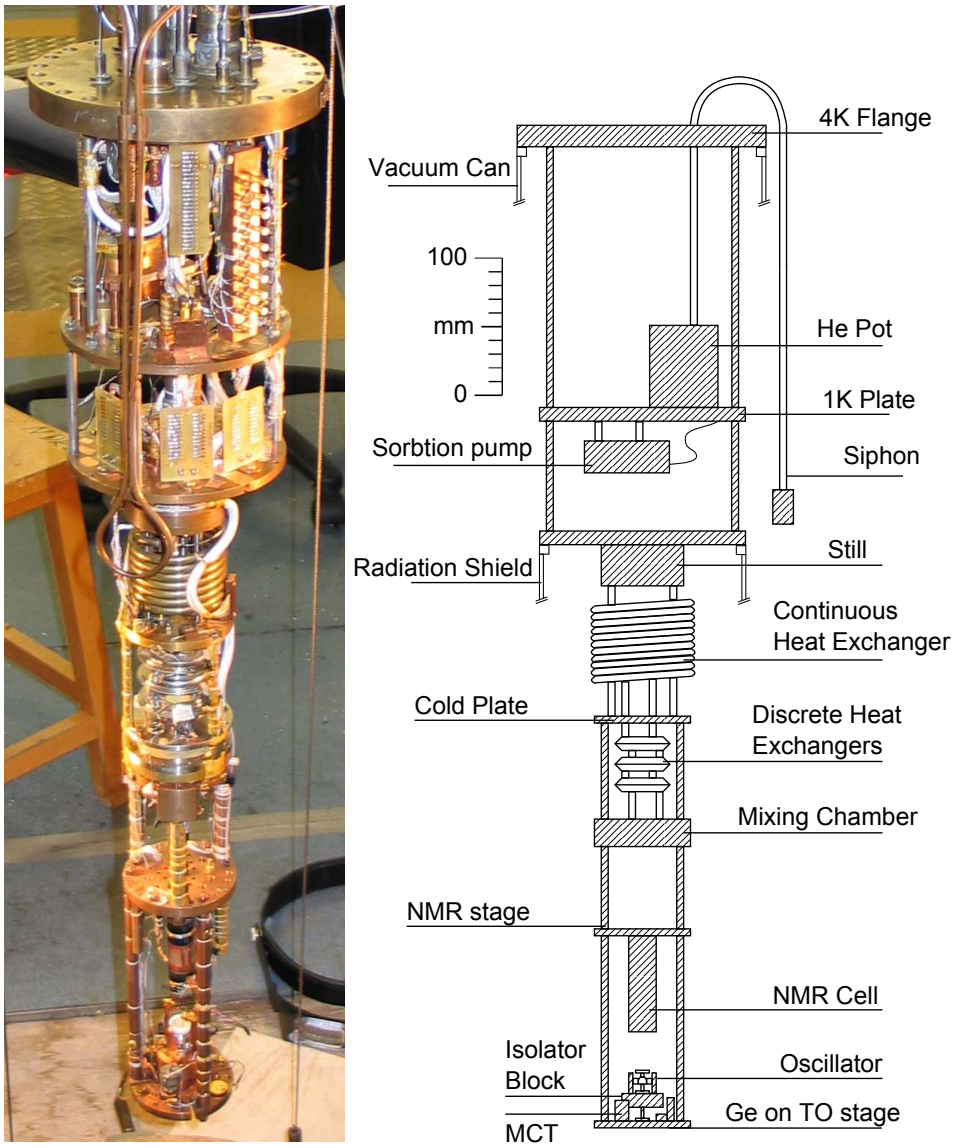

(a) (b)

Figure 3.1: The cryostat

The helium bath and nitrogen jacket are filled from storage dewars every 24 hours. A vacuum can is mounted to the 4K flange and is immersed in the helium bath. Three cold baffles minimise warming of the bath from the top-hat assembly. Below the 4 K flange is the 1 K plate which is cooled by a ^{4}He pot. Below the pot is the dilution unit (DU) which cools the experimental stage.

The dilution refrigerator exploits the phase separation of ^{4}He/^{3}He isotopes at low temperatures [59, 74]. The unit comprises a series of pipes, chambers and heat exchangers that make a long 'U'-shape running down the cryostat through which ^{3}He circulates. A flow impedance below the 1 K pot consisting of a thin capillary partially blocked by a fine wire slows the entry of ^{3}He and forces it to condense inside a chamber mounted on the 1 K plate. The liquid ^{3}He flows down the cryostat through the continuous heat exchanger, then a series of discrete heat exchangers, where it is cooled by the returning ^{3}He in solution with ^{4}He flowing up the other side of the 'U'.

The incoming ^{3}He leaves the exchanger stack and enters the top of the mixing chamber. This stainless steel cavity is packed with sinter biscuits (fine silver powder pressed and heated into a porous solid with high surface area and good thermal conductivity) tightly bolted to a copper post. This post runs through the brass base and down to screw thread, to which the experimental stage is attached. The mixing chamber contains a layer of ^{3}He floating on ^{4}He. As ^{3}He is a fermion and ^{4}He is a

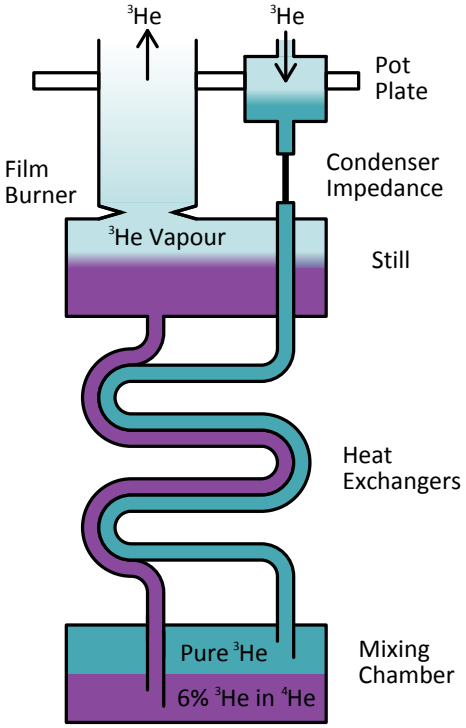

Figure 3.2: Schematic diagram of the dilution unit.

boson they obey different quantum statistics and are imiscible at low temperatures. ^{4}He has vanishingly small solubility in ^{3}He at millikelvin temperatures, and ^{4}He supports a 6% ^{3}He impurity down to absolute zero, as shown in Fig. 3.3.

A pipe enters the roof of the mixing chamber and runs from the bottom layer of ^{4}He up through the heat exchangers. Above the exchanger stack it enters the still, where a pumping line leads up and out of the IVC. Usually the still is heated, but on this cryostat heat leaks from lines thermally anchored to the still raise its temperature. The temperature difference between the mixing chamber and the still drives an osmotic flow of ^{3}He up into the still. When the ^{3}He/^{4}He mixture is correctly 'tuned' the liquid level is in the still. A polished knife-edge where the

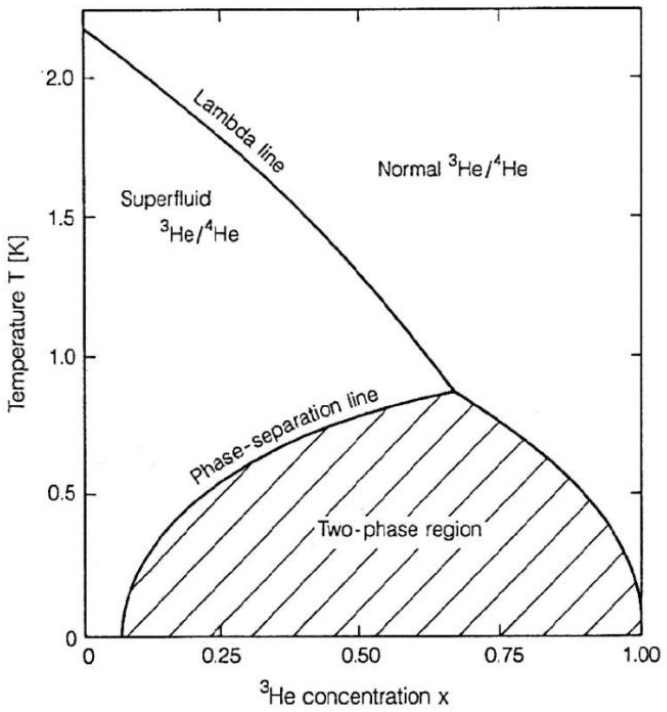

Figure 3.3: The phase diagram of liquid ^{3}He/^{4}He mixtures at saturated vapour pressure. Note the suppression of the superfluid transition, the phase separation of the mixture below 0.8 K and the finite solubility of ^{3}He in ^{4}He at $T \to 0$ K. Taken from Pobell [74].

pumping line enters the roof of the still prevents superfluid film climbing up the walls of the line and evaporating. In more modern cryostat designs this is usually a series of concentric pipes or a heated element known as a film burner.

^{3}He evaporates preferentially when the still is pumped on due to its lower mass. By removing ^{3}He from solution in the still, more is drawn up from the mixing chamber via osmotic pressure. This drives a flow across the phase boundary from the pure ^{3}He layer into solution in ^{4}He. This is analogous to evaporative cooling - atoms undergo a change from a concentrated phase to a dilute phase with a corresponding

change in enthalpy producing cooling at the phase boundary. A crucial difference being the requirement to maintain a 6% ^{3}He impurity in the dilute phase all the way to absolute zero, meaning that an ideal dilution refrigerator does not lose cooling power altogether at low temperatures.

The ^{3}He is pumped by a 'booster' vacuum pump, usually a high-throughput oil-mist diffusion pump or a Roots pump, backed by a sealed rotary pump. This cryostat uses an Edwards EO4 high-vacuum diffusion pump backed by an Alcatel two-stage sealed rotary pump. The pumped ^{3}He is sent through a Gas Handling System (GHS) to a charcoal nitrogen trap which freezes out any impurities such as air that may have leaked into the system, and a helium trap which freezes out any hydrogen that may have been released from cracking processes in the pump oil as it degrades. The cleaned mixture goes through a flow meter to monitor circulation, then into the dewar and a final U-bend trap in the helium bath and lastly into the IVC where it condenses again at the 1 K pot stage.

We may follow Pobell [74] to calculate the cooling power of the dilution refrigerator. From measurements of the specific heat of ^{3}He/^{4}He mixtures we know that the enthalpy ^3H_d of ^{3}He diluted in ^{4}He is larger than that of pure ^{3}He, ^3H_c [91, 3]. We can thus define a *heat of mixing* for $\dot{n}_3$ moles of ^{3}He

$$\dot{Q} = \dot{n}_3(H_d(T) - H_c(T)). \tag{3.1}$$

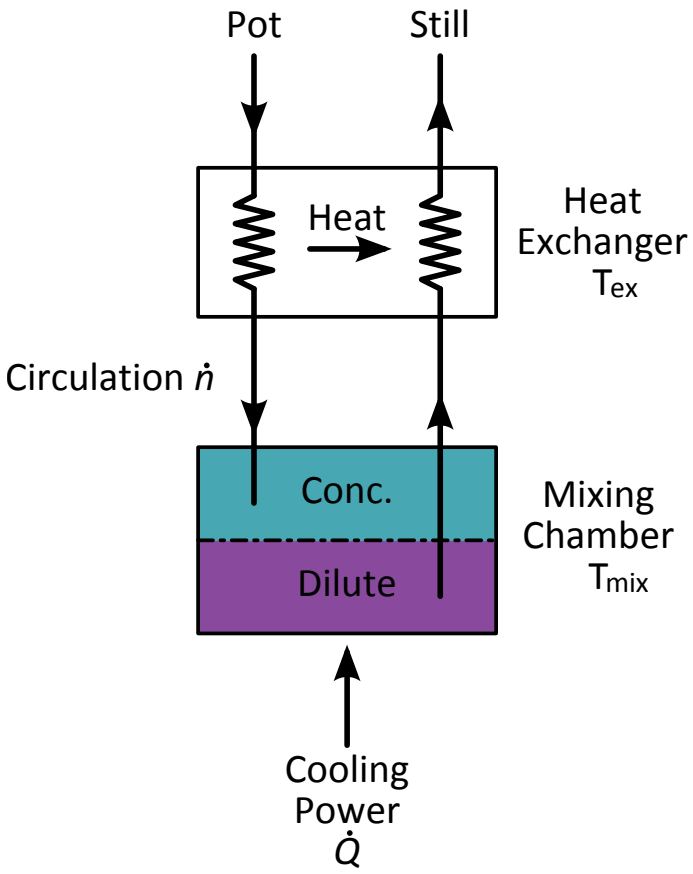

Figure 3.4: Heat flow in the dilution unit.

As the enthalpy of a system is given by the integral of its heat capacity C

$$H(T) - H(0) = \int_0^T C(T)dT \tag{3.2}$$

and we know from experimental data by Greywall [35, 34] that the heat capacity of ^{3}He liquid at the saturated vapour pressure below 40 mK is approximately

$$C_3 \approx 22T \text{ J mol}^{-1} \text{ K}^{-1} \tag{3.3}$$

(as a strongly interacting Fermi liquid calculating this value is difficult). Thus the enthalpy of concentrated liquid ^{3}He at low temperature is

$$^3H_c = {}^3H(0) + 11T^2 \text{ J mol}^{-1}. \tag{3.4}$$

In the mixing chamber we have a mixture of 6% ^{3}He in solution in ^{4}He. This is sufficiently low a concentration to consider the ^{3}He a weakly interacting Fermi liquid, where we may make a good approximation by the substitution of an effective mass. This allows us to derive a a specific heat of a 6% mixture as

$$^3C_d(6\%) \simeq 106T \text{ J mol}^{-1} \text{ K}^{-1}. \tag{3.5}$$

In equilibrium the chemical potential of the dilute and concentrated phases must be equal. As $\mu = H - TS$ then

$$^3H_c - T \times {}^3S_c = {}^3H_d - T \times {}^3S_d \tag{3.6}$$

from which follows

$$^3H_d(T) = {}^3H_c(0) + 11T^2 + T\int_0^T \left(\frac{^3C_d}{T'} - \frac{^3C_c}{T'}\right) dT' \tag{3.7}$$

$$= {}^3H_c(0) + 95T^2 \text{J mol}^{-1}. \tag{3.8}$$

We now consider the enthalpy balance in Fig. 3.1. For $\dot{n}_3$ mole of ^{3}He circulating through the dilution unit

$$\dot{n}_3(^3H_d(T_{mix}) - {}^3H_c(T_{mix})) = \dot{n}_3(^3H_c(T_{ex}) - {}^3H_c(T_{ex})) + \dot{Q} \tag{3.9}$$

Where T_{mix} is the temperature of the mixing chamber and T_{ex} is the temperature of the heat exchanger. Rearranging for $\dot{Q}$ and substituting in our results 3.4 and 3.8 we can see that the cooling power of the dilution unit is given by

$$\dot{Q} = \dot{n}_3(95T_{mc}^2 - 11T_{ex}^2) \text{ W}. \tag{3.10}$$

This shows how important properly cooling the condensing stream of ^{3}He is to good operation of the dilution unit - the heat load entering the mixing chamber at the bottom of the 'U' limits the cooling power and thus the minimum temperature of the refrigerator. At low temperatures the mismatch in phonon velocity between the liquid helium and surrounding metal leads to extremely high thermal boundary resistance, known as Kapitza resistance, which goes as T^{-3} [74]. The common solution to this is to provide the highest possible surface area of metal for heat transport.

The continuous exchanger consists of a large brass pipe containing a finer capillary wound tightly inside. The viscous condensing stream in the brass pipe is thus

cooled by the contraflowing returning stream in the capillary. The continuous heat exchanger terminates at the cold plate which is packed with sinter to thermalise it. This plate provides a last thermal anchor for lines running down the cryostat before the mixing chamber. The discrete exchangers are flat split rings of stainless steel divided into upper and lower chambers for the two streams by a thin CuNi foil. Silver sinter biscuits are bonded to either side of the foil giving the maximum possible surface area for heat exchange.

In practice the cooling is limited by their ability to cool the incoming ^{3}He stream to around 10 mK in commercial units and almost 1 mK in specialist units [19]. At the lowest temperatures turbulence in the viscous ^{3}He flow will cause appreciable heating around the exchangers, practically limiting base temperature. Base temperature may also be limited by chemical or oil contamination, physical problems such as a poorly prepared sinter, or a cross-leak between the condensing and pumping streams. If the cryostat is leaking and helium is entering the IVC a superfluid film may thermally 'short' stages and carry heat load down the DU, or poorly anchored wiring and fill lines may carry heat down the cryostat. The correct concentration and quantity of ^{3}He/^{4}He mixture (commonly referred to as 'mash') varies widely between cryostat designs and is vital for good operation. If the phase boundary occurs outside the mixing chamber cooling power will be severely reduced due to poor thermal contact and small area of the phase boundary, and be highly sensitive to changes in

concentration. If the liquid level is not high enough to enter the still there will be insufficient surface area for good pumping. If the still is below 600 mK the liquid will be too cold to achieve good ^{3}He circulation, and if it is over 800 mK ^{4}He will evaporate and start circulating with the ^{3}He. Similarly if the still is over-full or the film burner is not working a superfluid film will climb up the walls of the pumping line to warmer parts of the cryostat where it will evaporate and circulate with the ^{3}He. If ^{4}He enters circulation it must be recondensed, causing an additional heat load without any contribution to cooling.

Temperatures on this cryostat were originally monitored with Speer and Alan-Bradley carbon resistors. Because these were of different values and their calibrations were of poor quality they were replaced with surface-mount ruthenium dioxide resistors (see below). As ruthenium dioxide has very poor thermal conductivity the resistors are cooled through their copper leads which are thermally anchored to the cryostat. CuNi-clad NiTi superconducting loom runs from the copper leads to connector pads mounted to the underside of the 4 K flange, and then constantan wires run up an IVC pumping line to hermetically sealed 24-way Fischer connectors above the top-hat where they are read via a 2-wire measurement using a home-made scanner controlled by the computer and a Stanford SIM921 AC resistance bridge. Two wire measurement is sufficient for these monitoring resistors as the resistance of the constantan and superconducting leads varies very little and allows more ther-

mometers from the available wiring on the cryostat. Where resistors are required for experiment thermometry they are used in 4-wire configuration to eliminate lead resistance.

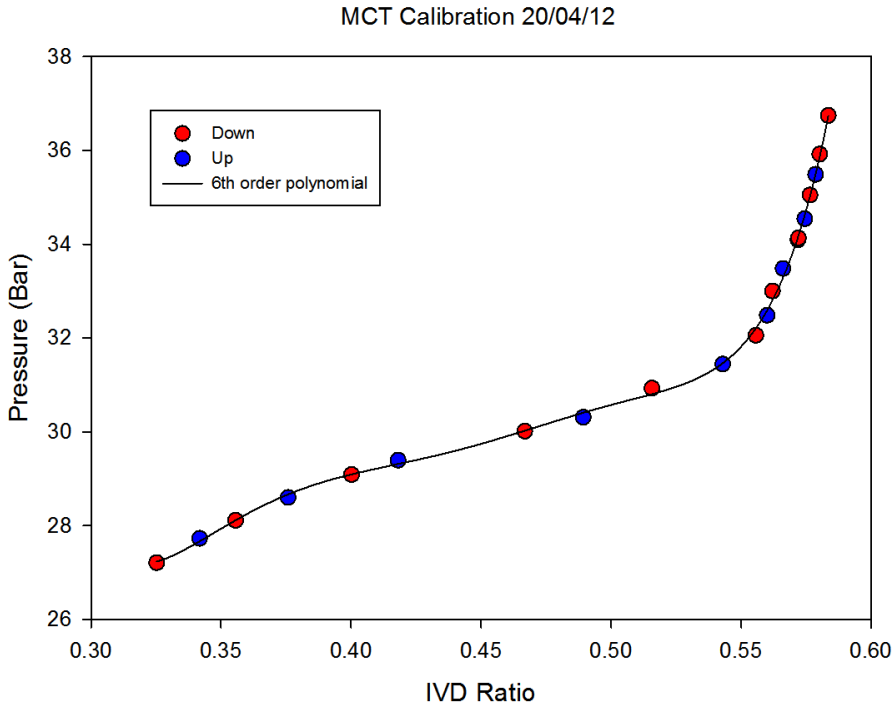

Figure 3.5: A calibration curve of the original MCT showing the poor stress-strain relationship. The cell has poor sensitivity at higher pressures, and shows significant hysteresis between raising (blue points) and lowering (red points) the pressure. A 6^{th} order polynomial is fitted to the calibration sweeps.

The torsional oscillator stage is held on black nylon washers to thermally isolate it from the DU. Copper braids run from posts coming from the DU on to the TO plate, allowing the thermal anchoring of the plate to be adjusted between runs. The temperature of the plate is regulated using an aluminium strain gauge as a heater and a calibrated germanium resistor as a main thermometer, read via a 4-wire

measurement by a dedicated Stanford SIM921 AC bridge. A Stanford SIM 960 PID controller applies heat to stabilise at temperature setpoints sent from the control computer via a LabVIEW vi. In addition to the germanium and RuO_2 resistors a ^{3}He Melting Curve Thermometer (MCT) is mounted on the TO plate. This is a Straty-Adams-type pressure gauge made from beryllium copper that capacitatively measures the deflection of a membrane caused by pressure changes in a cell filled with ultra-pure ^{3}He. On cooling the cryostat to pot temperature its pressure response is calibrated and it is charged to 35.5 bar using a dipping bomb before starting the dilution unit. The fill line will block on reaching around 800 mK and the liquid ^{3}He in the cell will start to freeze. If the cell was loaded correctly a mixture of solid and liquid will persist in the cell and its pressure will follow the ^{3}He melting curve, from which the temperature of the cell may be accurately inferred. The pressure of the MCT cell is read out by measuring the capacitance of the cell as one arm of a bridge circuit, the other being a reference capacitor mounted on the 1 K plate. An inductive voltage divider controlled by the computer is used to balance the bridge circuit using a lock-in amplifier as a null-detector.

The MCT cell mounted on the cryostat at the start of the experiment had a poor stress-strain curve, shown in Fig. 3.5 and showed hysteresis between expanding and contracting, so this was replaced with a new cell provided by the Low Temperature Physics group at Kharkov. This cell has a more linear response and shows no

significant hysteresis, shown in Fig. 3.6.

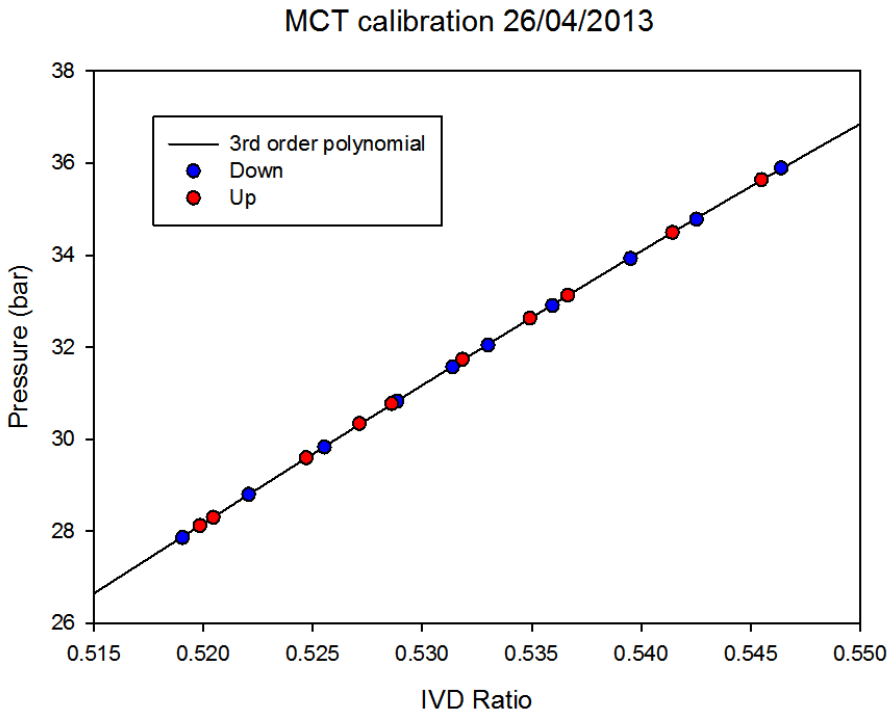

Figure 3.6: A calibration curve of the replacement MCT. This cell has an almost linear response and so requires only a 3rd order polynomial to fit the calibration curve.

On this cryostat cooling is limited to around 19 mK, most likely due to an inadequate booster pump. This was poorly chosen when the cryostat was designed as it is a high-vacuum rather than a high-throughput pump. Diffusion pumps rely on a circulating stream of oil vapour to deflect gas particles and drive them through the body of the pump. When the still is heated slightly the pressure in the still pumping line is seen to fluctuate as the higher throughput causes the pump to 'stall' as the flow of gas disrupts the oil circulation. This failure of the pump prevents us achieving ^{3}He circulation rates above 60 µmol s^{-1} which is low for this design of cryostat.

A full overhaul of the cryostat will replace this pump, and fit an improved mixing chamber base for better thermal contact to the experimental stage.

3.2 Repairing the Dilution Unit

Early in the project an accident caused a pressure gauge to break off the still line and a large amount of air to be pulled in. This froze and formed a plug in the still line. When the cryostat was warmed the helium mixture in the DU boiled and the build-up of pressure between the plug and the impedance ruptured two of the discrete heat exchangers. It was decided that the heat exchangers could be repaired, but would need to be removed. Support brackets were made up to hold the experimental stage while the indium seal joining the discrete exchanger stack to the cold plate was broken. Once the cryostat was split at this point the bottom half was lowered and the mixing chamber was heated with a blow torch to melt the solder joints between the exchanger stack an the mixing chamber. The stack was lifted clear of the mixing chamber and the ruptures were soldered closed with eutectic solder on the bench. The connections to the mixing chamber at the bottom of the stack were plugged and tubes made up with indium seal flanges to match the connections at the top were fabricated. These tubes were soldered into Klein Flanges (KF) at the other end for leak testing. The exchangers were leak tested by pumping on either side with the leak detector and spraying the outside with helium gas. To check for cross-leaks

the other side of the exchangers were flushed with helium. The exchangers were immersed in a liquid helium bath and the tests repeated at 4 K to see if leaks would open at low temperature due to thermal contraction. Blanking plates were made up to fit the exposed indium seals on the cryostat to close the two sides of the DU. The cryostat was pumped and leak tested and found to be leak tight.

The exchangers were refitted using Woods metal to avoid excessive heating of the mixing chamber. The cryostat was lifted on the support brackets and the indium seals were made up. The cryostat was found to be leak tight down to 4 K, but when the dilution unit was started it could not cool below 180 mK. On warming back up, a significant amount of helium was found inside the IVC, indicating the presence of a superfluid leak, or 'superleak'.

A superleak is a flow channel too small to allow measurable leak rates to normal fluids, but is open to superfluids. Due to the superfluid property of zero viscosity a significant amount of ^{4}He may pass through the apparently leak-tight barrier when it is cooled below the λ transition. No leak appeared after the pot had been cooled without admitting any mash, so the leak must have been on the DU. The Woods metal joints were reflowed and the indium seals were split, cleaned and remade, with several small scratches polished out. The cryostat was cooled again to 1.5 K and held there for 8 hours. It was then warmed to 5 K, where the IVC was pumped with a turbomolecular pump backed by a leak detector to establish a background helium

signal (no leak signal is visible below 4.2 K as any ^{4}He present is being strongly cryopumped). This process was repeated with mash admitted to the DU and the unit was found to be leaking at pot temperature.

To isolate the leak, thin film aluminium strain gauges (used as small heaters) and RuO_2 thermometer resistors were mounted to each heat exchanger, the cold plate and the mixing chamber so that they could be heated and monitored independently. To aid diagnostics all the Speer and Allen-Bradley resistors were replaced by 1.2 kΩ RuO_2 surface mount resistors. By using nominally identical high-quality resistors selected from one batch throughout the cryostat it is simple to make qualitative comparisons between the temperature of different components. All resistors were thermally cycled ten times in liquid nitrogen after soldering and tested by immersing in liquid helium. Any that differed by more than 1% from the others were replaced. One resistor was fitted to the experimental stage and calibrated against the Lakeshore germanium resistor and MCT (shown in Fig. 3.7). On a log-log plot the behaviour of the RuO_2 resistors is essentially linear below 1 K, making them convenient monitoring resistors. Below 30 mK the RuO_2 resistors become unreliable as conduction freezes out and resistance diverges. This generic calibration was then applied to all the resistors to provide approximate thermometry throughout the cryostat. The thermal conductivity of RuO_2 is vanishingly small at low temperatures, so these are soldered to short sections of enameled 36-gauge copper wire to

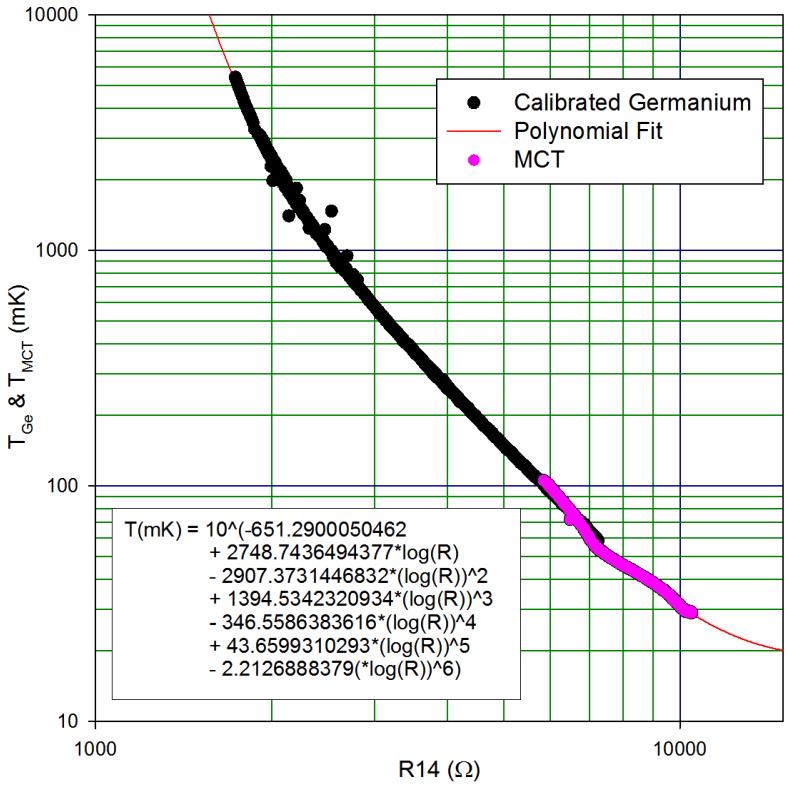

Figure 3.7: Generic calibration applied to all RuO_2 resistors. The MCT (pink data points) is used at temperatures below the limit of the germanium thermometer (black data points). In the vicinity of the melting curve minimum the MCT becomes insensitive, so the germanium is used for higher temperatures.

thermalise the resistors through their leads. This copper wire is then wound around a copper post or held under a copper tab in good contact with the plate it measures. On the exchanger stack the copper leads are wound around the tubes connecting exchangers. Mash was condensed into the DU with the pot while the mixing chamber and heat exchangers were heated, restricting the region in which helium could go superfluid. By reducing the heat on individual exchangers this superfluid region could be lowered down the cryostat so that a superleak could only occur between the pot and some known point inferred from the temperatures of the exchangers. Over many successive runs down to pot temperature and warm-ups back to 5 K to test the contents of the IVC, the superfluid region was allowed further down the cryostat, until a leak appeared when it was admitted into the exchanger stack. This procedure was extremely challenging due to the high thermal conductivity of the superfluid, poor thermalisation of resistors and the difficulty in maintaining the delicate equilibrium of heaters for the 8 hours required to allow the leak to build up to measurable levels. These difficulties made it impossible to isolate one individual exchanger as the source of problem.

Attempts were made to reflow the repaired joints *in situ* but these were unsuccessful. It was suggested that the cryostat might be able to run while leaking if an adsorbtion pump (sorb) could be fitted to stop stray helium thermally shorting the DU. Such pumps use a large surface area of a material such as carbon to which

helium will bond when cooled. A large sorb was made, holding 12 g of activated charcoal in a copper cylinder, held back by copper mesh. A constantan wire was wound around the cylinder to act as a heater for desorbing the pump and an Allen Bradley carbon resistor calibrated using the PPMS monitors the temperature. It was wrapped in superinsulating silvered mylar and fastened under the pot plate with a stainless steel bracket and nylon screws to thermally isolate it. 10 cm of fine copper wire provide a thermal link to the pot plate. This assembly allowed the sorb to be heated to over 30 K, expelling the adsorbed helium to be pumped away, and cool back down without warming the rest of the cryostat above 4 K. Though the sorb was shown to work as planned, running for several weeks without saturating, the base temperature did not improve. It was suspected that there may be a cross-leak between the contraflowing streams in the exchangers, or some physical damage to the sinter.

Eventually a decision was made to replace the exchanger stack. The cryostat was again split at the cold plate, the experimental stage was lowered and the stack removed, this time together with the mixing chamber. The stack and mixing chamber were sent to Oxford Instruments where a new stack was prepared, mounted to the mixing chamber and leak tested. Minor adjustments had to be made as although the placing of ports is the same in modern OI units the flow direction is reversed. The new stack was mounted and the cryostat circulated with no leaks, but could

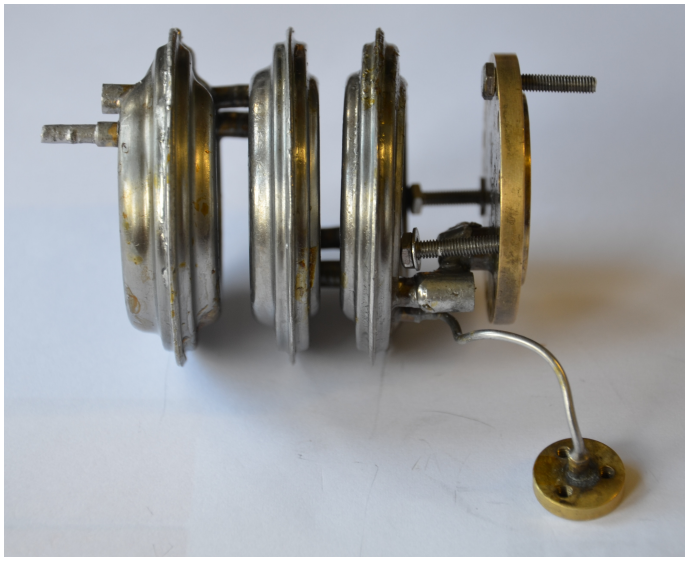

Figure 3.8: The old heat exchanger stack, removed from the cryostat. The two pipes leading into the mixing chamber are on the left. The returning stream leaves through the large flange on the right, joined into the bottom of the cold plate. The condensing stream enters the exchangers through the small flange, bottom right. Note the reflowed solder join on the left-most exchanger.

not cool below 80 mK.

3.3 Tuning the Mash

Some amount of ^{3}He/^{4}He mixture was lost during the accident, so an imbalance in the mash was the first candidate for the cryostat's poor performance. The total quantity was inferred from the dump pressure and volume as 80 l. A leak detector was used to measure the concentration, as follows:

A brass disc was made up to fit in the recess in KF16 Klein Flange, with a 2 mm hole drilled through the centre. This supported a thin sheet of polythene behind an O-ring, made gas-tight with vacuum grease. Polythene is somewhat permeable to helium, so this assembly shown in Fig. 3.9 made a 'test leak' through which the mash could be sampled by the leak detector. This test system was calibrated by admitting a shot of pure ^{3}He measured out between two valves from a sample gas bottle, then pumped out and repeated for ^{4}He using a bladder filled with boiled-off helium gas collected from a dewar. These leak rate values (1.6×10^{-6} and 5.4×10^{-7} mbar L s^{-1} respectively) were scaled by the pressure behind the leak during the measurement (always kept at approximately 150 mbar). A small amount of ^{3}He/^{4}He mixture was then admitted from the dumps and the pressure and ^{3}He leak rate were measured. Dividing the mixture leak rates, normalised by pressure, by the calibration values returned a ^{3}He abundance of 17%. To check this value the ^{4}He leak rate was also measured, and the concentration was found to be 85%. These values are sufficiently consistent to be confident in a concentration measurement of $16 \pm 2\%$ ^{3}He.

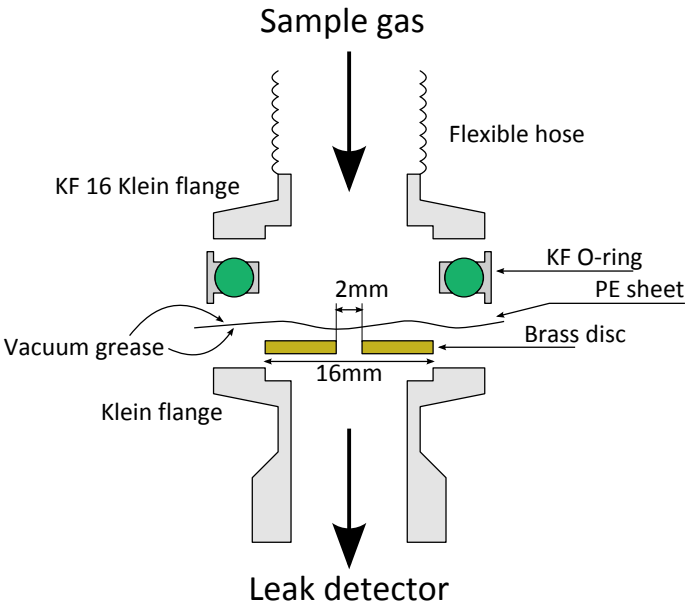

Figure 3.9: Exploded cross section of the control leak used to measure the mash concentraion.

When a dilution refrigerator is running well all the ^{4}He in the mixture is condensed into the DU and only ^{3}He circulates. This means that the required amount of ^{4}He depends only on the internal geometry of the unit. By examining the original blueprints of the DU the internal volume of the components can be easily calculated. ^{4}He should occupy most of the mixing chamber, half of the discrete heat exchangers and around half of the still. A small correction must be made for the packing fraction of the sinter, assumed to be 0.5, and the volume of the continuous exchanger capillary is negligible. This established a range of liquid ^{4}He volume that would allow the cryostat to operate, from the still almost empty to the still almost full. The mixing chamber provides some 'buffer' in the working range of concentration, and was assumed to be half full of ^{4}He. The quantity of ^{4}He remaining in the dumps was

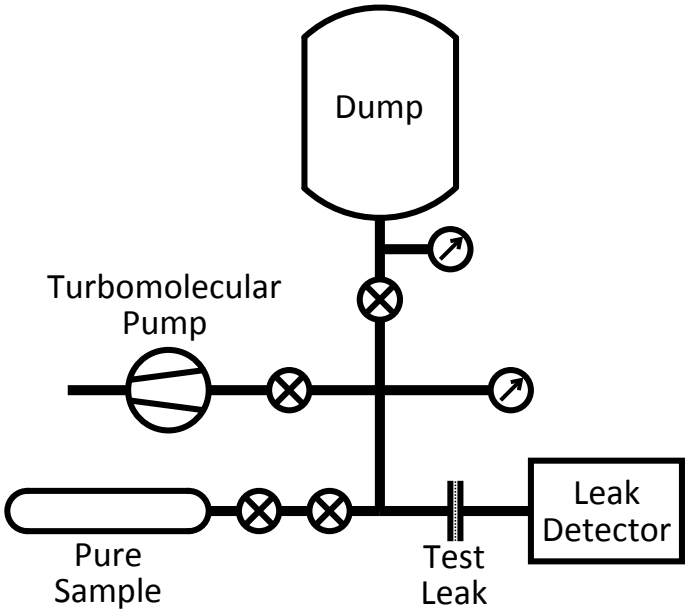

Figure 3.10: The gas handling system used to measure the isotopic composition of the mash.

found to be slightly in excess of this, presumably from a poor original set up, so 6l of ^{4}He gas were removed. The required quantity of ^{3}He is more difficult to calculate as it depends on the volume and pressure (and temperature) of traps, pumps and the GHS used, but unlike the ^{4}He quantity it can be easily tuned while the cryostat is circulating.

The overall volume of liquid was checked by heating the still. Once liquid has entered the still it will stabilise its temperature, as any heat applied will go to boiling off liquid. By adding mixture in steps and running the still heater we were able to determine when the liquid level has risen into the still. Knowing the volume of gas remaining and the volume of the still we were able to adjust the mash to keep the still approximately half full.

To test the mash concentration a series of 'one-shot' runs were made. By closing the circulation off to the condenser line and sending the returning ^{3}He to the dumps the heat load on the mixing chamber is eliminated. In a 'healthy' refrigerator the ^{3}He will continue to be pumped out from the still, but the liquid left on the condenser side will gradually become depleted. There should be immediate cooling below the normal minimum temperature of the unit as the heat load of the condensing stream is removed, then as the ^{3}He is pumped away the phase boundary will move up the condenser side of the unit and leave the mixing chamber. At this point the cooling will stop as there is no longer good thermal contact between the phase boundary and the unit and the unit will start to warm. If the unit is running too 'rich' in ^{3}He the phase boundary will be up in the still-side. The one-shot will move it slowly down into the chamber, and the cryostat will cool sharply after a long delay. If the cryostat is running 'lean' the phase boundary is too high in the condenser-side. In this case the phase boundary will never enter the mixing chamber during the one-shot, and there will be no cooling [80]. In practice this diagnostic is more complicated as the circulation $\dot{n}$ must not change during the test, as this will change the cooling power. When the condensing stream is stopped there is less heat load on the still, so it will cool and less ^{3}He will be pumped away. Thus the still temperature must be carefully regulated to maintain a constant flow of ^{3}He out of the DU.

The cryostat showed no cooling when a one-shot was performed, so was assumed

to be ^{3}He lean. ^{3}He was added to the circulation from a 50% ^{3}He/^{4}He mixture used in another experiment, 1 l of gas at a time. This increased the overall ^{3}He concentration and the one-shot test was repeated. After adding 6 l of 50/50 mixture in this fashion strong pressure and temperature oscillations were observed in the still. This was interpreted as the still overfilling and the liquid level oscillating in the still line, and so 4 l ^{4}He was removed to reduce the overall liquid level. While the still is cold ($\lesssim 800$ mK) the pumped gas is nearly pure ^{3}He, so by keeping the still cold throughout a one-shot nearly all the ^{3}He may be removed. The temperature will then rise sharply as there is no dilution cooling as only ^{4}He remains in the DU. By diverting an amount of gas pumped after this temperature rise near pure ^{4}He may be removed from the mash.

To expedite the process it was decided to add ^{3}He from a pure (99.9% isotopic purity) sample bottle. After adding a further 4 l of ^{3}He the temperature rose sharply to 150 mK. A one-shot produced a slight cooling after a delay, so this was interpreted as an excess of ^{3}He. This implies that we had passed through the correct concentration and that another factor was preventing the cryostat from cooling. 3 l of ^{3}He were thus removed to reach a final mash load of 78 l of 22% ^{3}He, with the most likely factor preventing cooling being a heat leak.

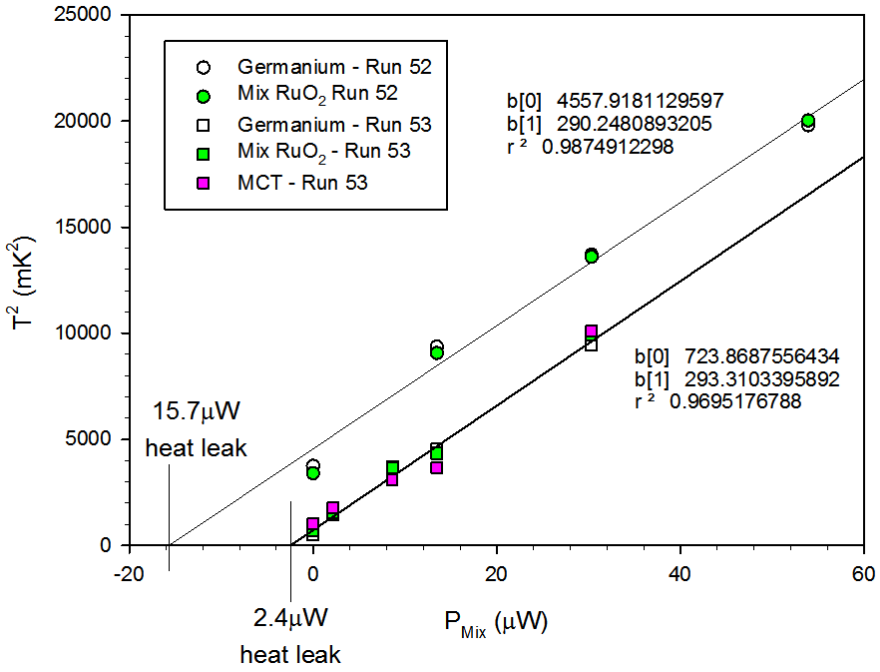

Figure 3.11: Evaluation of cooling performance before (circles) and after (squares) eliminating the heat leak.

3.4 Finding the Heat Leak

A cooling power test was performed in which the temperature of the DU was measured as a function of heating power applied to the mixing chamber. 3l of ^{3}He was removed to return the phase boundary to the mixing chamber and the cryostat was cooled to its base temperature. Voltage was applied to a constantan wire of known resistance wrapped around the mixing chamber to heat the DU at a known power.

As we saw in Eq. 3.10 the cooling power of a dilution unit $\dot{Q}$ goes as the square of temperature. This means that plotting T^2 vs. applied heating power a well-behaved unit should show a linear response. The intercept of such a plot then represents the

heat leaking into the unit. By measuring the temperature of the unit while heating the mixing chamber we were able to ascertain that the unit had a 15.7 µW heat leak, shown in Fig. 3.11. For reference, the refrigerator is rated as having 100 µW of cooling power at 100 mK, and will have much less at base temperature. We can put an upper limit on the cooling power of the unit at a given temperature if we assume that heat exchangers are working perfectly, *i.e.* the lower exchanger is at the same temperature as the mixing chamber. The temperature of the exchangers are at the limit of resistive thermometry, but the RuO_2 thermometers show this to be a reasonable approximation. Taking equation 3.10 with $T_{mix} = T_{ex}$

$$\dot{Q}_{max} = 84\dot{n}_3 T_{mix}^2 \tag{3.11}$$

then at the cryostat's rated base temperature of 10 mK and a reasonable circulation of 100 µmol s^{-1} the maximum cooling power available is less than a microwatt.

Calculations were made of the heat load of potential sources of a heat leak, *e.g.* a copper wire accidentally used in place of a CuNi one, a superfluid film running down the cryostat or a touch between the radiation shield and one of the stages. The most likely candidate was found to be an alloy wire incorrectly heatsunk or a alloy wire used in place of a superconducting one. As such all non-critical wiring was removed from the cryostat. Wiring looms, coaxial cables and the fill lines to the TO and NMR cells were disconnected from their connectors and wound up into the

space between the 4 K flange and the pot plate. Only the germanium, MCT and one RuO_2 resistor were left connected to provide thermometry. Unused ports through the 4 K flange were covered with copper shields and screw holes and slots on the various stages were covered with copper tape to block thermal radiation. Because the support rods around the heat exchanger stack had been removed and refitted with different washers to adjust the spacing there was a concern that differential cooling of the rods may cause the cryostat to go out of alignment with the radiation shield secured to the still plate and potentially touch it. This would provide a metal-to-metal contact between the radiation shield at $\sim$ 600 mK and the mixing chamber, and so a disastrous heat leak. A PTFE spacer was fitted to the bottom of the experimental stage to prevent the stage directly touching the shield if it were to go out of alignment.

On cool down the cryostat achieved 29 mK and a repeat of the cooling performance test showed a vastly improved residual heat leak of 2.4 µW. Rearranging equation 3.11 to give the minimum temperature

$$T_{min} = \left(\frac{\dot{Q}_{load}}{84\dot{n}_3} \right)^{1/2} \tag{3.12}$$

we see that the maximum achievable temperature with this heat leak is 17 mK - adequate to perform our experiment. The RuO_2 resistors and coaxial cables were reconnected, and the TO cell fill line soldered back into place. Additional heatsinking

was added to the TO fill line at the still plate and cold plate by wrapping copper wire around the line and clamping it to the plate under a copper bolt. The next run showed no loss of cooling with the cables and fill lines reattached, and after fine-tuning the mash and recalibrating the MCT a base temperature of 19mK is readily achieved.

Chapter 4

Software

"That's really the essence of programming. By the time you've sorted out a complicated idea into little steps that even a stupid machine can deal with, you've learned something about it yourself."

Douglas Adams

Dirk Gently's Holistic Detective Agency

4.1 Operating the Torsional Oscillator

We desire to know how the frequency of a resonant mode of the torsional oscillator changes as we vary its temperature. The instrumentation used to drive the oscillator and measure its response is set up as described in section 2.4 and shown in Fig. 2.12. The control computer runs a LabVIEW program that follows the resonance while

sweeping the temperature, discussed in section 4.4. The program detects changes in the resonant frequency from the changes in the in-phase and quadrature response of the oscillator and changes the drive frequency accordingly so that the oscillator is always 'tuned' on to resonance. The algorithm used to calculate the frequency deviation requires knowledge of the parameters of the resonance mode - the resonant frequency F_0, the quality factor Q, the on-resonance amplitude R_0 and the phase shift of the response of the oscillator compared to the drive, φ. These parameters are obtained by one of two methods - either measuring the frequency spectrum of the resonance, discussed in section 4.2, or its free decay in the time domain, or 'ringdown', discussed in section 4.3.

4.2 Frequency Domain Sweeping

By measuring the in-phase and quadrature response of the oscillator at a range of frequencies the frequency spectrum of a resonant mode may be acquired. The resonant frequency F_0, the peak amplitude R_0 and the quality-factor Q of the mode may then be found by fitting a Lorentzian curve to this frequency spectrum. As discussed in section 2.2 a resonant mode approaches a Lorentzian peak in the limit of low damping.

A LabVIEW vi controls the DS345 function generator and reads back the in-phase and quadrature response from the SR830 lock-in amplifier, as described in

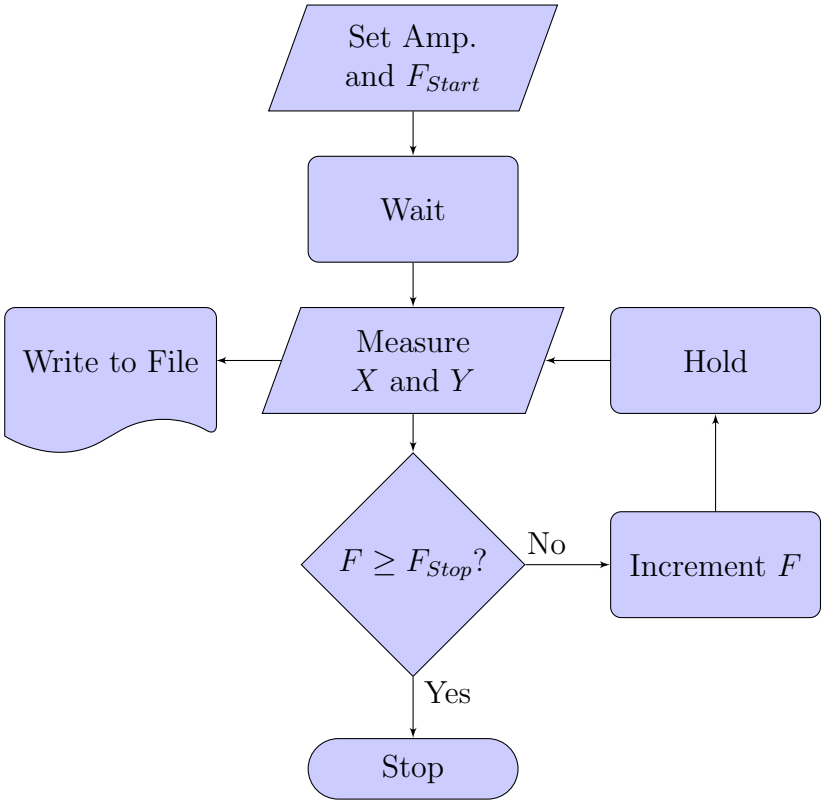

Figure 4.1: Operation schematic of the Frequency Sweeper LabVIEW vi.

section 2.4. The program's operation is shown schematically in Fig. 4.1. The user inputs a drive amplitude, the range of frequencies to sweep though, a starting wait time, the frequency step size, a holding time, sampling time and sampling rate. The vi sets the drive amplitude and starting frequency on the DS345 then waits the specified time to let the signal stabilise as transient components ring down. The wait time is based on the estimated Q of the resonance, typically tens of minutes. Once the wait time has passed the vi starts the SR830 writing X and Y values to its buffer at the sampling rate. Once the sampling time has passed it reads back the buffer and takes a mean of each channel. These mean values are written to a logfile

and displayed. The vi then increments the drive frequency by the required step and waits for the hold time for transients to decay. As the frequency increment is small compared to the linewidth of the resonance the hold time need not be as long as the wait time and is typically tens of seconds. After the hold time another measurement is made. This cycle is repeated until the drive frequency is equal to or greater than the specified stop frequency. The swept frequency range, drive amplitude, hold time, wait time and frequency step are entered as commands in a text field on the left side of the vi front panel, shown in Fig. 4.2. Multiple sweeps may be queued in this fashion.

The logfile is then imported into Sigmaplot where it is analysed. A three-parameter Lorentzian curve

$$y(x) = \frac{a}{1 + \left(\frac{x-x_0}{b}\right)^2} \tag{4.1}$$

is fitted to $R^2(F)$. From the fit parameters the values in our notation are extracted:

$$F_0 = x_0 \tag{4.2}$$

$$R_0 = \sqrt{a} \tag{4.3}$$

$$Q = \frac{x_0}{2b}. \tag{4.4}$$

We would like to know the phase shift of the signal, but this is not contained in

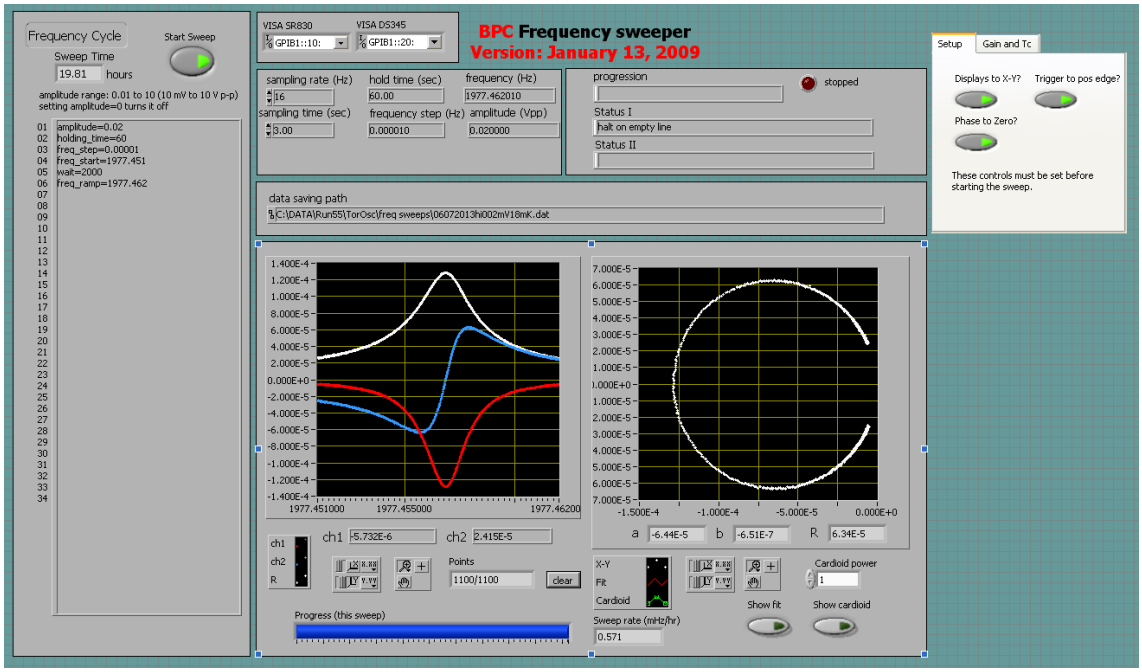

Figure 4.2: The frequency sweeper program front panel. The frequency-domain lineshape is shown in the left plot. The amplitude R is shown in white and the X and Y outputs of the lock-in are shown in red and blue respectively. The right plot shows the same data represented as a complex plot - the X channel is plotted on the horizontal axis against the Y channel on the vertical. The text box on the left is the command-set for the sweep and the tabbed controls on the right are the SR830 settings.

the amplitude information R^2. We can determine the required phase shift by setting the drive to the resonant frequency and varying the lock-in's phase shift until X is at its maximum and Y is minimised, but this is unreliable for noisy signals. A better value can be obtained by fitting a circle through the complex plot representation of the resonance.

We plot the the X channel against the Y channel to produce the complex plot, as shown in Fig. 4.3. In such a plot the resonance appears as a circle of radius

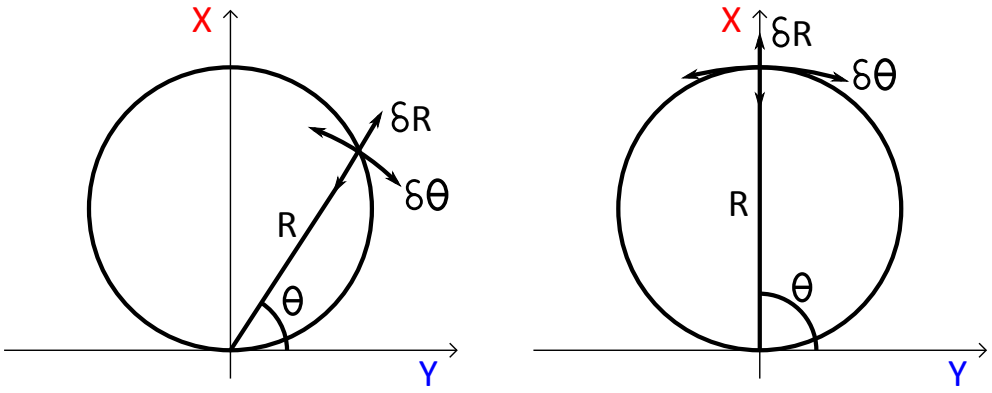

(a) (b)

Figure 4.3: The resonance represented as a complex plot. In (a) the drive is off resonance, and in (b) the drive is at the resonant frequency.

$R_0/2$ centred on $Y = 0$, $X = R_0/2$. Sweeping frequency through the resonance The X and Y channels of the lock-in track around the circle. The total amplitude $R = \sqrt{X^2 + Y^2}$ at a given frequency is then the distance from the origin and the phase θ is its angle about the origin from the Y-axis.

The circle is fitted according to the procedure outlined by Bullock in [21]. This provides the centre coordinates and the radius of the circle. The phase shift of the resonance is then the rotation of the entire resonance circle about the origin. It is necessary to use a two-parameter arctan function to identify the correct quadrant of the phase angle, implemented as:

```
atan2(x,y) = if(x>0)
             atan(abs(y/x))*y/abs(y)
             else
             (180-atan(abs(y/x)))*y/abs(y))
```

The complex plot is a convenient representation as it makes deviations from the Lorentzian response clearly visible. For example if the sweep rate is too fast the resonance will be 'dragged' and the peak will be skewed - this is known as the 'gliding tone' problem. This effect is not immediately obvious from the frequency-domain peak but the circle is clearly distorted, as shown in Fig. 4.4.

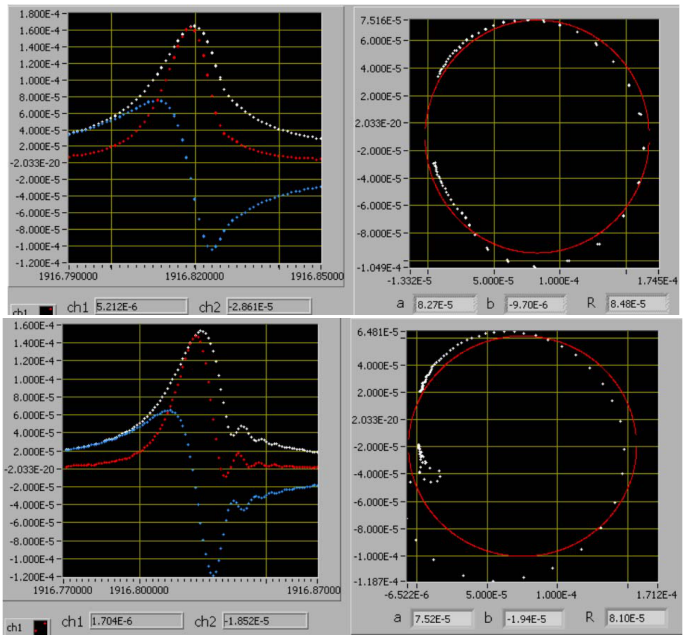

Figure 4.4: Sweeping through the resonance slightly too fast (top) and much too fast (bottom). The distortion of the peak, top left, is slight but clearly visible as a distortion of the circle, top right. Notice that the 'ripples' in the frequency domain, bottom right, appear as loops in the complex plot, bottom right.

4.3 Ringdown

The slow gliding tone required of the frequency sweep at high Q severely limits the rate at which samples can be measured - acquiring a peak may take a full

day, and two must be taken for each temperature sweep. The fourier transform of a Lorentzian peak in the frequency domain is an exponential decay in the time domain, so provided the behaviour of the osillator is linear all the information about a resonance contained in a frequency sweep through a resonance can also be acquired from its free decay. For an oscillator of resonant frequency 400 Hz and $Q = 500000$ a decay will be on the order of $t \approx Q/F \approx 1000\,\mathrm{s}$ – a great improvement.

A LabVIEW vi was written to capture ringdowns. Drive frequency and amplitude are set on the DS345 function generator, then once the resonance amplitude has built to its equilibrium value the drive is removed and the decay is captured by the two-channel lock-in. The DS345 does not output a synchronisation signal when the output amplitude is set to zero, so an in-line relay box was constructed that would break the connection to the torsional oscillator, and is driven from the SR830 Lock-in amplifier auxiliary output. The program may use the buffer of the SR830 to capture low-Q ringdowns at up to 32 Hz, or return data to the computer as the ringdown progresses. The second mode allows the user to see the amplitude decay, but the GPIB connection to the instrument limits acquisition to around 1 Hz so it is not suitable for low-Q resonances which would decay too rapidly. An exponential $y = e^{-t/\tau}$ curve is fitted to the amplitude data R and the Q of the resonance is obtained from the decay constant $\tau = 1/Q$. The natural logarithm of R is also plotted and the result of the exponential fit overlayed. Although fitting to $\ln R$ would be

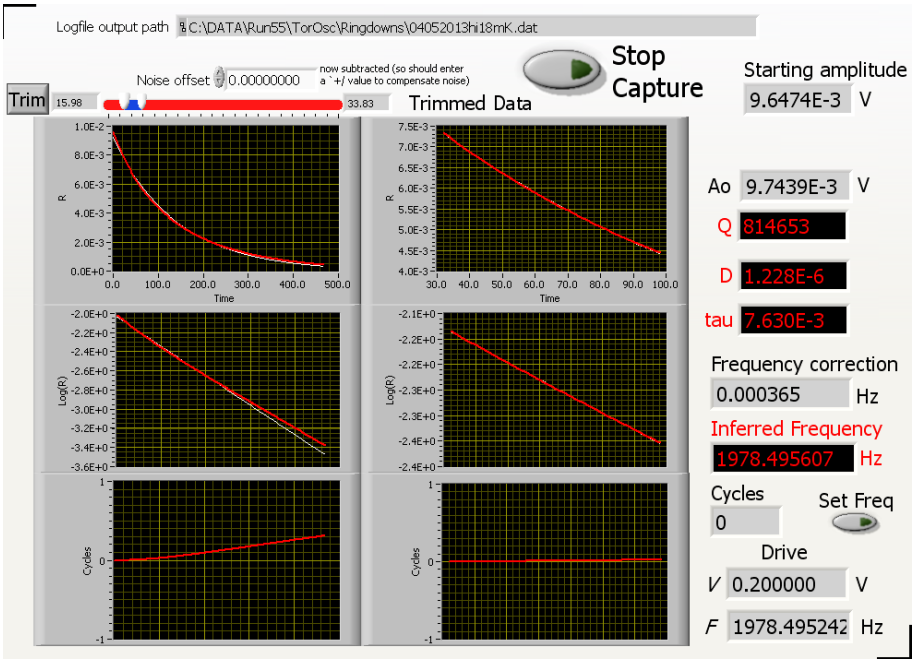

Figure 4.5: A captured ringdown. Note the deviation from an exponential in the untrimmed (left) plots.

less computationally demanding it would be thrown off when the signal decays into noise toward the end of a full ringdown. The frequency correction, or 'off-tuneness', is obtained from the phase progression during the ringdown. This is illustrated in Fig. 4.3 for an oscillator ringing down far from resonance (a) and near resonance (b). The more rapid oscillation of X and Y shows a rapidly advancing phase angle. A capture is shown in Fig. 4.7 is shown for comparison. The phase angle θ is given by the arctangent of X/Y, here implemented as

$$\theta = \frac{Y}{|Y|} \arctan \left| \frac{X}{Y} \right|. \tag{4.5}$$

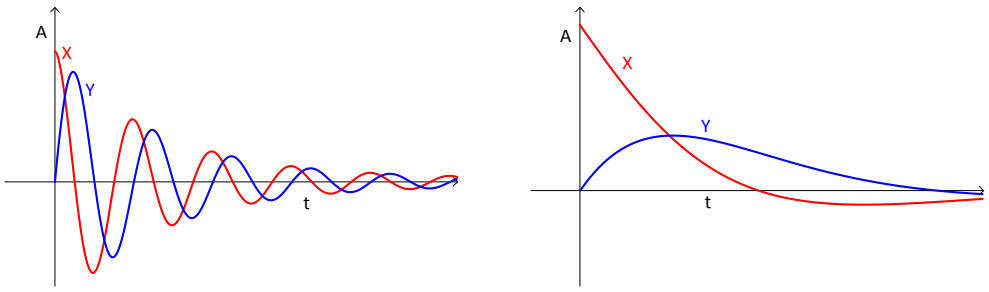

(a) (b)

Figure 4.6: The symmetric and antisymmetric signals during ringdown from well off resonance (a) and near resonance (b) showing the phase progression. A ringdown from exactly on resonance would have zero Y component and be entirely exponential in X.

This value wraps at $\pm\pi$, so to produce a continuously changing variable the difference between subsequent points is found and 2π added or subtracted accordingly when a wrap occurs. The phase angle progression is then fitted with a straight line, whose gradient gives the frequency correction. This correction is added to the drive frequency to obtain the resonant frequency. Strictly this is the damped resonant frequency β, but in practice the Q is sufficiently high that $\gamma \ll \omega_0$ and so $\beta \to \omega_0$. For ease of viewing the display is scaled by 2π so as to count cycles, rather than radians. The necessary phase shift can be found from the intercept of this fit through the phase progression.

Knowing the resonant frequency and the Q the on-resonance amplitude is then found from the amplitude at the start of the capture by a rearrangement of Eq. 2.52:

$$R_0 = R\sqrt{1 + 4Q^2(\omega_d - \omega_0)/\omega_d^2}. \tag{4.6}$$

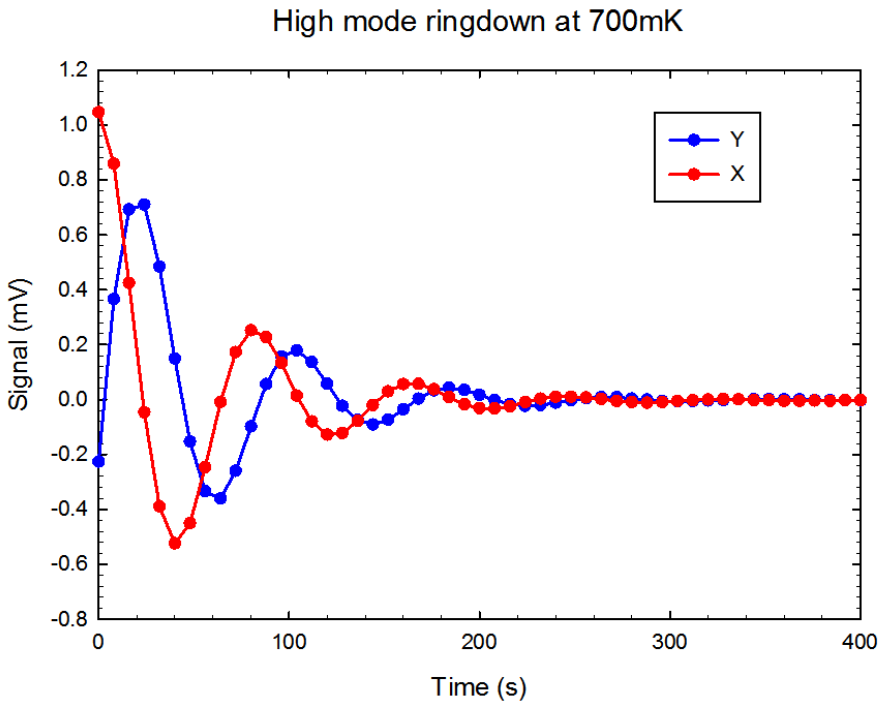

Figure 4.7: A capture of the oscillator's ringdown from some way off the antisymmetric resonance.

The analysis routine is run on the entire capture, but this may be misleading. For example the oscillator may be significantly anharmonic at high drives, may be dominated by noise at long times, or may be distorted at early times by the time constant of the SR830. Any of these will result in non-exponential behaviour as seen in Fig. 4.5 and thus a poor fit. In such cases the user may select a 'Trim' section of the data to fit. Since the oscillator is held on resonance when temperature sweeping we are only interested in the behaviour at high amplitude and thus we trim the data to only analyse early times.

There is also the facility to show the gradient of the natural logarithm of ampli-

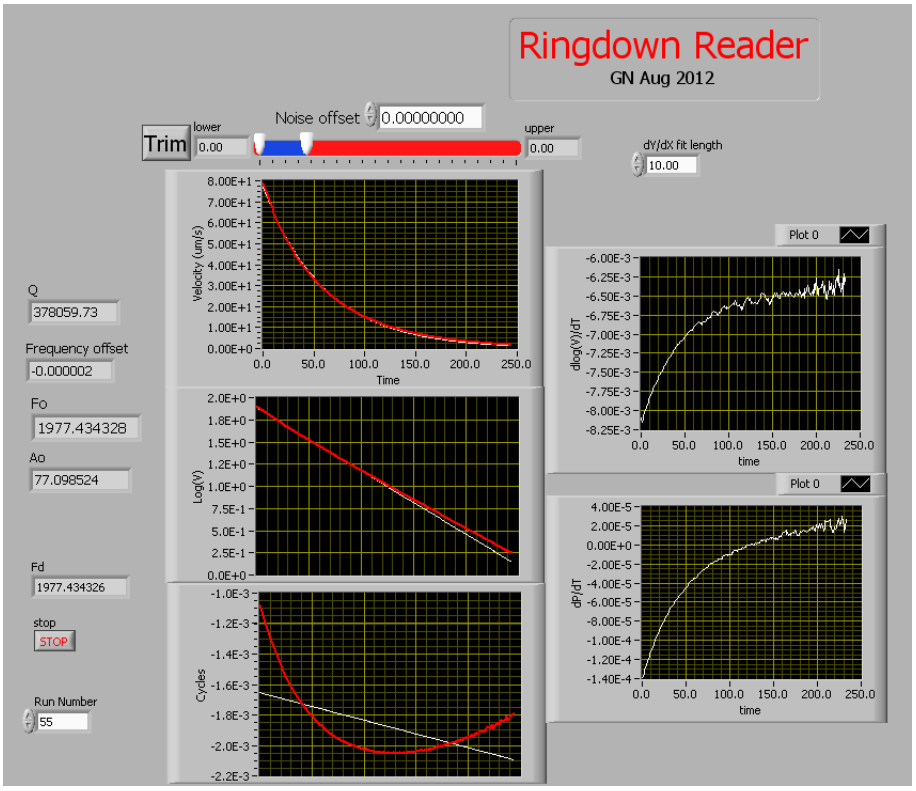

Figure 4.8: A captured ringdown shown in red in the left hand plots. The slopes of $\ln(R)$ and the phase progression are shown in white in the right hand plots.

tude and the phase progression as a function of time. If the behaviour is entirely exponential these should be linear until the signal decays into the noise, but deviations are observed. As the data is digital and noisy it cannot be simply differentiated. Instead the program applies a linear best fit through a shifting window of the data. The user specifies a fitting window width over which a straight line is fitted to the data. The window is then incremented one row in the data array and the fit is repeated. By plotting the gradients of the straight line fits the slope of the data is shown, as in Fig. 4.8. The window size must be chosen to be as short as possible

but longer than noise features, as any features smaller than the window size will be smeared out.

4.4 Tracking the Resonance

A final LabVIEW vi tracks changes in the resonant frequency as the temperature is varied and retunes the drive to hold the oscillator on resonance. The vi controls the driving frequency from the DS345 and reads back the X and Y values from the SR830, as shown schematically in Fig. 4.9. The DS345 is set to drive the oscillator at its resonant frequency and the SR830 phase is set such that X is at its maximum and $Y = 0$. The quality factor Q_{meas} and amplitude R_0 found from either frequency sweep or ringdown are entered in to the program. It reads from the SR830 in the same manner as the frequency sweeper above, averaging *sample time* $\times$*sample rate* points for the X and Y channels. The inferred Q_{inf} is then calculated based on the scaling of the signal amplitude from the input value R_0:

$$Q_{inf} = \frac{(X^2 + Y^2)Q_{meas}}{R_0 X}. \tag{4.7}$$

From our definition of Q in Eq. 2.53 we know that the Q of a resonant mode is directly proportional to its amplitude R – if the Q is higher than when the ringdown or sweep was taken then the amplitude will be proportionally higher as the oscillator

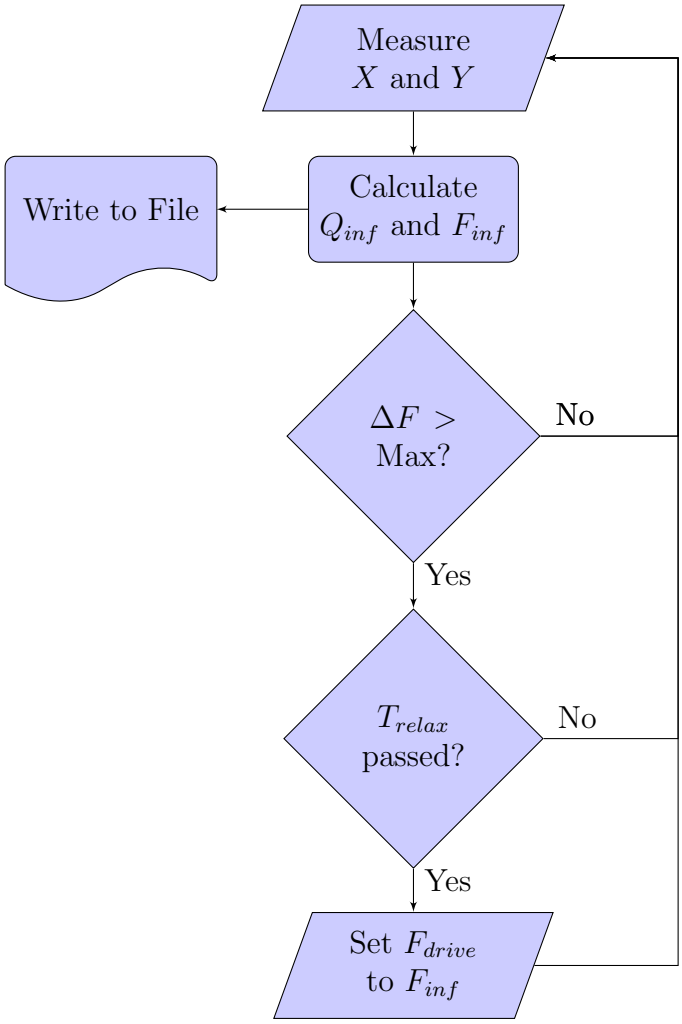

Figure 4.9: Operation schematic of the Temperature Sweeper LabVIEW vi.

is losing less energy, and if it is lower the amplitude will be lower.

The inferred frequency, F_{inf} is calculated from the phase information of the signal. On resonance the Y channel will be zero. We can see from Eq. 2.83 that for small deviations from resonance the Y voltage varies linearly with frequency. As the Q describes the linewidth it will scale the gradient of $Y(\omega)$. From this and the

ω_d set on the DS345 we may infer the resonant frequency:

$$F_{inf} = F_{drive}\left(1 + \frac{Y}{X}\frac{1}{2Q_{inf}}\right). \tag{4.8}$$

The assumption of this linearity is only valid for small frequency deviations, so a maximum permitted deviation is specified in the program. If this deviation is exceeded the drive will be set to the inferred resonant frequency. Since the oscillator takes time to respond to drive changes because of its high Q and F_{inf} depends on the drive frequency the step change in F_{drive} will result in a step change in F_{inf}. Over several τ the transient components will die away and F_{inf} will relax to its true value. To prevent the software setting a new F_{drive} based on a false F_{inf} and thereby driving the oscillator off resonance a relaxation time is set. F_{drive} will only be set if the allowed deviation is exceeded and the relaxation time has elapsed since the last change in F_{drive}.

4.5 Simulation

The oscillator was modelled and its resonant modes simulated in SolidWorks CAD package. 3D drawings of the various parts of the oscillator were created from the machining drawings. The parts were joined into a rigid assembly and material properties were added. The model can be used to quickly determine the moment of

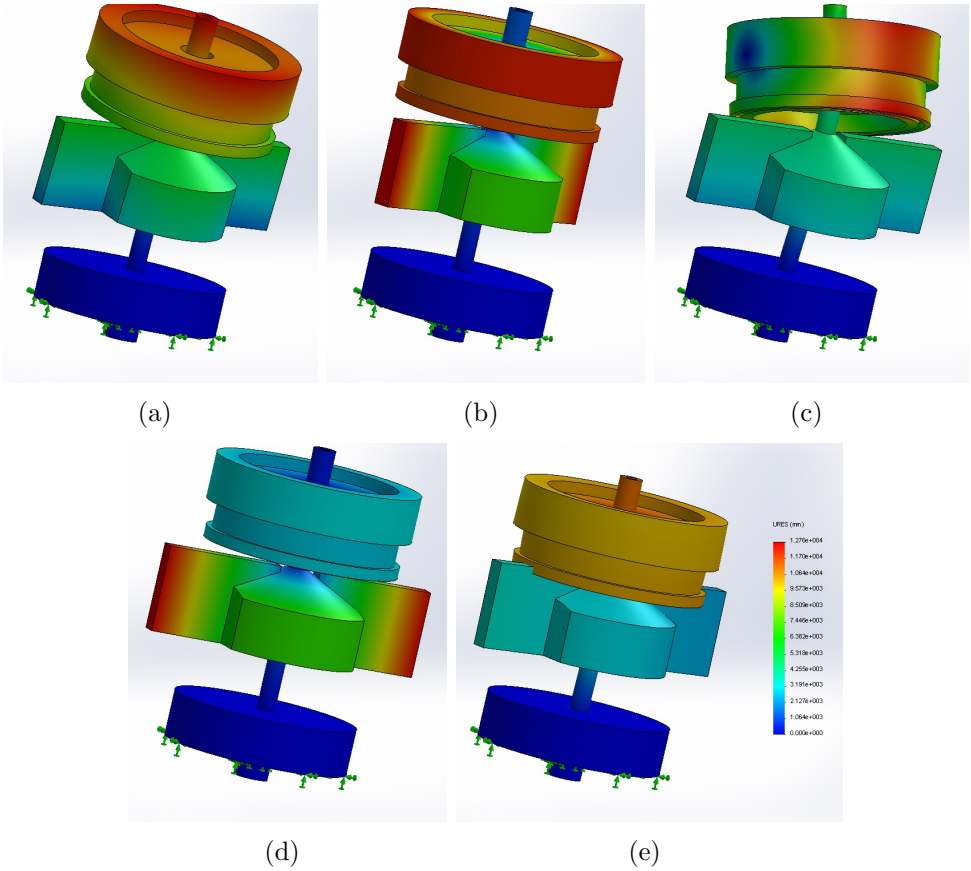

Figure 4.10: CAD software simulation of some of the resonant modes of the oscillator. In order of increasing frequency, a low frequency floppy mode (a), the symmetric torsion mode (b), a high frequency floppy mode (c), the antisymmetric torsion mode (d), and a very high frequency stretching mode (e). Displacement from the stationary position is shown as a colour gradient from blue to red.

inertia of various parts of the oscillator, as used in section 2.5. The model is anchored by the base, shown by green arrows. The software then divides the assembled model into a mesh and simulates the possible movements of the mesh within a specified range of frequencies and identifies resonant modes. The frequencies of these modes and animations of their motion are then displayed for review. The displacement of the oscillator at a selection of resonant modes are shown in Fig. 4.10.

As well as the symmetric (b) and antisymmetric (d) torsion modes, several other resonances are predicted by the software. These are dubbed 'floppy modes', (a) and (c), as the oscillator bends back and forth in its torsion rods, and 'stretching modes', (e), as the torsion rods are stretched and compressed up and down like springs. These modes are visible on a wide-rage frequency sweep of the oscillator, but as they are of low Q and move the sample in a more a complicated fashion they are not used.

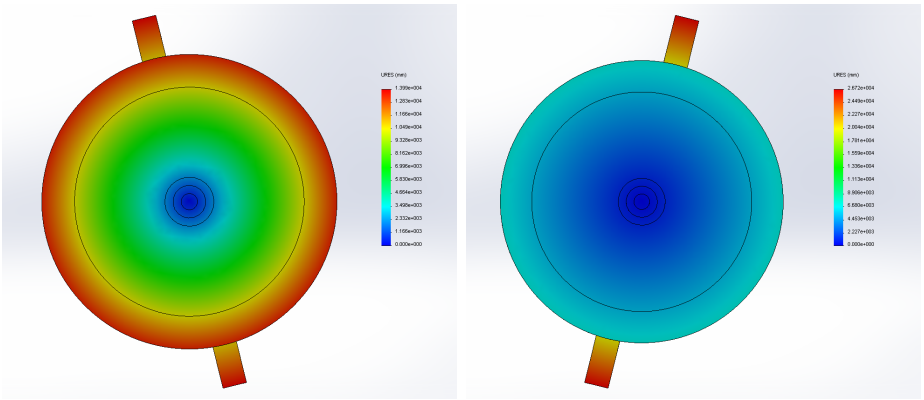

(a) (b)

Figure 4.11: Plan view of the two torsion modes. (a) shows the symmetric, low frequency mode and (b) shows the antisymmetric, high frequency mode.

We can see the relative displacement of the high and low torsion modes from a plan view of the simulations of the symmetric and antisymmetric torsion modes, (b) and (d) respectively in Fig. 4.10. Viewed as an animation or as a vector field they show the symmetric and antisymmetric motion of the low and high frequency torsion modes respectively. From these simulations we can read off relative displacements

of

$$\left.\frac{X_2}{X_1}\right|_s = 1.4 \quad \text{and} \quad \left.\frac{X_2}{X_1}\right|_a = -0.2 \tag{4.9}$$

for the two modes which compare well with our calculated ratio of displacements from Eqn. 2.68

$$\left.\frac{X_2}{X_1}\right|_s = 1.368 \quad \text{and} \quad \left.\frac{X_2}{X_1}\right|_a = -0.178. \tag{4.10}$$

The predicted resonant frequencies of low frequency modes are reasonably close to the measured values, but accuracy is poor at high frequencies. This may be because of small variations in the machining (particularly in the torsion rods where k varies as the fourth power of diameter), an inadequately fine meshing of the 3D model or incorrect material properties. Due to the poor quantitative agreement it was decided not to use the model to estimate the change of the torsion mode frequencies under changes in the behaviour of the sample, but it has value as an illustrative tool to explore the motion of the oscillator.

Chapter 5

Results

In God we trust. All others must bring data.

W. Edwards Deming

5.1 Growing the Sample

The torsional oscillator cell and its fill line must be tested for leaks at room temperature and at nitrogen temperature. The cell is loaded using the gas handling system (GHS) shown in Fig. 5.1. The system is pumped out and flushed with nitrogen to clean it, then the dump barrel may be filled from either the ^{3}He sample cylinder or with ^{4}He through the pumping port. To generate pressure in the cell the dump is opened to an activated charcoal dipping bomb immersed in liquid helium. The large surface area of the charcoal strongly adsorbs helium gas when it is cooled to

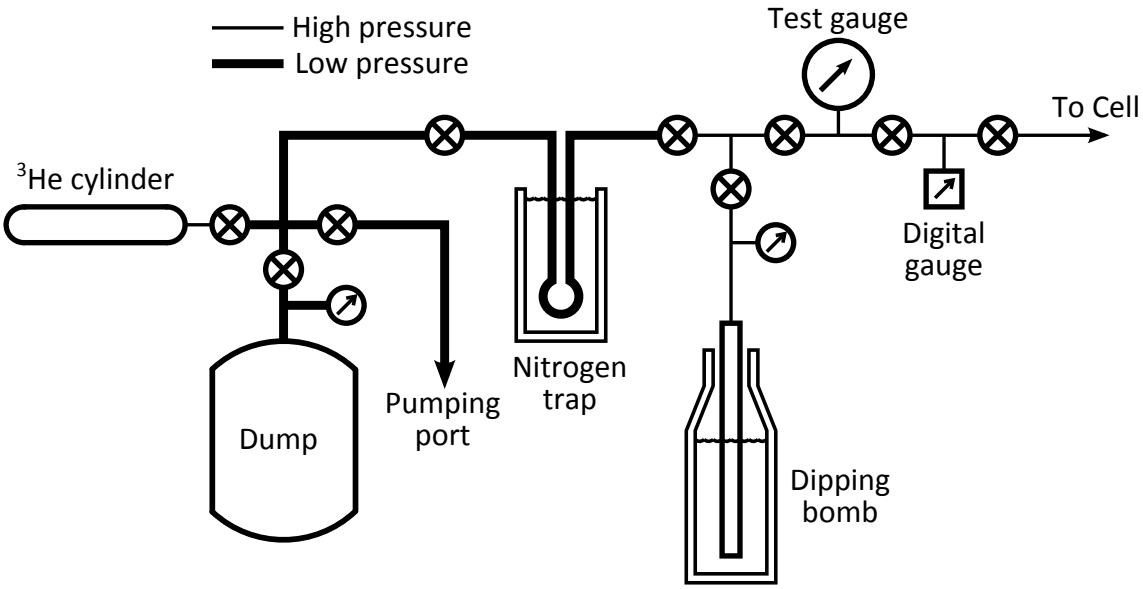

Figure 5.1: The sample gas handling system.

4.2 K. As the sample gas is cryopumped in to the dipping bomb it passes through a charcoal nitrogen trap. This is immersed in liquid nitrogen so that any air or other contaminant that may have entered the system is bound to the charcoal, but helium will pass through freely. The dipping bomb is left to charge for several hours then closed off to the low-pressure side of the GHS.

The bomb is then raised out of the liquid and the the sample gas desorbs from the charcoal as it warms, raising the pressure. The pressure may be controlled with some precision by careful raising and lowering or the bomb. The bomb is cleaned by lifting it in and out of the liquid several times before opening it to the cell so that any impurities are trapped in the bottom of the bomb. This part will not be raised out of the liquid and so any impurities will not desorb as the sample gas pressure is

increased. The bomb is then opened to the cell and the pressure is raised to a few bar at room temperature while a leak detector pumps on the vacuum can. The cell pressure gauge is monitored to check the performance of the back-diode oscillator and to ensure the fill line has not become blocked. This is then repeated once the cryostat has been cooled to liquid nitrogen temperature as leaks may have opened under thermal contraction. If all these tests are satisfactory the cryostat is cooled to helium temperature.

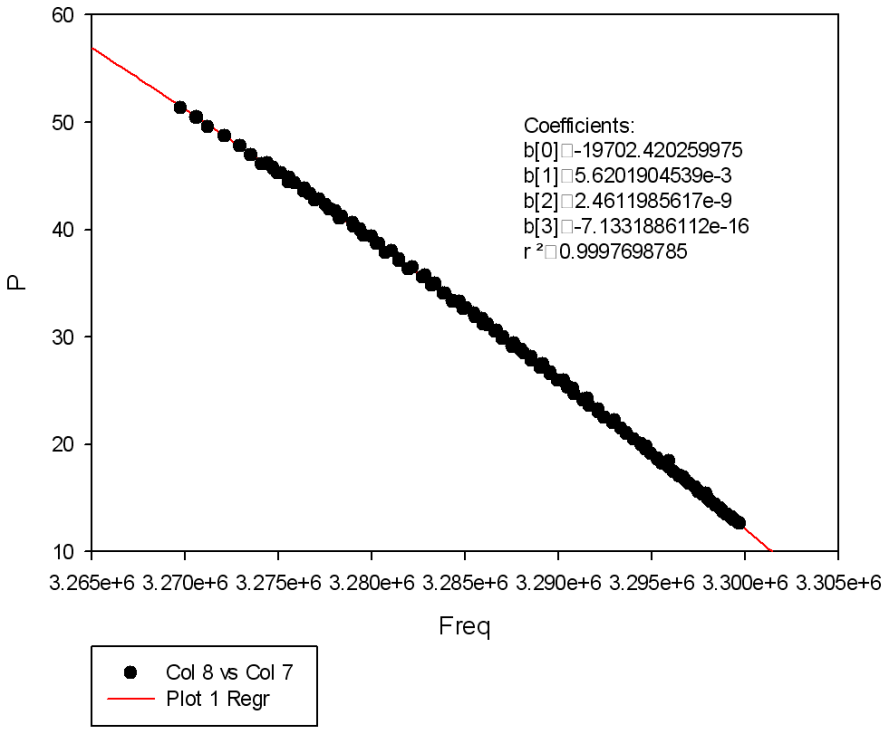

Figure 5.2: Calibrating the cell pressure gauge against the Paroscientific gauge. This plot includes points taken both on increasing and on decreasing the pressure and is fitted with a third order polynomial.

On reaching helium temperature the cell pressure gauge is calibrated. The bomb

is loaded and cleaned and then opened to the cell. The cell is then exercised by raising it to a little over the desired sample growth pressure and then gently reliving the pressure three times to prevent hysteresis in the deflection of the pressure gauge. The cell pressure is then raised and lowered over the working pressure range for the run, stopping at intervals to let the pressures stabilise. A LabVIEW vi captures the back diode oscillator frequency and the pressure given by a Paroscientific Digiquartz gauge to produce a calibration curve. By comparing the points taken on increasing the pressure and those taken on decreasing it we can confirm that the lag between the gauge and the cell is small. The calibration is fitted with a polynomial as shown in Fig. 5.2 and the fit parameters loaded into a LabVIEW vi that monitors the cell pressure.

In this experiment both ^{3}He and ^{4}He samples were used. These isotopes have very different phase diagrams, as shown in Fig. 1.1. In ^{3}He the sample is solidified at a little over 1 K, whereas in ^{4}He the melting line is above 2 K. As such, low pressure ^{3}He crystals are grown with the pot running and the cell at 1.5 K and ^{4}He crystals are grown with the pot stopped and the cell at 4.2 K.

Once the cell has been calibrated it is loaded to the required growth pressure. The solid density of the sample at the required pressure is taken from the literature. The cell is then loaded to the pressure corresponding to that density at the melting line. In ^{3}He the starting pressure will also determine the structural phase of the

final sample – body centered cubic (BCC) at low pressure or hexagonally close packed (HCP) at high pressure. In ^{4}He the BCC phase is limited to a narrow region between 1.4 K and 1.8 K, and 26 bar and 30 bar, and only HCP remains at our working temperature. The *in situ* pressure gauge allows us to confirm the final sample pressure for precise positioning on the $P-T$ phase diagram. This growth method is known as 'blocked capillary', or constant volume growth, where a solid is formed behind a block in the fill line. This is known to produce highly disordered polycrystaline samples as pressure changes behind the block break up the crystal lattice [30]. This growth technique produces the largest period shifts observed in other groups [81].

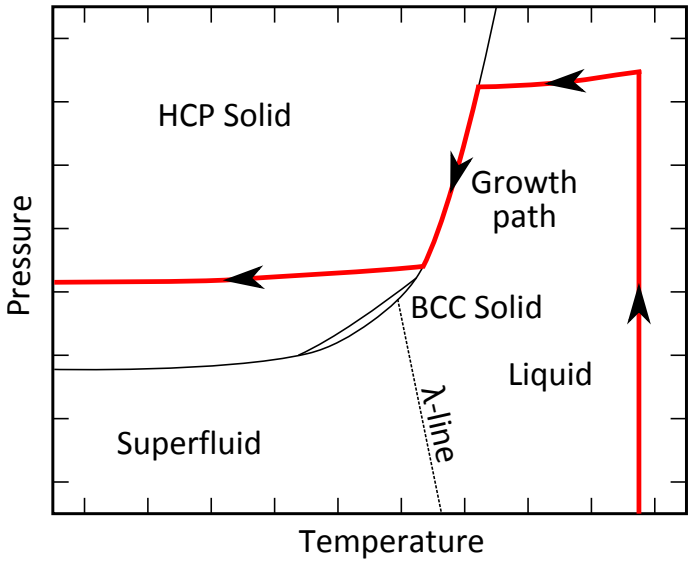

Figure 5.3: Typical blocked capillary growth of a ^{4}He sample. The cell is loaded with liquid. It contracts slightly on cooling and joins the melting line and the sample starts to freeze. Because of the difference in density between the solid and liquid phases the mixture follows the melting line until all the liquid is frozen. The solidified sample then leaves the melting line and contracts slightly as it cools.

Once the dipping bomb is stabilised at the growth pressure the pot is started. The pot plate quickly cools to 1.4 K and the liquid in the fill line freezes to form a solid plug where the line is thermally anchored to the pot plate. The growth of the sample follows an isochor on the $P-T$ phase diagram. A typical growth path in ^{4}He is shown in red in Fig. 5.3. The digital gauge at room temperature and the cell gauge will now move independently, so the user can confirm that the line is blocked. At this point the cell fill line is closed off to the GHS and the bomb is emptied back to the barrel. It is critical that the bomb and nitrogen trap are pumped out as they are warmed to room temperature as any air that may have leaked into the GHS will expand on warming and could reach dangerous pressures.

The ^{3}He/^{4}He mash is admitted into the cryostat as the pot cools the cryostat overnight. Once the cryostat is equilibrated at $\sim$1.5 K the MCT is loaded in the same fashion from its own gas handling system. The MCT fill line is plugged at the still plate by starting the condensed mash circulating through the dilution unit.

5.2 Empty-Cell Backgrounds

On the initial cooldown the torsional oscillator cell is not loaded. The empty torsional oscillator has temperature dependant behaviour that must be subtracted away from the data to leave only the behaviour of the sample. This behaviour is drive dependent, so several backgrounds must be taken for each of the two torsion modes.

Below a certain drive level the drive dependence diminishes and the backgrounds all follow the same curve, as shown in Fig. 5.4 and Fig. 5.5. The temperature of the cryostat is stabilised at 700 mK and the oscillator drive amplitude is set. A frequency sweep or ringdown is performed to obtain the parameters of the resonance to be studied. The temperature sweep vi is then started with these parameters to hold the oscillator on tune and the temperature of the cryostat is swept down to base temperature linearly over 12 hours. This sweep rate is slow enough that the sample remains thermalised with the thermometers. In this way the temperature dependence of the resonant frequency and Q is obtained between 700 mK and 18 mK.

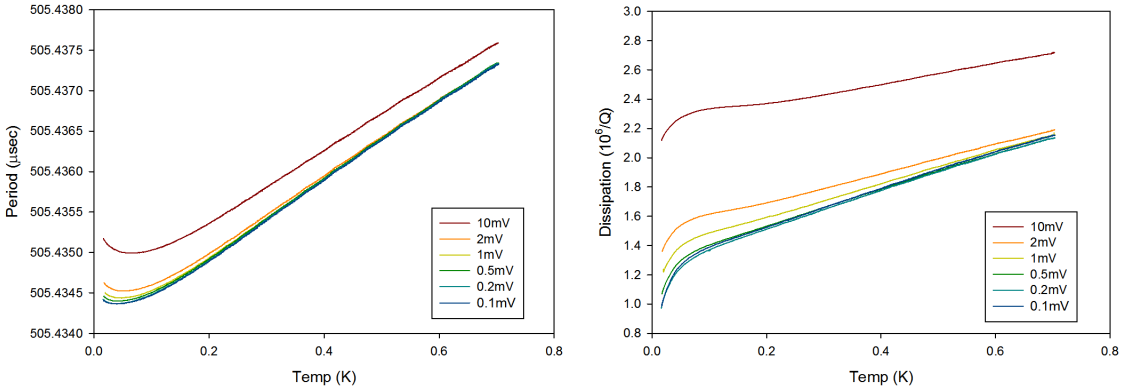

Figure 5.4: High mode empty-cell period and dissipation.

The low mode shows larger deviations in its frequency and amplitude, most likely because its frequency is close to that of some source of mechanical noise in the lab, such as a pump. Where possible the sweeps are run overnight to minimise ambient noise. The temperature sweeps are fitted with a high order polynomial so that the empty cell behaviour may be subtracted away from the Q and frequency points

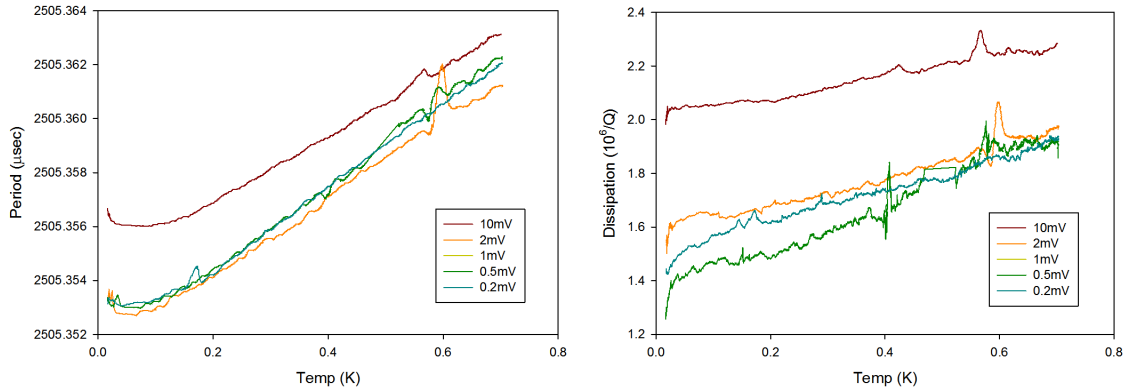

Figure 5.5: Low mode empty-cell period and dissipation.

obtained with a sample in the cell. In the context of the sample it is more convenient to discuss in terms of resonant period P and dissipation D, so the reciprocals of the F and Q are taken to produce the plots in Fig. 5.4 and Fig. 5.5.

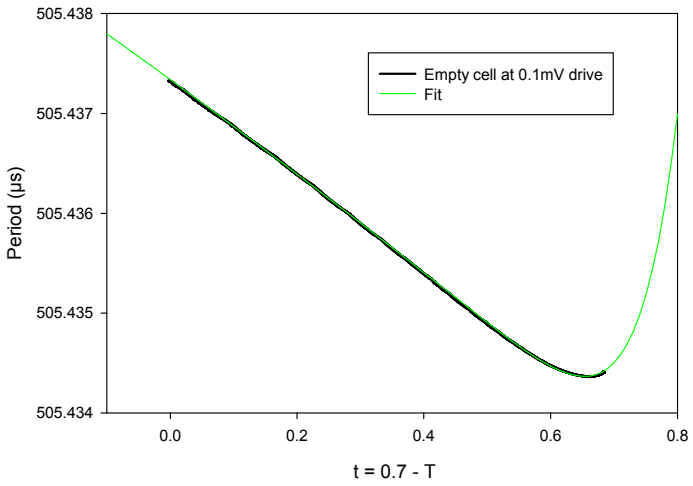

Figure 5.6: Fitting the empty cell background as $P = a + bt + ct^2 + dt^{13}$ where $t = 0.7 - T$. The data is black, the fit is overlayed in green.

The polynomial gives a better fit if the temperature scale is reversed, *i.e.* we fit to $t = 0.7 - T$ rather than T. Originally a 10^{th} order polynomial was used.

The period and dissipation variation with temperature is essentially linear down to 100 mK where a sharp turn occurs. This marks the onset of 'glassy' behaviour of the metal due to tunnelling systems within the metal, namely the movement atoms in double-well potentials around defects [73, 89].

This means that most of the high order terms are very small, and only the highest were needed to account for the sharp turn. It was found that a better fit was achieved using a quadratic with an added t^{13} term, *i.e.*

$$P = a + bt + ct^2 + dt^{13}. \tag{5.1}$$

The slightly curved high temperature behaviour is well fitted by the quadratic, and the sharp curve is well fitted by t^{13}. An example of the fitting is shown in Fig 5.6. Neglecting the highest drives the fit parameters a and c change very little between different drive levels, and the parameters b and d vary linearly with drive level. The empty oscillator was left tracking the low mode resonance stabilised at 50 mK as a 'worst case' test, and was found to show 1.9 µV of amplitude noise and 0.95° of phase noise with a frequency stability of 10 µHz.

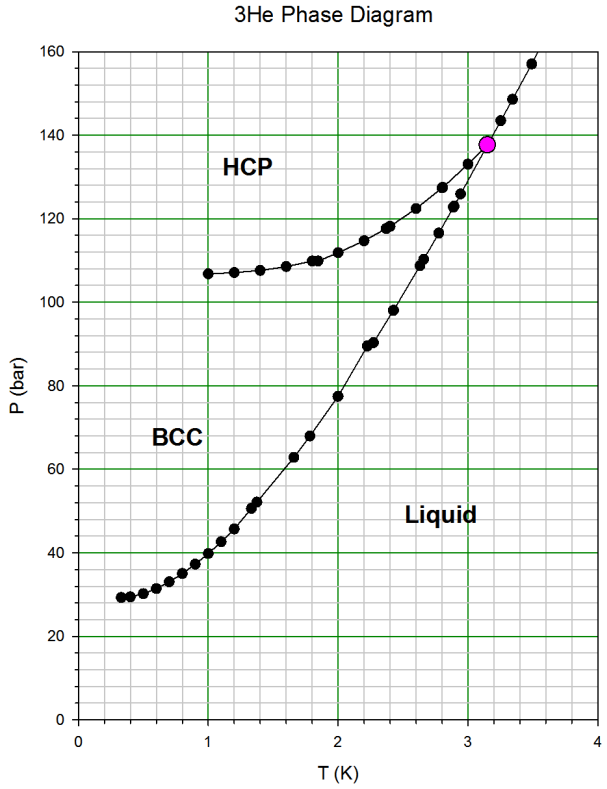

Figure 5.7: The $P-T$ phase diagram of ^{3}He. The tri-critical point at 3.148 K and 137.7 bar is shown in pink. Data taken from Straty and Adams [84], and Grilly and Mills [38]

5.3 The ^{3}He Sample

Once a set of empty background sweeps were acquired the cryostat was warmed to 1.5 K and the cell was filled with ^{3}He. The cell was loaded at 52.0 bar to produce a final solid pressure of 41.5 bar. At this pressure ^{3}He is BCC.

The resonant mode frequencies were found via ringdown and confirmed by frequency sweep at a number of different drive levels. The difference between the empty cell and loaded frequencies at 700 mK is the mass-loading frequency. This

difference may then be used to scale any observed frequency changes as a fraction of the sample mass.

The resonant frequency and Q were then logged as the temperature was swept for each in the same fashion as the empty cell. From the background polynomial empty-cell period P and dissipation D values were generated for each P and D point of the sweep, and subtracted away. In this manner the temperature dependent behaviour of the empty cell is removed from the data.

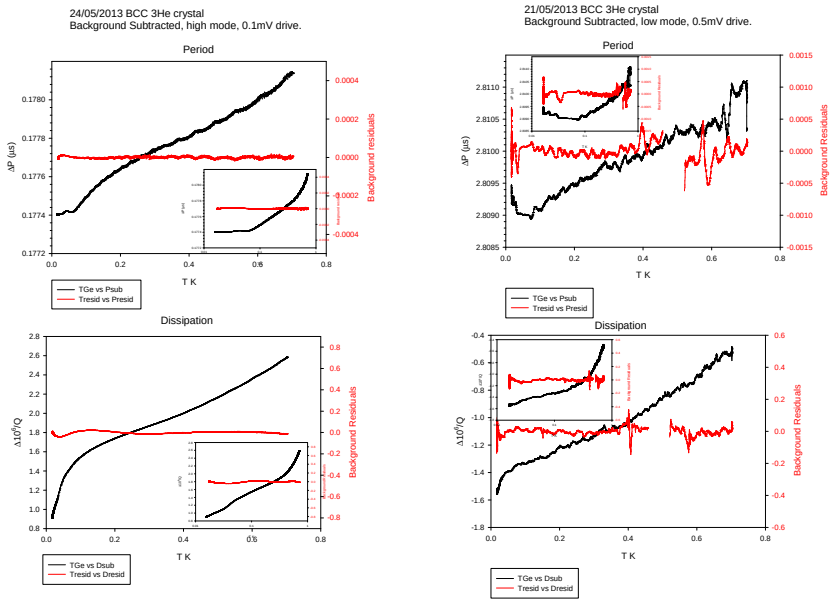

(a) (b)

Figure 5.8: Behaviour of the ^{3}He sample at high frequency (a) and low frequency (b). Empty cell background behaviour has been subtracted. The errors from the background fitting are shown in red. Period shift is shown at the top and dissipation at the bottom.

Examples of temperature sweeps on the ^{3}He sample are shown in Fig. 5.8. The

small feature at very low temperatures may be some loss mechanism in the sample freezing out, causing a drop in dissipation and shifting the resonant period. In agreement with other groups using a ^{3}He control sample we see no feature in the period at 200 mK and no peak in the dissipation. We observe no drive dependence in the ^{3}He temperature sweeps.

5.4 The ^{4}He Sample

The dilution unit and the pot were then stopped and the cryostat was warmed to 5.0 K and the cell was emptied into the bomb. The cell was cryopumped by the bomb for 24 hours then closed off and the sample gas returned to the ^{3}He dump. The cell was then flushed with ^{4}He and left for an hour to dislodge any ^{3}He from the cell walls and fill line. The cell was then pumped out for several hours, and the ^{4}He flush and pump were repeated twice more. The cell was then loaded with ^{4}He to a growth pressure of 80.0 bar and the cryostat was cooled to base temperature, giving a final sample pressure of 42.0 bar.

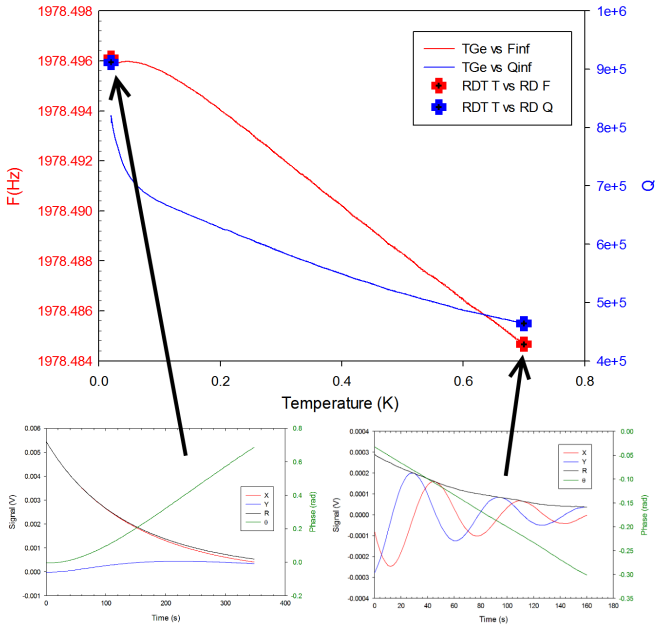

Figure 5.9: The raw f and Q data collected from a twelve hour temperature sweep of the empty oscillator. The smaller plots below show the ringdowns used to collect the initial f and Q parameters used to track the resonance, left, and to remeasure then to confirm that the sweep tracked correctly, right. The small discrepancy at the low temperature (left) end of the sweep is due to the cryostat cooling further after the sweep is completed.

The mass loading frequency shift was found in the same manner as for ^{3}He and the temperature sweeps were conducted, again from 700 mK to base temperature over 12 hours. The background were subtracted to produce a set of data sheets of sample period shift ΔP and dissipation contribution D for several drives at each frequency. Example data sheets are shown in Fig. 5.10 (high mode) and Fig. 5.11 (low mode).

The two plots on the left side are the raw data taken from the temperature sweeping program, the upper plot is the period of the resonant mode and the lower

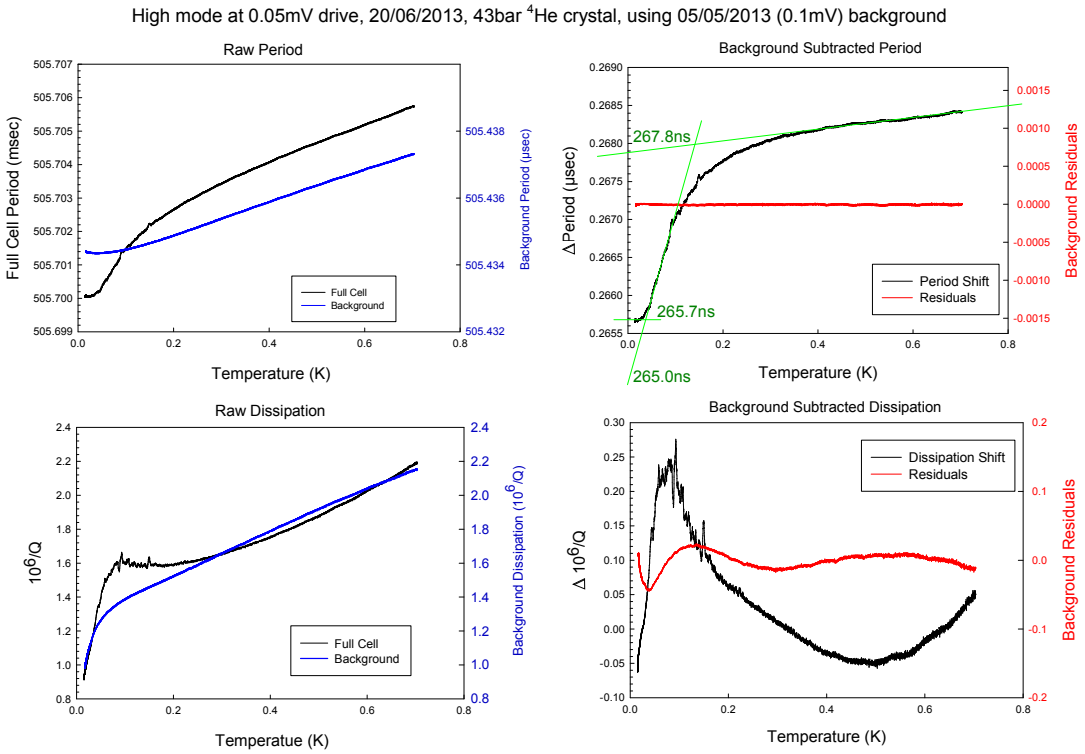

Figure 5.10: A high frequency ^{4}He example data sheet.

is its dissipation. The full cell data is shown in black, and its corresponding empty cell background is shown in blue. The scales are shifted but of the same span so that differences between the loaded and empty cell are obvious. The plots on the right side show the full cell data after the empty cell background data is subtracted away. Again, the upper plot shows the period and the lower plot the dissipation. The data is shown in black, and the error arising from the polynomial fitting of the background in red. The low mode shows more noise due as it couples more strongly to sources of mechanical vibration in and around the cryostat. The noise in the Q

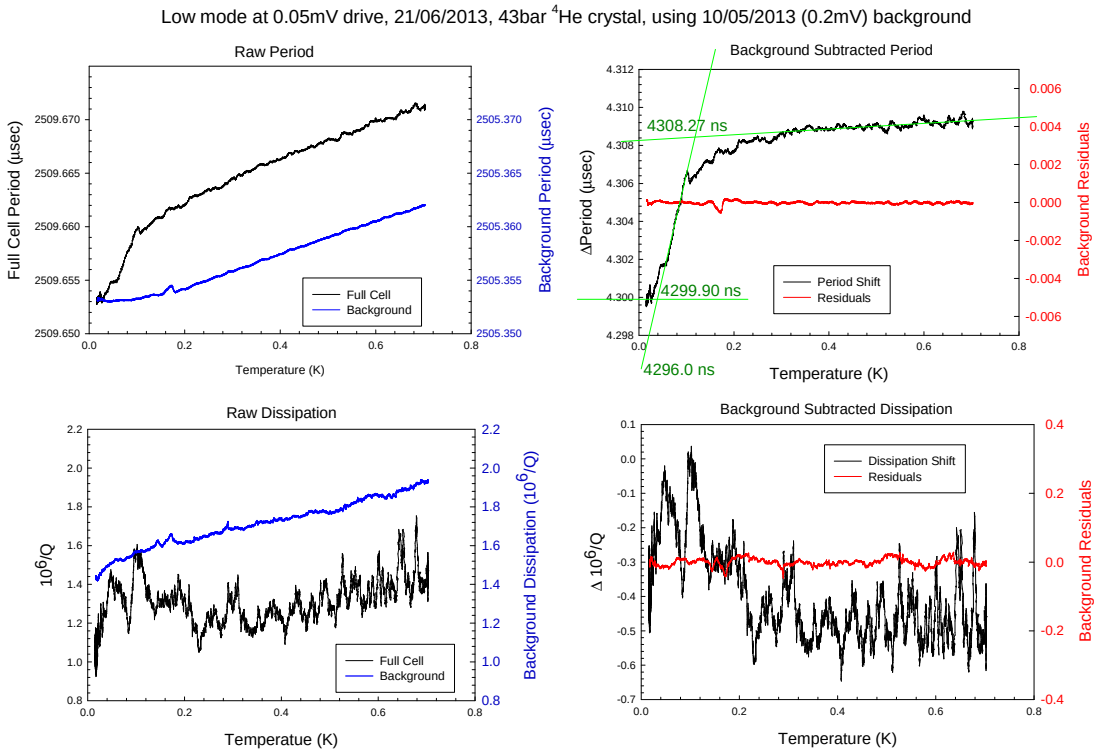

Figure 5.11: A low frequency ^{4}He example data sheet.

is greater as this is calculated from the angle between the two lock-in channels and is thus highly sensitive to phase noise, whereas the period is only sensitive to the amplitude noise.

The general shape of these period shift plots is a plateau at high temperatures, gently sloping down in period on cooling. On approaching 200 mK the downward slope increases, reaching a maximum gradient around 60 mK which coincides with the peak in the dissipation. At around 30 mK the dropping period levels off sharply and remains constant or rises slightly. At higher drives the levelling off at low tem-

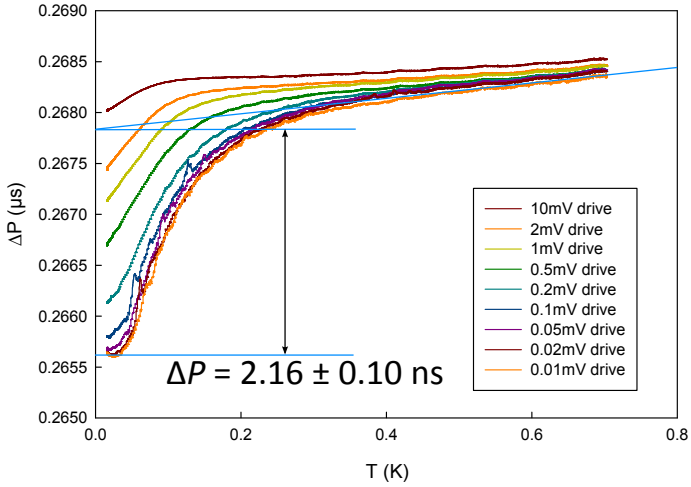

Figure 5.12: High frequency period shift summary.

perature is not observed - presumably it is suppressed below the base temperature of the cryostat.

Over the ΔP plot top right a construction (green lines) is made to find the period shift. First the high temperature slope is extrapolated to $T = 0$. Then the lowest period the oscillator reaches is then subtracted from the extrapolation of the high temperature slope to give a lower limit on the period shift, as shown in blue on the summary plots. The steepest section of the period drop is then extrapolated back to $T = 0$. This intercept is subtracted from the extrapolation of the high temperature slope to give an upper limit on the period shift. For sweeps at low drive level where the levelling off of the period at low temperature is observed only the lower limit shift value is used. At higher drives we can only specify a range between the two limits in which the maximum period shift may be.

Summaries of the sweeps at various drive levels are shown in Fig. 5.12 (high

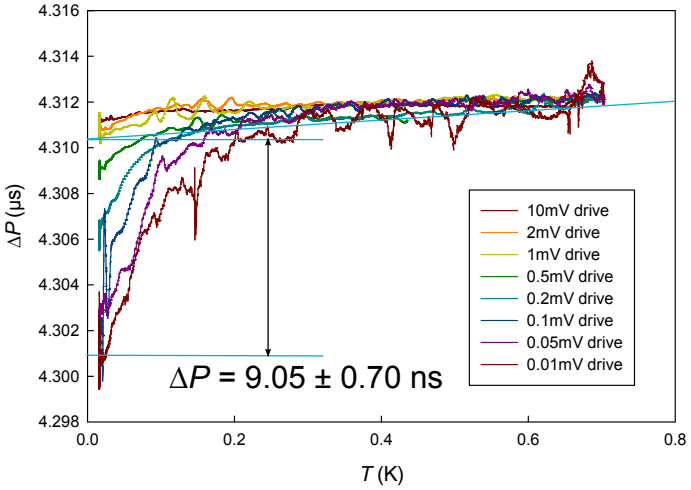

Figure 5.13: Low frequency period shift summary.

mode) and Fig. 5.13 (low mode). The sweeps in the low mode summary are shifted for clarity.

The dissipation of the oscillator is also measured during the temperature sweep as shown in Eqn. 4.7. An empty cell background dissipation is then subtracted via a polynomial fit as for the oscillator period, leaving the bare dissipation of the sample as a function of temperature. The dissipation shifts are summarised in Figs. 5.14 and 5.15 for the high and low frequency modes respectively. The high frequency summary shows a clear peak at low temperatures, growing in amplitude and appearing at higher temperature with decreasing drive. The same feature is present in the low frequency mode but is obscured at lower drives by noise.

The period shift for each mode is then taken as the mean of the measured lower limit shifts at drive levels where the shift is saturated. The period shifts are then divided by the mass loading period for the corresponding mode to scale them by the

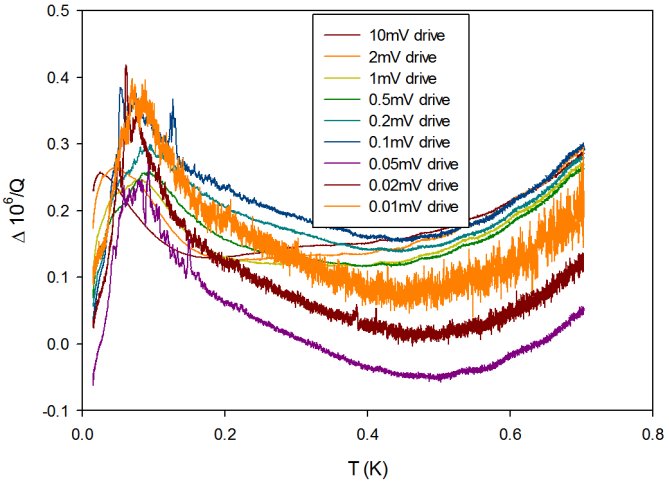

Figure 5.14: High frequency dissipation shift summary.

mass sensitivity of the oscillator at that mode. Note that this mass loading period is not the same as the parameter β derived in Eq. 2.93 – β refers to the frequency change caused by changes of moment of inertia as a fraction of the moment of inertia of the entire head of the cell, whereas this scaling gives shift as a fraction of the helium sample, $\frac{\Delta M}{M_{\mathrm{He}}}$. These values are given in Table 5.1.

Table 5.1: Period shifts and apparent change in moment of inertia of the torsional oscillator.

	ΔP	$\Delta M/M_{\mathrm{He}}$
Symmetric mode	(9.05 ± 0.70) ns	$(2.10 \pm 0.16) \times 10^{-3}$
Antisymmetric mode	(2.16 ± 0.10) ns	$(8.04 \pm 0.37) \times 10^{-3}$

Once the data had been acquired the cell was very gently opened to the dump barrel. The cryostat was warmed up to room temperature and the cell left open to the dump barrel to equilibrate. Because the cell had been used to measure a ^{3}He sample before the ^{4}He sample was loaded there may have been some contamination

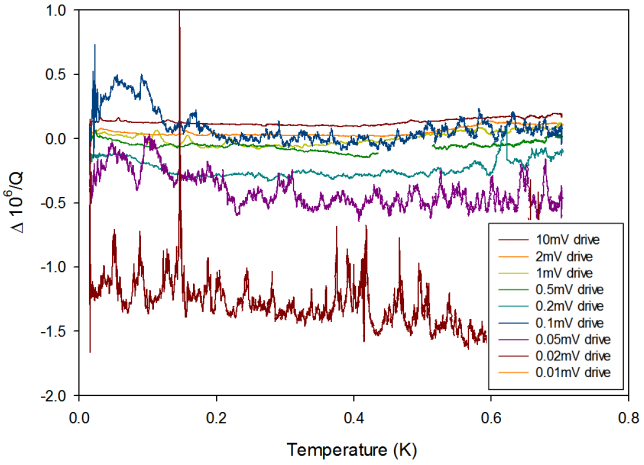

Figure 5.15: Low frequency dissipation shift summary.

from ^{3}He that was not removed by flushing the cell with ^{4}He. To test this a leak detector was used in a similar manner to that discussed in section 3.3 to measure the ^{3}He impurity concentration. In this case the ^{3}He concentration was much smaller, and so the method of measuring ^{3}He and ^{4}He leak rates as in section 3.3 may be inaccurate. The mass peak of the abundant ^{4}He may overlap with the center of the ^{3}He mass peak, inflating the ^{3}He abundance.

By controlling the leak detector from a computer over RS232 it is possible to initiate a service procedure that generates a full mass spectrum from the leak detector. The leak detector sweeps its accelerating voltage from 300 V to 1000 V and gives the mass spectrometer current, scaled as a leak rate, to a two channel chart recorder output. The leak rate is outputted in scientific notation with the mantissa on one channel and the exponent on the other, as analogue voltages between 1 V and 10 V. These two channels are captured by a Textronics TDS430A storage os-

cilloscope and are read back to the control computer via GPIB. A python program provided by Dr Lev Levitin combines the mantissa and the exponent to obtain the mass spectrometer current. From this data Fig. 5.16 was produced.

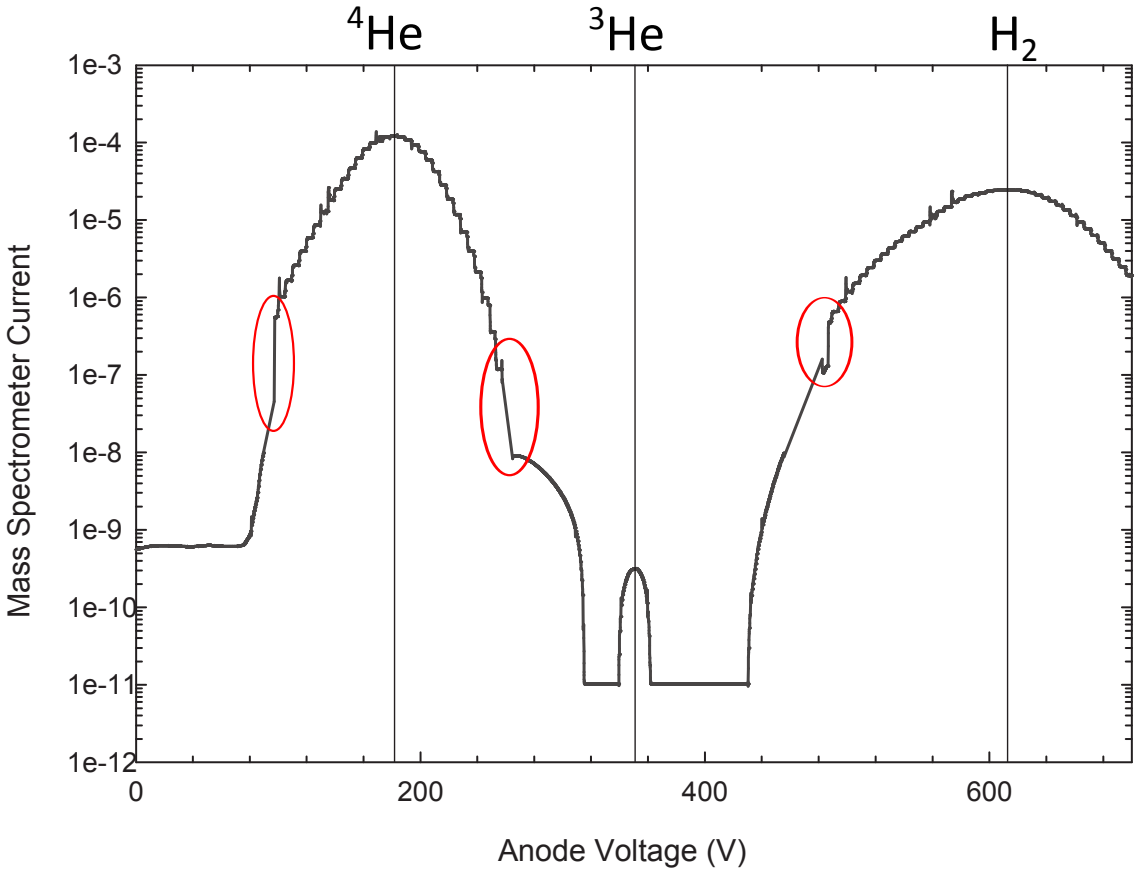

Figure 5.16: Mass spectrometry of the ^{4}He sample. The isotope peaks are labelled along the top edge. The discontinuous features circled in red are artefacts from the leak detector automatically changing its preamplifier gain.

A needle valve was mounted between the leak detector and the sample gas handling system. The valve and piping are pumped out and the needle valve is closed. The sample gas is then admitted behind the needle valve and the leak detector is set to monitor ^{4}He. The needle valve is then cracked open to allow the sample gas to

enter the detector, and opened until the leak rate reaches $1.0 \times 10^{-4}\,\mathrm{mbar\,l\,s^{-1}}$. The mass spectrum is then swept and captured. Three distinct peaks are observed with lighter masses at higher accelerating voltages. As well as the two helium isotopes originating from the sample a large hydrogen peak originates from the breakdown of the pump oil. In previous measurements on samples of known purity Dr Levitin learned that the leak detector is 2.3 ± 0.1 times more sensitive to ^{3}He than to ^{4}He, so this correction factor was applied. Comparing the height of the isotope peaks and applying the correction factor gives a ^{3}He impurity concentration of 1 part-per-million, essentially the same purity as commercial helium gas [95].

Chapter 6

Interpretation

> Torture the data, and it will confess to anything.
>
> *Ronald Coase*

6.1 Drive Dependence

Superfluidity of liquid helium is suppressed above a certain critical velocity, $v_c \approx 20\,\mathrm{cm\,s^{-1}}$ [7]. If the 'supersolid' phase is its analogue one would expect a similar critical flow velocity. Persistent DC flow experiments in solid helium have proven fruitless [36, 18, 27, 83] or highly complex [76, 75], so we must rely on the torsional oscillator. As expected the observed period shifts increase as the drive level (and hence the velocity) is reduced until a saturation is reached where further reductions in drive produce no larger period shift (see section 5.4). However, the nature of the

torsional oscillator introduces complications. Because the cell is undergoing simple harmonic motion we cannot say whether the suppression of period shift at high drives at a given frequency is a response to the sample velocity, the acceleration it is undergoing or the shear it is subjected to.

The two-mode oscillator allows us to resolve this ambiguity by comparing the period shift suppression of the two modes.

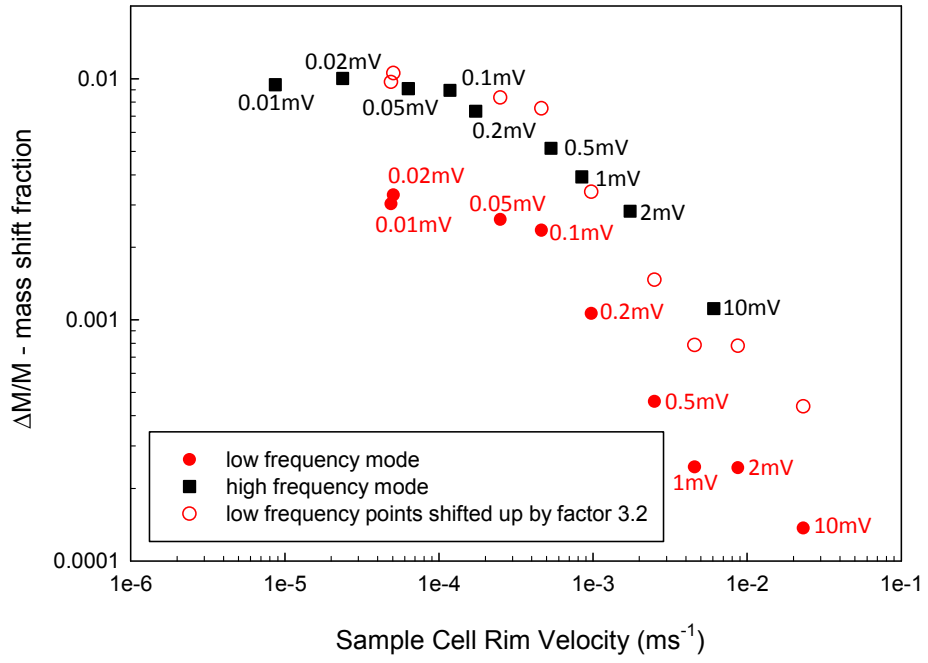

Figure 6.1: The measured period shift as a function of cell velocity.

The signal voltage from the torsional oscillator is proportional to its velocity, as shown by Eq. 2.31, but this describes the velocity of the vane – we are interested in the velocity of the sample.

From the ratio of displacements in Eq. 2.66 we know that the relative motion of

the head and the body is

$$\left.\frac{x_2}{x_1}\right| = \frac{k_2}{k_2 - M_2\omega^2} = \frac{1}{1 - \omega^2/\omega_2^2} \tag{6.1}$$

which we scale by the ratio of the radius of the rim of the specimen to that of the vane to find the velocity of the sample rim at a given frequency

$$v_{\text{rim}} = v_{\text{vane}} \frac{1}{1 - \omega^2/\omega_2^2} \times \frac{r_{\text{rim}}}{r_{\text{vane}}}. \tag{6.2}$$

From the signal voltage of the torsional oscillator readout we find the velocity of the rim of the sample and plot this against the measured period shift to produce the plot in Fig. 6.1. The two plots follow the same curve, shifted on the vertical axis due to the frequency dependence of the period shift. By multiplying the low mode points by 3.2 (hollow red circles) we see that the two modes have the same 'rolloff' as the full period shift is suppressed by increasing the velocity of the oscillator. The knee of this curve gives a critical velocity in the region of $100\,\mu\text{m}\,\text{s}^{-1}$. The 'pancake' geometry of our cell limits our ability to determine the critical velocity, as the velocity of the sample goes as its radius from the axis, smearing the knee of the curve.

6.2 The Effect of Changes in Shear Modulus

Apparent changes in moment of inertia at zero frequency may originate from changes in the moment of inertia M and from changes in the spring constant k. Changes in the spring constant of the silver torsion rod are accounted for in the subtraction of the empty-cell background, but as our cell is filled through a fill line drilled through the torsion rod we must consider the effect of the helium in the line on the period of the oscillator. The piezo cell measurements of Day and Beamish [25] have shown that the shear modulus of solid ^{4}He increases significantly in the vicinity of 200 mK, independently of frequency, with strikingly similar drive and ^{3}He concentration dependence. The effect of this increase in shear modulus of the helium in the fill line is to stiffen the torsion rod, and as we showed in Eq. 2.3

$$\omega_0 = \sqrt{\frac{k}{M}}$$

an increase in the natural frequency of the oscillator may arise from *either* a reduction in its moment of inertia M *or* an increase in its spring constant k. This stiffening of the helium has been shown to account for an appreciable fraction of the observed period shift of torsional oscillators using a hollow torsion rod, depending on their particular geometry [14]. This effect must be taken into account before any conclusions can be drawn from an apparent change in moment of inertia.

We denote the outer radius of the torsion rod as $r_{\rm o}$ and the radius of the fill line as $r_{\rm i}$, and the shear modulus of the rod material $\mu_{\rm r}$. If the shear modulus of the helium in the torsion rod changes by $\Delta\mu_{\rm He}$ then the fractional change in the torsion constant of the rod is given by

$$\frac{\Delta k}{k} = \frac{\Delta\mu_{\rm He}}{\mu_{\rm r}} \frac{1}{(r_{\rm o}/r_{\rm i})^4 - 1}. \tag{6.3}$$

In our double oscillator we must consider the effect on both rods, which will be different due to their different geometry. Using the dimensions of the rods in Fig. 2.7 we find that

$$\begin{aligned} \frac{\Delta k_1}{k_1} &= 2.02 \times 10^{-2} \frac{\Delta\mu_{\rm He}}{\mu_{\rm He}} \\ \frac{\Delta k_2}{k_2} &= 7.72 \times 10^{-4} \frac{\Delta\mu_{\rm He}}{\mu_{\rm He}}. \end{aligned} \tag{6.4}$$

Changes to the two modes will then be

$$\begin{aligned} \Delta P_{\rm a} &= \frac{\partial P_{\rm a}}{\partial k_1}\Delta k_1 + \frac{\partial P_{\rm a}}{\partial k_2}\Delta k_2 \\ \Delta P_{\rm s} &= \frac{\partial P_{\rm s}}{\partial k_1}\Delta k_1 + \frac{\partial P_{\rm s}}{\partial k_2}\Delta k_2 \end{aligned} \tag{6.5}$$

which in terms of the logarithmic derivatives discussed in section 2.6 becomes

$$\begin{aligned} -\frac{\Delta P_{\rm a}}{P_{\rm a}} &= (\frac{1}{2} - \alpha)\frac{\Delta k_1}{k_1} + \alpha\frac{\Delta k_2}{k_2} \\ -\frac{\Delta P_{\rm s}}{P_{\rm s}} &= \alpha\frac{\Delta k_1}{k_1} + (\frac{1}{2} - \alpha)\frac{\Delta k_2}{k_2}. \end{aligned} \tag{6.6}$$

This gives the contributions from shear modulus changes in the helium in the rods to the two modes as

$$\begin{aligned} -\frac{\Delta P_{\mathrm{a}}}{P_{\mathrm{a}}} &= 1.51 \times 10^{-3} \frac{\Delta \mu_{\mathrm{He}}}{\mu_{\mathrm{r}}} \\ -\frac{\Delta P_{\mathrm{s}}}{P_{\mathrm{a}}} &= 8.97 \times 10^{-3} \frac{\Delta \mu_{\mathrm{He}}}{\mu_{\mathrm{r}}}. \end{aligned} \tag{6.7}$$

We take the shear modulus of coin silver to be 33 GPa and the shear modulus of ^{4}He at the sample pressure of 42 bar to be 15 MPa [26][36]. A typical shear modulus shift in a polycrystaline helium of 25% as reported by Day and Beamish [26] would thus cause period shifts of $\Delta P_{\mathrm{s}} = 2.5$ ns and $\Delta P_{\mathrm{a}} = 0.08$ ns in the symmetric mode and antisymmetric mode respectively. Changes in the shear modulus of the polycrystaline sample may therefore account for less than one third of the observed period shift in the symmetric mode, and have a negligible effect on the antisymmetric mode.

6.3 Movement of the Sample Chamber Base

Maris has shown that the behaviour of the cell can be influenced by the movement of the base of the sample chamber [61]. He demonstrates that the base of the cell will be in torsion as well as the rod below it, and changes in the shear modulus of the helium in the cell can have a significant effect on the effective torsion constant of the base. This will in turn change frequency of the oscillator. Maris estimates

the fractional change in the torsion constant of the rod to be

$$\frac{\Delta k_2}{k_2} = \frac{r_o^3}{8lw^2}\frac{\Delta\mu_{\mathrm{He}}}{\mu_{\mathrm{m}}} \tag{6.8}$$

where l is the length of the torsion rod (in our case rod 2, as this is the one connected to the sample chamber), w is the thickness of the base and μ_{m} is the shear modulus of the sample cell material. For our oscillator then

$$\frac{\Delta k_2}{k_2} = 3.65 \times 10^{-2}\frac{\Delta\mu_{\mathrm{He}}}{\mu_{\mathrm{m}}}. \tag{6.9}$$

Comparing this to Eq. 6.4 we can see that this effective change in torsion constant of the upper rod is some 50 times that from the change in shear modulus of helium inside the rod.

From Eq. 6.6 we can again find the change in the oscillator period arising from this effect, assuming a 25% change in μ_{He}:

$$\begin{aligned} -\frac{\Delta P_{\mathrm{a}}}{P_{\mathrm{a}}} &= 1.61 \times 10^{-2}\frac{\Delta\mu_{\mathrm{He}}}{\mu_{\mathrm{r}}} \\ -\frac{\Delta P_{\mathrm{s}}}{P_{\mathrm{a}}} &= 2.12 \times 10^{-3}\frac{\Delta\mu_{\mathrm{He}}}{\mu_{\mathrm{r}}}. \end{aligned} \tag{6.10}$$

This leads to an increase in ΔP_{s} of 0.61 ns and an increase in ΔP_{a} of 0.93 ns. Thus we see that this effect may account for some 7% of the low frequency period shift, and around 43% of the high mode shift. We see that the effect of the stiffening

of the helium sample on the base of the sample cell makes little difference to the zero-frequency $\Delta M/M$, as this is chiefly influenced by the symmetric mode.

6.4 Frequency Dependence

The torsional oscillator suffers a serious complication in studying solid samples – the elastic motion of the sample. The sample is being accelerated by the walls of the sample chamber. The sample has inertia and therefore is subjected to an oscillating shear stress as the oscillator accelerates, and as it has a finite shear modulus it will distort. The oscillator will thus experience a back-action torque arising from the viscoelastic motion of the sample. The effect of this viscoelastic back-action is discussed by Yoo and Dorsey [94] who find that it can account for some, but not all, of the period shift observed in previous experiments. They show that the viscoelastic contribution to period shift will vary as the square of frequency.

The use of a two-mode torsional oscillator allows us to study the frequency dependence of the period shift. As we have only two frequencies available to us we are not in a position to fit a particular distribution but by plotting the period shift, scaled by the mass sensitivity to give $\frac{\Delta M}{M_{\mathrm{He}}}$, against the square of the oscillator frequency we are able to fit the viscoelastic contribution described by Yoo and Dorsey as a straight line. The intercept of this line will then give the frequency-independent apparent change in moment of inertia. This plot is shown in Fig. 6.2, with the shifts

and intercept. A true superfluid-like mass flow would be frequency independent, so it is this zero-frequency shift that is of interest. We find a residual 'missing moment of inertia' fraction at zero frequency of 1.3 ± 0.2.

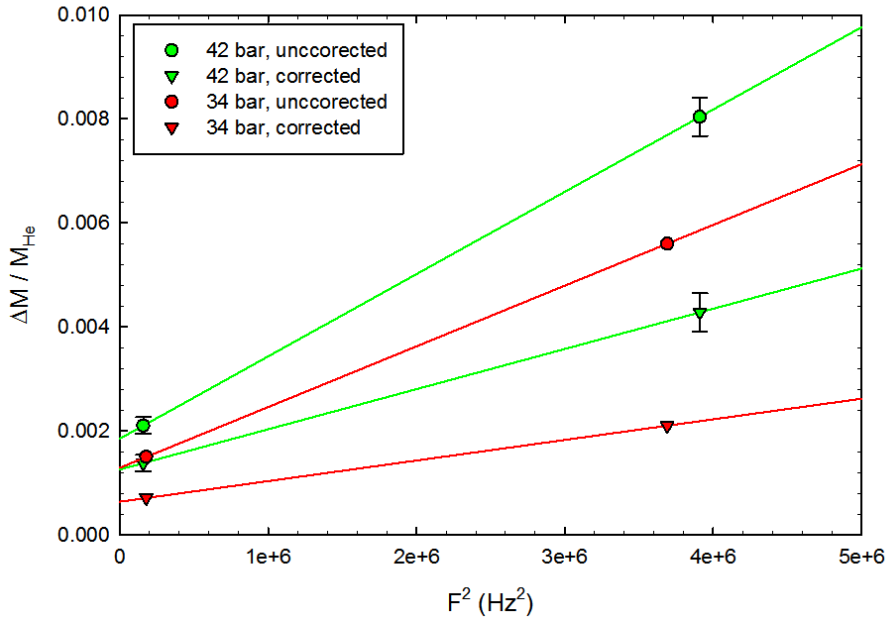

Figure 6.2: The frequency dependence of the period drop. Here $\frac{\Delta M}{M}$ is plotted against the square of frequency. The green points represent the most recent experimental run using a well characterised cell. Measurements from a previous experimental run using a different TO cell of the same design are given in red for reference. The α sensitivity factor for the previous cell is assumed to be the the same as the current cell. Error bars arise from the range of period shifts that may be inferred from the temperature sweeps at low drives. The projection back to zero frequency represents the period shift which does not arise from viscoelastics.

6.5 Comparison with Aoki, Graves and Kojima

The double-oscillator experiments of Aoki *et al* [9, 8, 39] provide a point of comparisson with our work. The sensitivity of their cell to changes in shear modulus is not discussed but from the details in [8] we are able to determine the α and β parameters of their cell.

Their sample chamber is a bored out epoxy cylinder of 10.2 mm inner diameter and 7.6 mm height, giving a volume of $6.2 \times 10^{-7}\,\mathrm{m}^3$. The sample discussed in [8] was loaded to a final pressure of 37 bar. At this pressure ^{4}He has a molar volume of $20.21\,\mathrm{cm}^3\,\mathrm{mol}^{-1}$ (extrapolated from [37]), giving a sample mass of $1.23 \times 10^{-4}\,\mathrm{kg}$ with moment of inertia $M_{^4\mathrm{He}} = 1.6 \times 10^{-9}\,\mathrm{kg\,m}^2$. The two resonant frequencies are given as $f_s = 496\,\mathrm{Hz}$ and $f_a = 1175\,\mathrm{Hz}$, which on loading the sample decrease by $\Delta f_s = 0.6\,\mathrm{Hz}$ and $\Delta f_a = 2.0\,\mathrm{Hz}$ respectively.

Following the analysis of our oscillator in section 2.5 we can ascertain the parameters for the cell of Aoki *et al* listed in Table 6.1 along with those of our oscillator for comparison.

As one would expect, $k_1 \approx k_2$ as the upper and lower rods are nominally identical. Their oscillator has very similar susceptibility to changes in shear modulus as ours (same α), but their mass sensitivity is greater (larger β). As discussed in section 2.6 the necessary trade-off for this is a narrower seperation in frequencies.

They observe the same 0.1% apparent mass decoupling ("NCRIF") for both the

Table 6.1: Comparison with the oscillator of Aoki *et al.*

	Aoki *et al*	This work
f_s	496 Hz	399 Hz
f_a	1175 Hz	1978 Hz
k_1	10.7	3.35
k_2	9.84	13.7
M_1	7.26×10^{-7} kg m^2	1.43×10^{-7} kg m^2
M_2	2.74×10^{-7} kg m^2	3.27×10^{-7} kg m^2
ω_1	$2\pi \times 611$ Hz	$2\pi \times 769.7$ Hz
ω_2	$2\pi \times 954$ Hz	$2\pi \times 1026$ Hz
α	0.444	0.442
β	0.294	0.119

low and high frequency modes. From their oscillator frequencies and mass loading frequency shifts we can ascertain that this corresponds to period shifts of $\Delta P_s = 4.93\,\mu$s and $\Delta P_a = 1.24\,\mu$s. Using the calculated value of α for their cell we may correct for shear modulus effects as above using the given geometry of their oscillator. We can attribute period drops of $\Delta P_s = 2.3$ ns and $\Delta P_a = 0.98$ ns to stiffening of the torsion rods. The base of the sample chamber contains an intermediate step in and is formed from mixed materials making analysis of its movement more complicated. From some of the general comments in [61] we can likely neglect movement of the sample base as it is relatively thick. Fig 6.3 shows the correction applied to the data of Aoki *et al* and extrapolated back to give a zero-frequency missing moment of inertia.

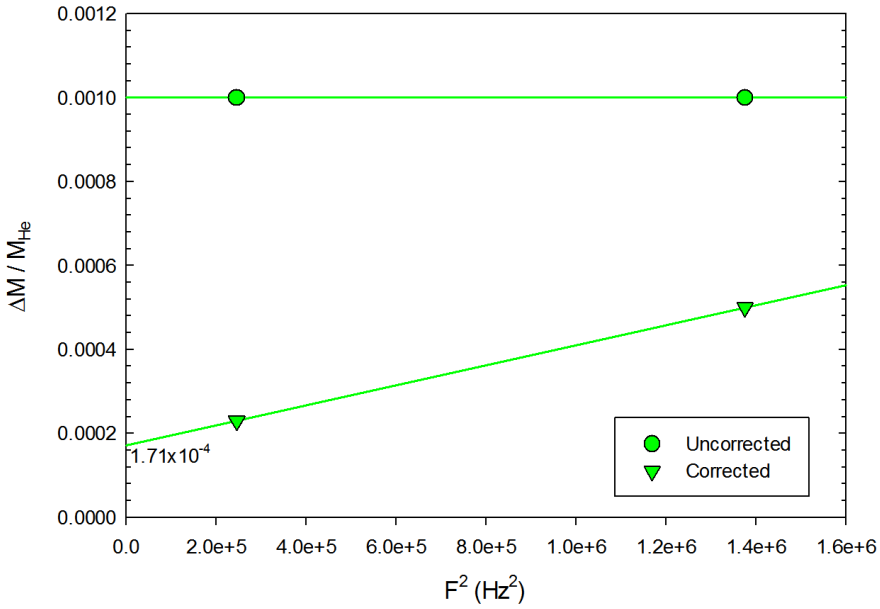

Figure 6.3: Data of Aoki *et al*, original (circles), and with shear modulus correction applied (triangles).

6.6 Conclusions

This work has developed the two-mode torsional oscillator for experiments on solid helium at millikelvin temperatures, improving its performance and analysing its sensitivity to mass and shear modulus changes. By using a two mode oscillator we are able to study the frequency dependence of a single sample, avoiding sample-to-sample variation, and correct for effects arising from changes in shear modulus. A coin silver torsional oscillator was used with two torsion rods, a 'dummy' mass with drive and pickup vanes and a sample chamber with an *in situ* pressure gauge. Several wiring arrangements were tested and the highest Q performance was achieved using a short length of 38-gauge copper wire from a PCB pad to the wings of

the oscillator, as close as possible to the torsion axis. A method for running the torsional oscillator without wires to the vanes was also developed and implemented. An adsorbtion bump was also fitted to the cryostat which may have significantly improved Q performance.

We have derived expressions for the sensitivity of the oscillator's frequency to changes in moment of inertia and spring constant arising from flow or changing shear modulus of the sample, reducible to two constants α and β, calculated from the changes in the frequencies on loading the sample cell.

We developed new software to capture the free decay of the oscillator and extract its resonant frequency and Q much faster than conventional frequency-domain sweeping. In the future this may be developed into a new measurement scheme to measure frequency shift and dissipation as 2D surfaces rather than as a collection of amplitude plots. We have also modelled the motion of the oscillator using commercial finite element analysis. We have measured the frequency and Q of the empty torsional oscillator cell as a function of temperature at a range of drive velocities and found that the cell response collapses on to a common curve when driven below $100\,\mu\mathrm{m\,s^{-1}}$. The cell was then filled with BCC ^{3}He and measured again. The empty cell backgrounds were subtracted away leaving the bare sample response which showed a slope but no clear features. The cell was then emptied and flushed with ^{4}He, loaded with a polycrystaline sample of ^{4}He and measured again. On sub-

tracting the empty cell background a shift down in the period and a dissipation peak were observed at both frequencies, suppressed at high drive velocities. This is consistent with the phenomenon some groups refer to as 'supersolidity'.

By considering the α sensitivity parameter and the frequency dependence of the effect we have accounted for possible non-superfluid contributions to the torsional oscillator period shift in ^{4}He. We conclude that there is a fraction of the observed period shift extrapolated to zero frequency which does not arise from changes in the shear modulus of the helium in the torsion rod or from the vicsoelastic behaviour of the sample. This corrected zero frequency period shift corresponds to an apparent decoupling of 0.135% of the sample, with a critical velocity $v_c \approx 100\,\mu\mathrm{m\,s^{-1}}$. This 'missing moment of inertia' remains unaccounted for by mechanisms of false period shift proposed in the literature and may be a sign of genuine superfluid-like behaviour. We have compared our data to that of Aoki *et al*, applying appropriate corrections for shear modulus effects and extrapolated back to zero frequency. We find that they also show a residual missing moment of inertia, but it is almost an order of magnitude smaller than that observed in our experiment.

Chapter 7

Further Work

> Poems are never finished – just abandoned.
>
> *Paul Valéry*

7.1 Extending ^{4}He Results

The behaviour of solid ^{4}He samples in torsional oscillator cells is well known to be highly dependent on sample preparation. Slight differences in the cooling rate, isotopic purity, sample cell design *etc.* can drastically change the observed period shifts, so repeating the measurements above with crystals grown under the same and various other conditions is of paramount importance.

Samples may be grown under constant pressure as well as under constant volume as used in this experiment. By adding a thermal link from the mixing chamber to the

cell and weakening the thermal anchors on the fill line the crystal may be nucleated inside the cell and grow outward, producing a single crystal in the cell. If the cryostat is cooled below 2 K and the pressure raised while the fill line is heated it is possible to grow a single crystal from superfluid helium. This crystal will be of exceptionally high quality which according to other groups greatly diminishes the period shift. However, Balibar *et al* have shown that the shear modulus behaviour of ^{4}He monocrystals depends strongly on their orientation. We do not have the capability to determine the orientation of the crystal in the sample chamber, so it is questionable how informative monocrystal results can be without direct observation of the crystal growth as afforded by the optical cryostat and sapphire cells of Balibar *et al*.

Sample quality may be affected after growth by pressure changes or thermal shock [81, 29] to introduce disorder, or by annealing to reduce it [72, 81, 26]. By warming the cell up to near the melting line grain boundaries and dislocations in the polycrystal will relax and a higher quality sample will result.

The viscoelastic contribution calculated by Yoo and Dorsey [94] assumes fixed boundary conditions–that there is no slip between the sample and the walls of the cell. This assumption could be tested by using sample cells with different surface preparations. The existing cell has a machined finish. Torsional oscillator sample chambers made in three sections could be polished to promote slippage, and another

bead blasted to reduce it. Because of the known variation between samples several crystals would need to be grown in each cell. A reproducible change in the frequency dependence of the samples would indicate that sample slippage is contributing to the behaviour of the oscillator.

The two-mode oscillator allows for further exploration of critical velocity effects. By mixing two AC drives the oscillator may be driven at both frequencies simultaneously with its response read out at the two drive frequencies by lock-in amplifiers. By driving one mode at low amplitude and raising the amplitude of the other one should observe the suppression of *both* modes as the sample exceeds its critical velocity. If the same suppression is observed for both modes while over-driving the other it is very likely that a superfluid-like critical velocity is responsible.

7.2 HCP ^{3}He

The 'supersolid' period shift has never been observed in ^{3}He samples. Beamish *et al* have observed a shear modulus change in HCP solid ^{3}He, but not in BCC. As ^{4}He is necessarily HCP in the temperature range where the 'supersolid' period shift is observed we are naturally curious what behaviour HCP ^{3}He might show in a torsional oscillator. If the 'supersolid' period shift is entirely the result of the shear modulus change then one would expect similar results in HCP ^{3}He as in ^{4}He.

Only one torsional oscillator experiment on HCP ^{3}He is documented in the lit-

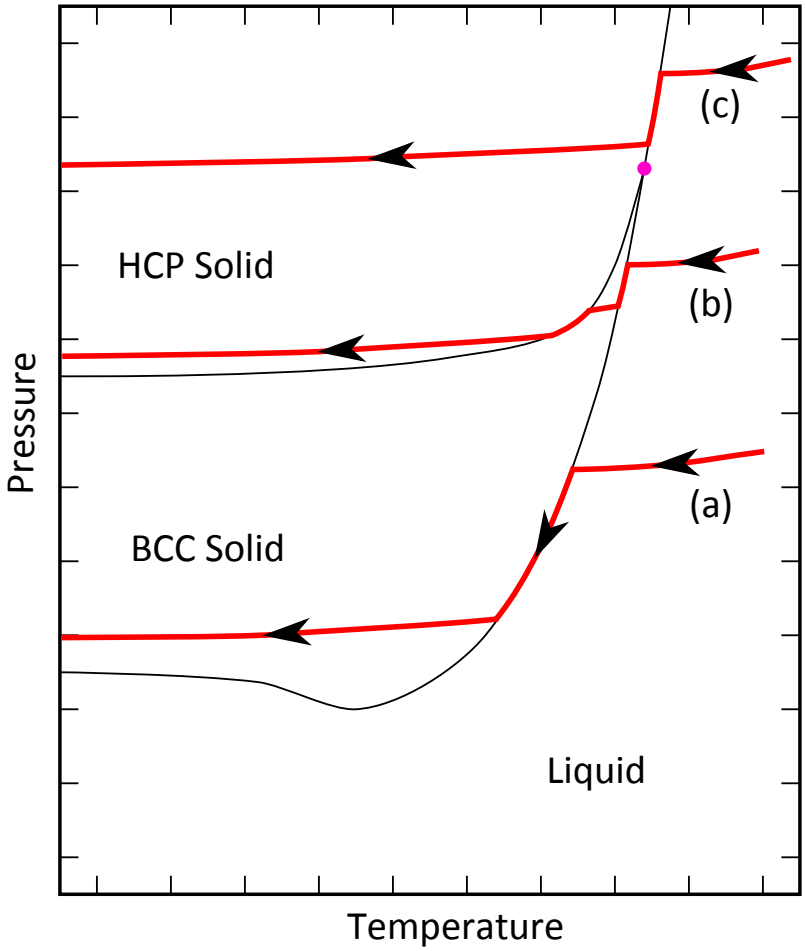

Figure 7.1: Phase diagram of ^{3}He showing possible blocked-capillary sample growth isochors, (a) BCC throughout, (b) HCP cooled through BCC, and (c) HCP throughout. The tri-critical point is shown in pink.

erature [90] and no period shift was observed. However in order to support the high pressure required to form HCP ^{3}He (at least 108 bar, see Fig. 5.7) the experimental cell used was of a very different design to earlier ^{4}He experiments. As the path length experiments by Chan *et al* [51], amongst others, have shown certain designs appear to yield no period shift in ^{4}He, and the experiment was never repeated in the same cell with ^{4}He [90].

Our experimental cell has shown the period shift effect in ^{4}He, and the design has been pressure tested up to 150 bar. Its *in situ* pressure gauge allows us to exactly position a sample on the phase diagram with no uncertainty regarding pressure changes from phase transitions and thermal contraction. As such we are ideally placed to test the torsional oscillator behaviour of HCP solid ^{3}He. A subsequent experiment must grow a solid ^{3}He sample in a clean cell at a final pressure of at least 110 bar and measure its response. This can be directly compared to a ^{4}He sample grown under the same conditions and the shear modulus shifts of ^{3}He and ^{4}He. This measurement has the potential to offer an amount of closure on the 'supersolid' question.

7.3 Nuclear Magnetic Resonance

The TO period shift and shear modulus change in solid ^{4}He are known to be strongly dependant on ^{3}He impurity concentration, x_3. Some explanations of the phenomena centre on the 'pinning' of dislocations by ^{3}He [26, 46] and so we are keen to know more about its microscopic action. As the magnetogyric ratio of ^{3}He is large and the surrounding ^{4}He has no nuclear magnetic moment to obscure its signal, one might imagine these samples are highly amenable to Nuclear Magnetic Resonance (NMR). Unfortunately, the required concentrations of less than 100ppm at which the phenomena are observable make such measurements exceptionally difficult. The

tiny number of ^{3}He nuclei in the experimental cell make for very weak signals. The physical separation of adjacent ^{3}He atoms means that their interactions will be faint, and consequently the spin-lattice relaxation time T_1 will be exceedingly long, while the exchange of ^{3}He and ^{4}He atoms in the solid at low temperatures will make the spin-spin relaxation time T_2 very short. These factors all conspire to make NMR investigation of 'supersolid' samples challenging.

Sullivan *et al* have been able to measure samples down to $x_3 = 16$ppm [54] and observe a number of features but are unable to resolve these clearly or extend to lower concentrations. The use of Superconducting QUantum Interference Devices (SQUIDs) may allow detections of even smaller concentrations. SQUIDs exploit a property of Josephson junctions to detect minute changes in magnetic felds. A DC SQUID is formed from a loop of superconductor, broken by two Josephson junctions in parallel. In the absence of magnetic flux an equal supercurrent I may flow through each junction. When magnetic flux ϕ is applied a screening current I_s is induced in the loop to expell the flux, so that one junction experiences a current $I + I_s$ and the other $I - I_s$. When the critical current of a junction is exceeded it becomes resistive and a voltage is observed across the SQUID. If this flux is ramped up to exceed half a flux quantum ($\frac{\phi_0}{2} = \frac{h}{4e}$ where h is the Plank constant and e is the elementary charge) it is energetically favourable to admit one quantum of flux in to the loop and in doing so reverse the direction of the screening current. As such, the

critical current of the loop alternates periodically with increasing flux. By adjusting the biasing current the working point of the SQUID is set at the steepest part of the $V - \phi$ sinusoid the SQUID becomes a flux-to-voltage converter with astonishing sensitivity. Full details of SQUIDs and their operation may be found in [24].

By connecting the receiver coil of an NMR cell to the input coil of a SQUID mounted to the 4 K stage of the cryostat it may be used to amplify the minute relaxation signals coming from the cell. In this way the sensitivity of the experiment and therefore the range of available concentrations may be significantly increased. This technique could offer great insight into the microscopic behaviour of solid helium.

Bibliography

[1] J F Allen and H Jones. "New Phenomena Connected with Heat Flow in Helium II". In: *Nature* (1938).

[2] J F Allen and A D Misener. "Flow Phenomena in Liquid Helium II". In: *Nature* (1938).

[3] A C Anderson et al. "Heat Capacity of Dilute Solutions of Liquid ^{3}He in ^{4}He at Low Temperatures". In: *Phys. Rev. Lett.* (1966).

[4] P. W. Anderson, W. F. Brinkman, and David A. Huse. "Thermodynamics of an Incommensurate Quantum Crystal". In: *Science* 310.5751 (2005), pp. 1164–1166.

[5] A F Andreev and I M Lifshitz. "Quantum theory of defects in crystals". In: *Sov. Phys. JETP* (1969).

[6] E Andronikashvili. "A Direct Observation of Two Kinds of Motion in Helium II". In: *Zh. Eskp. Teor. Fiz.* 16 (1946), p. 780.

[7] J Annett. *Superconductivity, Superfluids and Condensates*. Oxford University Press, 2004.

[8] Y Aoki, J C Graves, and H Kojima. "Measurements of Non-classical Rotational Inertia of Solid ^{4}He at Two Frequencies". In: *J Low Temp Phys* 150 (2008), p. 252.

[9] Y Aoki, J C Graves, and H Kojima. "Oscillation Frequency Dependence of Nonclassical Rotation Inertia of Solid ^{4}He". In: *Phys. Rev. Lett.* 99.015301 (2007).

[10] S Balibar. "The discovery of superfluidity". In: *arXiv:physics/0611119* (2006).

[11] S Balibar. "The enigma of supersolidity". In: *Nature* (2010).

[12] Sébastien Balibar and Frédéric Caupin. "Comment on "Observation of Unusual Mass Transport in Solid hcp ^{4}He"". In: *Phys. Rev. Lett.* 101 (18 2008), p. 189601. DOI: 10.1103/PhysRevLett.101.189601. URL: http://link.aps.org/doi/10.1103/PhysRevLett.101.189601.

[13] K Baumann et al. "Dicke quantum phase transition with a superfluid gas in an optical cavity". In: *Nature* (2010).

[14] J. R. Beamish et al. "Elastic effects in torsional oscillators containing solid helium". In: *Physical Review B* 85.18 (2012), pp. 1–5. ISSN: 1098-0121. DOI: 10.1103/PhysRevB.85.180501. URL: http://link.aps.org/doi/10.1103/PhysRevB.85.180501.

[15] J. E. Berthold et al. "Determination of the ^{3}He Superfluid-Density Tensor for the A and B Phases". In: *Phys. Rev. Lett.* 37 (17 1976), pp. 1138–1141. DOI: 10.1103/PhysRevLett.37.1138. URL: http://link.aps.org/doi/10.1103/PhysRevLett.37.1138.

[16] D. J. Bishop, M. A. Paalanen, and J. D. Reppy. "Search for superfluidity in hcp ^{4}He". In: *Phys. Rev. B* 24 (5 1981), pp. 2844–2845. DOI: 10.1103/PhysRevB.24.2844. URL: http://link.aps.org/doi/10.1103/PhysRevB.24.2844.

[17] M L Boas. *Mathematical Methods in the Physical Sciences*. Wiley, 2006.

[18] Bonfait, G., Godfrin, H., and Castaing, B. "Solid ^{4}He : search for superfluidity". In: *J. Phys. France* 50.15 (1989), pp. 1997–2002. DOI: 10.1051/jphys:0198900500150199700. URL: http://dx.doi.org/10.1051/jphys:0198900500150199700.

[19] D.I. Bradley et al. "A dilution refrigerator combining low base temperature, high cooling power and low heat leak for use with nuclear cooling". In: *Cryogenics* 22.6 (1982), pp. 296 –304. ISSN: 0011-2275. DOI: http://dx.doi.org/10.1016/0011-2275(82)90060-1. URL: http://www.sciencedirect.com/science/article/pii/0011227582900601.

[20] M J Buckingham and W M Fairbank. *Progress in Low Temperature Physics*. Ed. by C J Gorter. 1961.

[21] R Bullock. *Least Squares Circle Fit*. 2006. URL: http://www.dtcenter.org/met/users/docs/write_ups/circle_fit.pdf.

[22] G V Chester. "Speculations on Bose-Einstein condensation and quantum crystals". In: *Phys. Rev. A* (1970).

[23] H. Choi et al. "Evidence of Supersolidity in Rotating Solid Helium". In: *Science* 330.6010 (2010), pp. 1512–1515. DOI: 10.1126/science.1196409. eprint: http://www.sciencemag.org/content/330/6010/1512.full.pdf. URL: http://www.sciencemag.org/content/330/6010/1512.abstract.

[24] J Clarke and A Braginkski. *The SQUID Handbook*. Wiley-VCH.

[25] James Day and John Beamish. "Low-Temperature shear modulus changes in solid ^{4}He and connection to supersolidity". In: *Nature* 450 (2007), p. 853.

[26] James Day and John Beamish. "Low-temperature shear modulus changes in solid ^{4}He and connection to supersolidity." In: *Nature* 450.7171 (2007), pp. 853–6. ISSN: 1476-4687. DOI: 10.1038/nature06383. URL: http://www.ncbi.nlm.nih.gov/pubmed/18064007.

[27] James Day and John Beamish. "Pressure-Driven Flow of Solid Helium". In: *Phys. Rev. Lett.* 96 (10 2006), p. 105304. DOI: 10.1103/PhysRevLett.96.105304. URL: http://link.aps.org/doi/10.1103/PhysRevLett.96.105304.

[28] J Emsley. *Nature's Building Blocks*. Oxford University Press, 2001.

[29] A Eyal et al. "Evidence for a High-Temperature Disorder-Induced Mobility in Solid ^{4}He". In: *Phys. Rev. Lett.* 105 (2 2010), p. 025301. DOI: 10.1103/PhysRevLett.105.025301. URL: http://link.aps.org/doi/10.1103/PhysRevLett.105.025301.

[30] A D Fefferman et al. "He Crystal Quality and Rotational Response in a Transparent Torsional Oscillator". In: (), pp. 1–15. arXiv: arXiv:1112.5998v2.

[31] R. P. Feynman. "Atomic Theory of the Two-Fluid Model of Liquid Helium". In: *Phys. Rev.* 94 (2 1954), pp. 262–277. DOI: 10.1103/PhysRev.94.262. URL: http://link.aps.org/doi/10.1103/PhysRev.94.262.

[32] R. P. Feynman and Michael Cohen. "Energy Spectrum of the Excitations in Liquid Helium". In: *Phys. Rev.* 102 (5 1956), pp. 1189–1204. DOI: 10.1103/PhysRev.102.1189. URL: http://link.aps.org/doi/10.1103/PhysRev.102.1189.

[33] D. E. Galli and L. Reatto. "Bose-Einstein Condensation of Incommensurate Solid ^{4}He". In: *Phys. Rev. Lett.* 96 (16 2006), p. 165301. DOI: 10.1103/PhysRevLett.96.165301. URL: http://link.aps.org/doi/10.1103/PhysRevLett.96.165301.

[34] D Greywall. "^{3}He specific heat and thermometry at millikelvin temperatures". In: *Phys. Rev. B* (1986).

[35] D Greywall. "Specific heat of normal liquid ^{3}He". In: *Phys. Rev. B* (1983).

[36] D. S. Greywall. "Search for superfluidity in solid ^{4}He". In: *Phys. Rev. B* 16 (3 1977), pp. 1291–1292. DOI: 10.1103/PhysRevB.16.1291. URL: http://link.aps.org/doi/10.1103/PhysRevB.16.1291.

[37] E R Grilly. "Pressure-Volume-Temperature Relations in Liquid and Solid ^{4}He". In: *J. Low. Temp. Phys* (1973).

[38] E R Grilly and R L Mills. "Melting Properties of ^{3}He and ^{4}He up to 3500 kg/cm^2". In: *Annals of Physics* (1959).

[39] P Gumann et al. "Effects of ^{3}He Impurity on the Non-classical Rotational Inertia of Solid ^{4}He Studied by Double Resonance Torsional Oscillator". In: *J Low Temp Phys* 158 (2010), pp. 567–571.

[40] R B Hallock. "Superfluid Helium". In: *American Journal of Physics* (1982).

[41] Ariel Haziot et al. "Giant Plasticity of a Quantum Crystal". In: *Phys. Rev. Lett.* 110 (3 2013), p. 035301. DOI: 10.1103/PhysRevLett.110.035301. URL: http://link.aps.org/doi/10.1103/PhysRevLett.110.035301.

[42] D. G. Henshaw and A. D. B. Woods. "Modes of Atomic Motions in Liquid Helium by Inelastic Scattering of Neutrons". In: *Phys. Rev.* 121 (5 1961), pp. 1266–1274. DOI: 10.1103/PhysRev.121.1266. URL: http://link.aps.org/doi/10.1103/PhysRev.121.1266.

[43] Pei-Chun Ho, IanP. Bindloss, and JohnM. Goodkind. "A New Anomaly in Solid ^{4}He". English. In: *Journal of Low Temperature Physics* 109.3-4 (1997),

pp. 409–421. ISSN: 0022-2291. DOI: 10.1007/s10909-005-0094-0. URL: http://dx.doi.org/10.1007/s10909-005-0094-0.

[44] P Horowitz and W Hill. *The Art of Electronics*. Cambridge University Press, 2001.

[45] B. Hunt et al. "Evidence for a Superglass State in Solid ^{4}He". In: *Science* 324.5927 (2009), pp. 632–636. DOI: 10.1126/science.1169512. eprint: http://www.sciencemag.org/content/324/5927/632.full.pdf. URL: http://www.sciencemag.org/content/324/5927/632.abstract.

[46] Evan S H Kang, Hongkee Yoon, and Eunseong Kim. "Microscopic description of stress- and temperature-dependent shear modulus in solid ^{4}He". In: *arXiv:1211.5593v1* (2012), pp. 1–12. arXiv: arXiv:1211.5593v1.

[47] P Kapitza. "Viscosity of Liquid Helium below the λ-Point". In: *Nature* (1938).

[48] W H Keesom. "Comm. Kamerlingh Onnes Lab., Leiden". In: *Helium*.

[49] Tassilo Keilmann, Ignacio Cirac, and Tommaso Roscilde. "Dynamical Creation of a Supersolid in Asymmetric Mixtures of Bosons". In: *Phys. Rev. Lett.* 102 (25 2009), p. 255304. DOI: 10.1103/PhysRevLett.102.255304. URL: http://link.aps.org/doi/10.1103/PhysRevLett.102.255304.

[50] Duk Y. Kim and Moses H. W. Chan. "Absence of Supersolidity in Solid Helium in Porous Vycor Glass". In: *Phys. Rev. Lett.* 109 (15 2012), p. 155301. DOI:

10.1103/PhysRevLett.109.155301. URL: http://link.aps.org/doi/10.1103/PhysRevLett.109.155301.

[51] Duk Y. Kim et al. "Probing phase coherence in solid helium using torsional oscillators of different path lengths". In: *Phys. Rev. B* 85 (2 2012), p. 024533. DOI: 10.1103/PhysRevB.85.024533. URL: http://link.aps.org/doi/10.1103/PhysRevB.85.024533.

[52] E Kim and M H W Chan. "Observation of Superflow in Solid Helium". In: *Science* 305 (2004), p. 1941.

[53] E. Kim and M. H. W. Chan. "Probable observation of a supersolid helium phase". In: *Nature* 427.6971 (2004), pp. 225–227.

[54] S S Kim et al. "NMR study of the dynamics of ^{3}He impurities in the proposed supersolid state of solid ^{4}He". In: ().

[55] R. K. Kochhar. "French astronomers in India during the 17th - 19th centuries". In: *Journal of the British Astronomical Association* 101 (1991), pp. 95–100.

[56] A J Leggett. "Can a Solid be "Superfluid"?" In: *Phys Rev Lett* 25 (1970), pp. 1543–1546.

[57] Alfred Leitner. *"Liquid Helium, Superfluid.* Educational video. 1963.

[58] F London. "The λ-Phenomenon of Liquid Helium and the Bose-Einstein Degeneracy". In: *Nature* (1938).

[59] O V Lounasmaa. *Experimental Principles and Methods below 1K*. Academic Press, 1974.

[60] *Low Temperature Techniques*. Materials Science Center, Cornell University, 1981.

[61] Humphrey J. Maris and Sebastien Balibar. "Effect of Helium Elasticity on Torsional Oscillator Measurements". In: *Journal of Low Temperature Physics* 162.1-2 (2010), pp. 12–22. ISSN: 0022-2291. DOI: 10.1007/s10909-010-0268-2. URL: http://www.springerlink.com/index/10.1007/s10909-010-0268-2.

[62] P V E McClintock, D J Meredith, and J K Wigmore. *Matter at Low Temperatures*. Blackie, 1984.

[63] Mark Meisel. "Supersolid ^{4}He: an overview of past searches and future possibilites". In: *Physica B* 178 (1992), p. 121.

[64] Xiao Mi, Erich J Mueller, and John D Reppy. "Study of Supersolidity and Shear Modulus Anomaly of ^{4}He in a Triple Compound Oscillator". In: *Journal of Physics: Conference Series* 400.1 (2012), p. 012047. ISSN: 1742-6588. DOI: 10.1088/1742-6596/400/1/012047. URL: http://stacks.iop.org/1742-6596/400/i=1/a=012047?key=crossref.3e05d38d82104e771bc6d3222d025142.

[65] Xiao Mi and John D. Reppy. "Anomalous Behavior of Solid ^{4}He in Porous Vycor Glass". In: *Phys. Rev. Lett.* 108 (22 2012), p. 225305. DOI: 10.1103/

PhysRevLett.108.225305. URL: http://link.aps.org/doi/10.1103/PhysRevLett.108.225305.

[66] G W Morley et al. "Torsion Pendulum for the Study of Thin ^{3}He Films". In: *JLTP* (2002).

[67] *Nobel Lectures, Physics 1901-1970*. Elsevier, 1967.

[68] NSRW. *MATERIAL SAFETY DATA SHEET - Copper Beryllium Wrought Alloy*. 2003.

[69] D. D. Osheroff, R. C. Richardson, and D. M. Lee. "Evidence for a New Phase of Solid ^{3}He". In: *Phys. Rev. Lett.* 28 (14 1972), pp. 885–888. DOI: 10.1103/PhysRevLett.28.885. URL: http://link.aps.org/doi/10.1103/PhysRevLett.28.885.

[70] D. D. Osheroff et al. "New Magnetic Phenomena in Liquid ^{3}He below 3 mK". In: *Phys. Rev. Lett.* 29 (14 1972), pp. 920–923. DOI: 10.1103/PhysRevLett.29.920. URL: http://link.aps.org/doi/10.1103/PhysRevLett.29.920.

[71] Oliver Penrose and Lars Onsager. "Bose-Einstein Condensation and Liquid Helium". In: *Phys. Rev.* 104.3 (1956), pp. 576–584.

[72] Andrey Penzev, Yoshinori Yasuta, and Minoru Kubota. "Annealing Effect for Supersolid Fraction in ^{4}He". In: *J Low Temp Phys* 148 (2007), p. 677.

[73] W A Phillips. *Amorphous Solids: Low Temperature Properties*. 1981.

[74] F Pobell. *Matter and Methods at Low Temperatures*. Springer, 2007.

[75] M. W. Ray and R. B. Hallock. "Mass Flux and Solid Growth in Solid ^{4}He for 60˘700 mK". In: *Phys. Rev. Lett.* 105 (14 2010), p. 145301. DOI: 10.1103/PhysRevLett.105.145301. URL: http://link.aps.org/doi/10.1103/PhysRevLett.105.145301.

[76] M. W. Ray and R. B. Hallock. "Observation of Unusual Mass Transport in Solid hcp ^{4}He". In: *Phys. Rev. Lett.* 100 (23 2008), p. 235301. DOI: 10.1103/PhysRevLett.100.235301. URL: http://link.aps.org/doi/10.1103/PhysRevLett.100.235301.

[77] M. W. Ray and R. B. Hallock. "Ray and Hallock Reply:" in: *Phys. Rev. Lett.* 101 (18 2008), p. 189602. DOI: 10.1103/PhysRevLett.101.189602. URL: http://link.aps.org/doi/10.1103/PhysRevLett.101.189602.

[78] E S Reich. "Proponent of supersolid helium joins sceptics". In: *Nature* (2012).

[79] JD Reppy et al. "Interpreting Torsional Oscillator Measurements: Effect of Shear Modulus and Supersolidity". In: *Arxiv preprint arXiv:1112.2218* (2011). URL: http://arxiv.org/abs/1112.2218.

[80] R C Richardson and E N Smith. *Experimental Techniques In Condensed Matter Physics At Low Temperatures*. Westview Press, 1998.

[81] Ann Sophie C. Rittner and John D. Reppy. "Disorder and the Supersolid State of Solid ^{4}He". In: *Phys. Rev. Lett.* 98 (17 2007), p. 175302. DOI: 10.

1103/PhysRevLett.98.175302. URL: http://link.aps.org/doi/10.1103/PhysRevLett.98.175302.

[82] Ann Sophie C Rittner and John D Reppy. "Observation of Classical Rotational Inertia and Nonclassical Supersolid Signals in Solid ^{4}He below 250 mK". In: *Phys. Rev. Lett.* 97 (2006), p. 165301.

[83] Ann Sophie C. Rittner et al. "Absence of pressure-driven supersolid flow at low frequency". In: *Physical Review B* 80.22 (2009), p. 224516. ISSN: 1098-0121. DOI: 10.1103/PhysRevB.80.224516. URL: http://link.aps.org/doi/10.1103/PhysRevB.80.224516.

[84] G C Straty and E D Adams. "PVT Measurements of the hcp-bcc Phase Transition in Solid ^{3}He". In: *Physical Review* (1966).

[85] Stanford Research Systems. *About Lock-In Amplifiers*. URL: http://www.thinksrs.com/downloads/PDFs/ApplicationNotes/AboutLIAs.pdf.

[86] L Tisza. "Transport Phenomena in Helium II". In: *Nature* (1938).

[87] Laszlo Tisza. "The Theory of Liquid Helium". In: *Phys. Rev.* 72 (9 1947), pp. 838–854. DOI: 10.1103/PhysRev.72.838. URL: http://link.aps.org/doi/10.1103/PhysRev.72.838.

[88] I.A. Todoshchenko et al. "Absence of low-temperature anomaly on the melting curve of ^{4}He". English. In: *JETP Letters* 85.9 (2007), pp. 454–457. ISSN: 0021-

3640. DOI: 10.1134/S0021364007090093. URL: http://dx.doi.org/10.1134/S0021364007090093.

[89] G Weiss et al. "Acoustic properties of crystals at very low temperatures- Comparison with glasses". In: *Physica B* (1996).

[90] Joshua T. West et al. "Role of shear modulus and statistics in the supersolidity of helium". In: *Nature Physics* 5.8 (2009), pp. 598–601. ISSN: 1745-2473. DOI: 10.1038/nphys1337. URL: http://www.nature.com/doifinder/10.1038/nphys1337.

[91] J C Wheatley. "Dilute Solutions of ^{3}He in ^{4}He at Low Temperatures". In: *Am J Phys* (1968).

[92] J Wilks. *The Properties of Liquid and Solid Helium*. Oxford University Press, 1967.

[93] L J Wittenberg, J F Santarius, and G L Kulcinski. "Lunar Source of ^{3}He for Commercial Fusion Power". In: *Fusion Technology* (1986).

[94] C.-D. Yoo and Alan Dorsey. "Theory of viscoelastic behavior of solid ^{4}He". In: *Physical Review B* 79.10 (2009), p. 100504. ISSN: 1098-0121. DOI: 10.1103/PhysRevB.79.100504. URL: http://link.aps.org/doi/10.1103/PhysRevB.79.100504.

[95] G.N. Zastenker et al. "Isotopic Composition and Abundance of Interstellar Neutral Helium Based on Direct Measurements". English. In: *Astrophysics*

45.2 (2002), pp. 131–142. ISSN: 0571-7256. DOI: 10.1023/A:1016057812964. URL: http://dx.doi.org/10.1023/A%3A1016057812964.

[96] D. E. Zmeev and A. I. Golov. "Simultaneous Measurements of the Torsional Oscillator Anomaly and Thermal Conductivity in Solid ^{4}He". In: *Phys. Rev. Lett.* 107 (6 2011), p. 065302. DOI: 10.1103/PhysRevLett.107.065302. URL: http://link.aps.org/doi/10.1103/PhysRevLett.107.065302.